AGU ADVANCING EARTH AND SPACE SCIENCE

Reviews of Geophysics

REVIEW ARTICLE
10.1029/2019RG000690

Key Points:
- Iron-bearing minerals and ferrimagnetic minerals in particular are sensitive to faulting-associated physical and chemical processes
- Laboratory faulting experiments and comparison with nonmagnetic approaches confirm results from magnetic studies on natural rocks
- Rock magnetic methods offer novel tools to analyze strain, grain fining, temperature trends, and fluid-rock interaction in fault zones

Correspondence to:
T. Yang and M. J. Dekkers,
tyang@cugb.edu.cn;
t.yang@uu.nl;
m.j.dekkers@uu.nl

Citation:
Yang, T., Chou, Y.-M., Ferré, E. C., Dekkers, M. J., Chen, J., Yeh, E.-C., & Tanikawa, W. (2020). Faulting processes unveiled by magnetic properties of fault rocks. *Reviews of Geophysics*, *58*, e2019RG000690. https://doi.org/10.1029/2019RG000690

Received 28 FEB 2020
Accepted 21 SEP 2020
Accepted article online 3 OCT 2020

Faulting Processes Unveiled by Magnetic Properties of Fault Rocks

Tao Yang[1,2,3], Yu-Min Chou[4,5], Eric C. Ferré[6], Mark J. Dekkers[2], Jianye Chen[7,8], En-Chao Yeh[9], and Wataru Tanikawa[10]

[1]Hubei Subsurface Multi-Scale Imaging Key Laboratory, Institute of Geophysics and Geomatics, China University of Geosciences, Wuhan, China, [2]Paleomagnetic Laboratory Fort Hoofddijk, Department of Earth Sciences, Utrecht University, Utrecht, The Netherlands, [3]Now at School of Geophysics and Information Technology, China University of Geosciences, Beijing, China, [4]Shenzhen Key Laboratory of Marine Archaea Geo-Omics, Department of Ocean Science and Engineering, South University of Science and Technology, Shenzhen, China, [5]Southern Marine Science and Engineering Guangdong Laboratory, Department of Ocean Science and Engineering, Southern University of Science and Technology, Shenzhen, China, [6]School of Geosciences, University of Louisiana at Lafayette, Lafayette, LA, USA, [7]State Key Laboratory of Earthquake Dynamics, Institute of Geology, China Earthquake Administration, Beijing, China, [8]HPT Laboratory, Department of Earth Sciences, Utrecht University, Utrecht, Netherlands, [9]Department of Earth Sciences, National Taiwan Normal University, Taipei, Taiwan, [10]Japan Agency for Marine-Earth Science and Technology, Kochi Institute for Core Sample Research, Nankoku, Japan

Abstract As iron-bearing minerals—ferrimagnetic minerals in particular—are sensitive to stress, temperature, and presence of fluids in fault zones, their magnetic properties provide valuable insights into physical and chemical processes affecting fault rocks. Here, we review the advances made in magnetic studies of fault rocks in the past three decades. We provide a synthesis of the mechanisms that account for the magnetic changes in fault rocks and insights gained from magnetic research. We also integrate nonmagnetic approaches in the evaluation of the magnetic properties of fault rocks. Magnetic analysis unveils microscopic processes operating in the fault zones such as frictional heating, energy dissipation, and fluid percolation that are otherwise difficult to constrain. This makes magnetic properties suited as a "strain indicator," a "geothermometer," and a "fluid tracer" in fault zones. However, a full understanding of faulting-induced magnetic changes has not been accomplished yet. Future research should focus on detailed magnetic property analysis of fault zones including magnetic microscanning and magnetic fabric analysis. To calibrate the observations on natural fault zones, laboratory experiments should be carried out that enable to extract the exact physicochemical conditions that led to a certain magnetic signature. Potential avenues could include (1) magnetic investigations on natural and synthetic fault rocks after friction experiments, (2) laboratory simulation of fault fluid percolation, (3) paleomagnetic analysis of postkinematic remanence components associated with faulting processes, and (4) synergy of interdisciplinary approaches in mineral-magnetic studies. This would help to place our understanding of the microphysics of faulting on a much stronger footing.

Plain Language Summary The Earth's surface is riddled with faults that largely contribute to landscape evolution and human activities. Some of these faults produce earthquakes of different magnitudes including some with catastrophic consequences. Understanding faulting mechanisms benefits society when predictions about rupture are made. Fault zones preserve an excellent record of chemical and physical processes involved in failure. Among other analytical methods, magnetic studies prove to be an emergent and untapped source of information on these processes. These methods, focused on prefaulting, synfaulting, and postfaulting mineral changes, have resulted in significant advances in our understanding of the conditions of faulting. In this review, we present an extensive account of the state of knowledge and highlight current challenges and future avenues of fault magnetism research.

1. Introduction

Fault zones comprise only a very small volume of the Earth's crust. However, their structure and associated deformation processes are ultimately decisive for a wide range of crustal processes (e.g., Faulkner et al., 2010; Townend & Zoback, 2000). This pertains in particular to the physical origin of earthquakes

within the seismogenic zone, which typically extends from 3–4 to 15–20 km depth for faults in the continental crust (e.g., Scholz, 2019; Sibson, 1986). "Fault-related rocks" (Wise et al., 1984), or simply "fault rocks" (Sibson, 1977), form as a result of localized strain within a fault zone (Brodie et al., 2007). These rocks are common along upper crustal fault zones (Woodcock & Mort, 2008). Physical and chemical attributes, and textures of fault rocks hold valuable information for understanding both the long-term behavior of faults, on a timescale of millions of years, as well as the short-term behavior involving the nucleation (see Appendix A for definition), rupture, cessation, and recurrence of (large) earthquakes (Bradbury et al., 2015; Faulkner et al., 2010; Henderson et al., 2010; Rowe & Griffith, 2015; Schmid & Handy, 1991; Ujiie & Kimura, 2014; Wibberley et al., 2008). Studies into fault rocks thus have intrigued geologists for decades and have been and continue to be an important subject in the context of large, active faults with repeated seismic activity (Chester et al., 1993; Rowe & Griffith, 2015; Sibson, 1986).

It is realized that a full appreciation of earthquake dynamics requires an integration of macroscopic seismology with microscopic and experimental studies of fault zones (e.g., Cowan, 1999; Kanamori & Heaton, 2000; K.-F. Ma, 2009; Niemeijer et al., 2012; Scholz, 2019; Sibson, 1989). The former relies on earthquake kinematic analysis based on seismic waveform data (Kanamori & Heaton, 2000). The latter two mainly focus on the physical/chemical attributes and texture of fault rocks, including their formation mechanisms (K.-F. Ma, 2009; Scholz, 2019). Their combination is crucial for understanding earthquake energy dissipation, rupture processes, and seismic efficiency. Substantial research effort has been dedicated during the last two decades to understanding the development and physical/chemical attributes of fault rocks using diverse approaches—either of mesoscopic or microscopic scale—in natural faults, laboratory experiments, and numerical simulations (e.g., Billi, 2005; Mair & Abe, 2008; Rowe, Fagereng, et al., 2012; Rowe, Kirkpatrick, & Brodsky, 2012). These studies have covered aspects of fault rocks in the widest possible sense, including terminology and classification (Choi et al., 2016; Woodcock & Mort, 2008), development and architecture (Faulkner et al., 2010; Fossen & Rotevatn, 2016; Pei et al., 2015; Wibberley et al., 2008), microstructure (e.g., Boullier et al., 2009; Bradbury et al., 2015; Fossen & Cavalcante, 2017; Isaacs et al., 2007; Rowe & Griffith, 2015), grain-size distribution (e.g., Billi, 2005; Hattori & Yamamoto, 1999; Wilson et al., 2005), mineral assemblages (e.g., Boullier, 2011; Bradbury et al., 2015; J. Chen et al., 2013; Isaacs et al., 2007; Matsuda et al., 2004), geochemical composition (e.g., Bradbury et al., 2015; J. Chen et al., 2013; Isaacs et al., 2007; Tanaka et al., 2001), hydraulic properties (e.g., Bense et al., 2013; Carpenter et al., 2014; J. Chen et al., 2016; Faulkner et al., 2010), nanocrystallization (e.g., Verberne et al., 2019; Viti, 2011), geochronology (e.g., Oriolo et al., 2018), and frictional properties (e.g., Boulton et al., 2017; Carpenter et al., 2015; Di Toro et al., 2011; Niemeijer & Vissers, 2014).

A magnetic property analysis is occasionally included in the description of fault rock properties. Magnetic properties are primarily governed by the distribution and speciation of iron—the fourth most abundant element in the Earth's crust. By far most Fe-bearing minerals are not considered "magnetic" at room temperature; common minerals include Fe-bearing silicates, carbonates (siderite and ankerite), and sulfides (pyrite). What we refer to as magnetic minerals are ferromagnetic (sensu lato) minerals, which retain permanent or remanent magnetism; they include iron oxides (i.e., (titano)magnetite, maghemite, and hematite), oxyhydroxides (primarily goethite), and some iron sulfides (i.e., pyrrhotite and greigite). They occur only in trace amounts in the rock but nonetheless determine its magnetic signature. Metallic iron and other reduced phases such as iron phosphide, iron carbide, and iron silicide are also magnetic; they are extremely rare in the Earth's crust. All aforementioned minerals, magnetic and nonmagnetic, are not exempt from (thermo)chemical alterations induced by the faulting and related fluid-rock interaction, resulting in changes in magnetic properties of fault rocks in comparison to adjacent host rocks. Thus, magnetic properties of fault zones are natural archives of the faulting-associated processes in tectonically active regions. It makes rock magnetism, which is the study of the magnetic properties of rocks, sediments, soils, and even organisms, a promising tool to unravel faulting processes. Rock magnetic techniques are capable of determining the nature, grain size, and concentration of magnetic minerals in a sample down to the ppm level, which lies well below the detection limit of more conventional mineralogical techniques, for example, X-ray diffraction. Also, magnetic measurements are generally rapid, cost-effective, and nondestructive (evidently with the exception of high-temperature magnetic analysis) so they can be used in conjunction with other techniques. These advantages make rock magnetic analysis of fault rocks attractive.

Fault rocks, however, have been the subject of rock magnetic studies only recently, with a focus on faults from seismically active zones (e.g., Almqvist et al., 2020; Cai et al., 2019; Chou, Song, Aubourg, Lee, et al., 2012; Chou, Song, Aubourg, et al., 2014; Chou, Song, Aubourg, Song, et al., 2012; Chou, Song, Lee, et al., 2014; Ferré et al., 2005, 2012, 2015, 2016, 2017; Ferré, Gébelin, et al., 2014; Ferré, Geissman, et al., 2014; Fukuchi, 2003; Fukuchi et al., 2005, 2007, 2009; D. Liu et al., 2014, 2016; Mishima et al., 2006, 2009; Nakamura et al., 2002; Pei, Li, et al., 2014; Pei, Zhou, et al., 2014; Tanikawa et al., 2007, 2008; Yang et al., 2012a, 2012b, 2018, 2019; Yang, Chen, et al., 2013; Yang, Mishima, et al., 2013; Yang, Dekkers, & Zhang, 2016; Yang, Yang, et al., 2016; Zhang et al., 2017, 2018). By providing a trove of information on physical and chemical processes associated with faulting in seismically active zones, these pioneer works have laid the foundation of "fault magnetism", an emerging subdiscipline in the geosciences.

This review concentrates on the rock magnetic studies on fault rocks from seismically active fault zones where recent megaearthquakes occurred, such as the 1995 *Mw* (moment magnitude) 6.9 Kobe (Japan), the 1999 *Mw* 7.6 Chi-Chi (Taiwan), the 2008 *Mw* 7.9 Wenchuan (China), and the 2011 *Mw* 9.0 Tohoku (Japan) earthquakes. Additionally, magnetic studies on pseudotachylytes that are the products of fossil seismogenic fault zones are included. First, we describe concisely the processes that result in the formation of fault rocks. Second, we outline the approaches to evaluate magnetism of fault rocks. Third, we discuss the mechanisms that are responsible for changes in the magnetism of fault rocks. Fourth, we address the insights gained from magnetic property analysis of fault rocks and compare the magnetic methods with other approaches, the core of this review. Thereafter, we identify some of the current challenges in fault magnetism research and propose potential avenues that would contribute to a full appreciation of the magnetism of fault rocks and would advance our understanding of faulting.

2. Formation of Fault Rocks and Processes During Faulting

A fault is a narrow zone of crushed rocks along which two blocks of rock have moved alongside each other in response to stress imposed on the rock. This movement, that is, the very faulting, takes place either as creep: stable, slow sliding, or in the form of a series of earthquakes: unstable, fast slip intertwined with long periods of no motion. Faults thus accommodate strain on a momentous range of dimensions: on a spatial scale, from millimeters to hundreds of kilometers (for major plate boundaries), while also the time intervals range widely from seconds to minutes of earthquake slip, to years of slow, aseismic slip, and to millions of years of intermittent activity (e.g., Nielsen, 2017; Sibson, 2003). The textures and structures that develop in fault rocks depend on the amount and rate of shearing, and the physical conditions, that is, temperature and pressure, under which the shearing occurred. Fault zones that develop within and above the seismogenic zone are often characterized by highly localized brittle shear deformation (Figure 1a); they are termed brittle faults. In contrast, faults formed at much deeper levels in the crust tend to deform by purely thermally activated creep mechanisms and are characterized by continuous ductile displacement; they are termed ductile faults (e.g., Scholz, 2019). As depth increases, a fault zone is expected to encounter a gradual transition from brittle to ductile deformation, occurring in a depth interval with temperatures spanning from a few tens to hundreds of °C (typically 400–650°C, depending on the fault rock composition). It is usually termed the "brittle-to-ductile" transition zone (e.g., Aharonov & Scholz, 2019; Kawamoto & Shimamoto, 1997). The "brittle-to-ductile" transition zone also defines the lower limit of seismic activity on faults since ductile deformation is largely aseismic (Aharonov & Scholz, 2019).

The terminology and classification of fault rocks are not universally agreed upon yet (Woodcock & Mort, 2008). Fault rocks formed above a depth of 1–4 km are generally incoherent, friable, and uncemented; they include fault breccia and fault gouge (Figure 1a). At greater depth (up to 10–15 km), typical fault rocks are different types of cataclasites, sometimes with pockets of pseudotachylyte that were formed during seismic slip events (e.g., Sibson & Toy, 2006). The cataclasite group is subdivided according to the relative proportion of fine-grained matrix into protocataclasite, (meso)cataclasite, and ultracataclasite (Figure 1b; e.g., Brodie et al., 2007; Woodcock & Mort, 2008). A similar classification also applies to mylonite as the fault rock type for ductile deformation at greater depth (Figure 1b). The "brittle-to-ductile" transition zone, as the name suggests, is characterized by mixed mode of fault slip behavior and by extensive juxtaposing and overprinting of different types of fault rocks, such as mylonite with pseudotachylyte interlayers and mylonitized pseudotachylyte (e.g., Hayman & Lavier, 2014; Menegon et al., 2017; White, 1996).

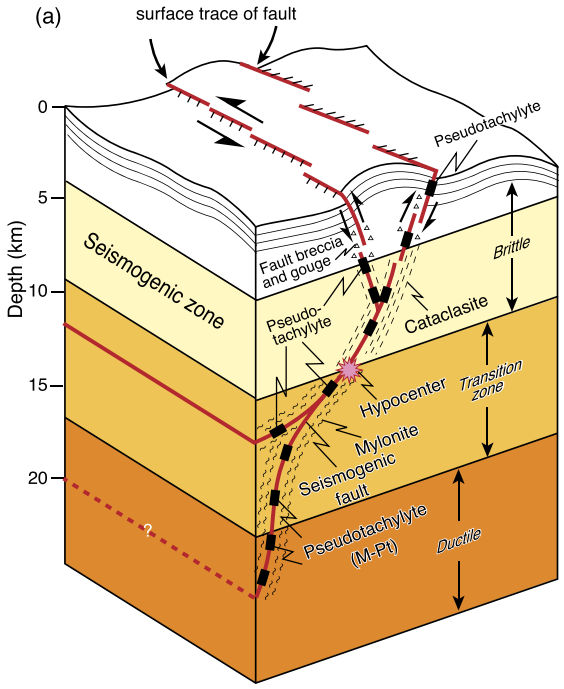

(b)

		non-foliated	foliated
> 30% large clasts (> 2mm)	75-100% large clasts (> 2mm)	fault breccia: **crackle breccia**	
	60-75% large clasts (> 2mm)	fault breccia: **mosaic breccia**	
	30-60% large clasts (> 2mm)	fault breccia: **chaotic breccia**	
< 30% large clasts (> 2mm)	incohesive[1]	**fault gouge**	
cohesive	glass or de-vitrifiled glass	**pseudotachylyte**	
cohesive	0-50% matrix (< 0.1 mm)	**protocataclasite**	**protomylonite**
cohesive	50-90% matrix (< 0.1 mm)	**(meso)-cataclasite**	**(meso)-mylonite**
cohesive	90-100% matrix (< 0.1 mm)	**ultracataclasite**	**ultramylonite**
cohesive	pronounced grain growth		**blasto-mylonite**[2]

[1] incohesive at present-day outcrop
[2] some blastomylonites have >30% large porphyroclasts

Figure 1. (a) Sketch illustrating the occurrence of diverse fault rocks in the shallow crust (reproduced from A. Lin et al., 2005). Fault breccia, fault gouge, and cataclasite mostly occur in the brittle regime; in contrast, mylonites develop within the ductile regime. Pseudotachylytes are frozen melt pockets occasionally formed by seismic frictional heating during large earthquakes. (b) A revised classification of fault rocks as suggested by Woodcock and Mort (2008). The brittle versus ductile behavior of rocks depends, to a large extent, on strain rate. The delineation of brittle and ductile zones here reflects expected behavior under typical geological strain rates of 10^{-14} s^{-1}.

Figure 2 summarizes the formation stages of a typical brittle fault (e.g., Hattori & Yamamoto, 1999): (i) increased stress produces a cross-joint system over the rock body (Figure 2a); (ii) rock fragments are formed by shearing along joints (Figure 2b); (iii) movements of the host blocks in a bookshelf-style mode rotate these fragments and abrase them to sand-, silt-, and clay-size particles, even down to micron/nanometer-size particles (Figure 2c); (iv) cementation of disintegrated fragments and subsequent formation of new joints (Figure 2d) with one or more cycles of refracturing (Figure 2e); and eventually (v) a relatively narrow zone (millimeters to centimeters thick) composed of very fine grained particles is produced (Figure 2f). The fault growth process commonly results in a fault zone architecture consisting of a so-called fault core enclosed by broader damage zones (Figure 2g; Caine et al., 1996; Chester et al., 1993).

The fault core is the result of highly localized strain and intense shearing that accommodates the majority of the displacement within the fault zone. It typically consists of a number of (recurring) slip surfaces and several types of fault rocks, such as fault breccia, fault gouge, and/or cataclasite (Caine et al., 1996; Chester et al., 1993; Choi et al., 2016; Sibson, 2003). The principal slip zone (PSZ) cuts the fault core (Figure 2g); it is the foremost location where physicochemical processes take place as a result of individual earthquake events (Boullier, 2011; Sibson, 2003). Examples of fault rocks from the first borehole of the Wenchuan earthquake Fault Scientific Drilling project (WFSD-1) are shown in Figure 2 (Wang et al., 2014).

The damage zone enveloping the fault core (Figure 2g) is characterized by what is referred to as distributed deformation (i.e., where homogenous strain is distributed across a network of evenly spaced faults, cf. Nixon et al., 2014). The damage zone differs structurally, mechanically, and petrophysically from the undeformed host rock or protolith (Caine et al., 1996; Chester et al., 1993; Choi et al., 2016). The host rock surrounds the damage zone and remains basically unchanged during faulting (Caine et al., 1996). As mentioned earlier on, a fault undergoes cycles of creep and seismic slip. A seismic cycle is divided into three periods: (1) the coseismic period (the time during an earthquake itself, typically seconds to minutes), (2) the postseismic period (days, months, and sometimes years after a given earthquake), and (3) the interseismic period (the time

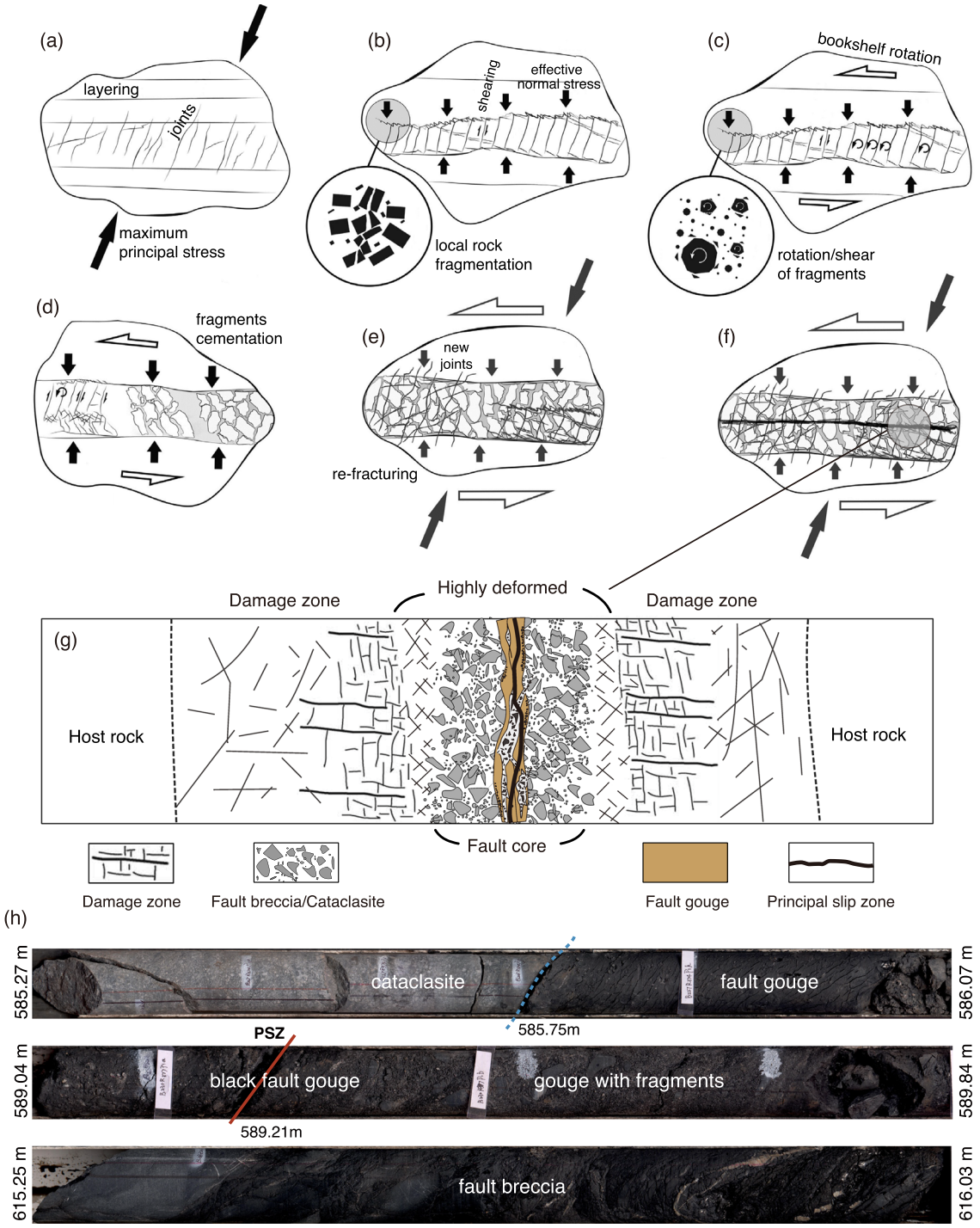

Figure 2. (a–f) An idealized schematic model showing the development of a brittle fault zone (modified after Hausegger et al., 2010, and Billi, 2005) and (g) the typical architecture of a fault zone (after Chester et al., 1993, and Caine et al., 2010). A brittle fault zone is the result of several deformation processes: (a) formation of cross joints, (b) fracturing of initial rocks and fragmentation, (c) fracturing and disintegration of fragments by bookshelf rotation, (d) cementation of disintegrated fragments, (e) subsequent formation of new joints due to the refracturing, and (f) eventually a relatively narrow zone (i.e., principal slip zone, PSZ) is formed composed of very fine grained particles. (g) Typical fault zone structure consisting of the fault core that includes fault gouge cut by the PSZ, fault breccia, and/or cataclasite, the damage zone surrounded by undeformed host rock (protolith). The figure is not to scale. (h) Examples of different fault rocks, which were retrieved from the first borehole of the Wenchuan earthquake Fault Scientific Drilling project (WFSD-1) (adapted from Wang et al., 2014). The blue and red lines indicate the boundary between cataclasite and fault gouge, and the inferred PSZ of the 2008 *Mw* 7.9 Wenchuan earthquake, respectively. The numbers on both sides of the cores indicate the depth intervals they were retrieved from.

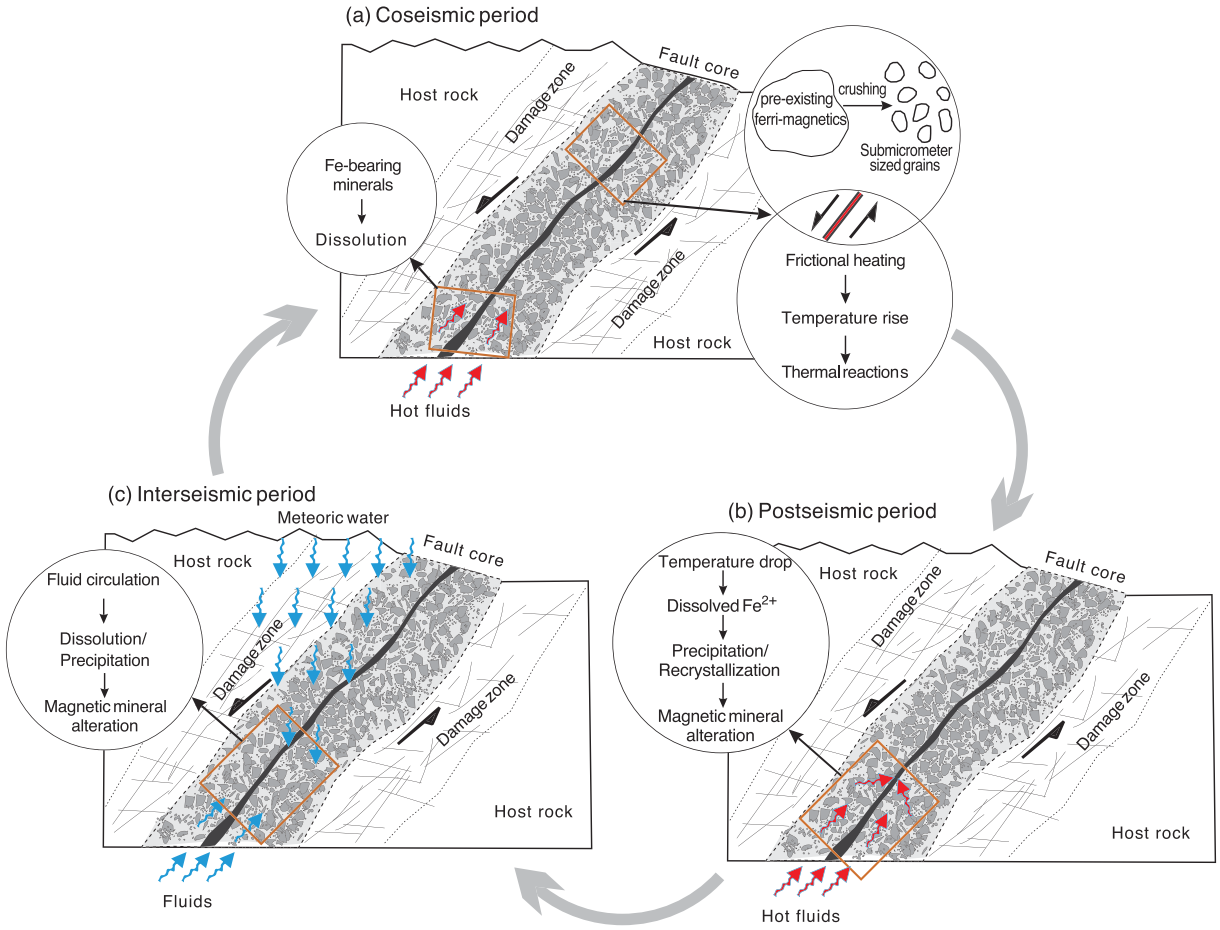

Figure 3. A conceptual model showing the faulting-related physical and chemical processes and the causes of potential magnetic changes in a fault zone during the different stages of the earthquake cycle. (a) During a coseismic period, the high rate seismic slip may crush the ferrimagnetic grains (if present) in the PSZ (indicated by the dark band) to a much finer size, due to the comminution of rock fragments. Meanwhile, frictional heating raises the temperature and can induce a myriad of thermochemical reactions within a fault zone, which include transformations of Fe-bearing minerals with immediate bearing on magnetic properties. Coseismic hot fluids and those from deeper down may dissolve the Fe-bearing minerals and release mobile Fe^{2+}. (b) During a postseismic period, neoformation of ferrimagnetic minerals occurs through precipitation of the mobilized Fe^{2+} as mixed ferrous-ferric iron oxide. Further, several thermochemical reactions may proceed during cooling of the fault fluids warmed by friction in the PSZ. (c) During an interseismic period, infiltration and percolation of meteoric water and/or deep-layer fluids into the fault zone may dissolve (part of) the Fe-bearing minerals again and induce precipitation of new magnetic minerals. A fault zone is the cumulative product of many earthquake cycles. The fault core cartoons are modified after Gray et al. (2005).

span between large earthquakes, lasting tens to thousands of years). A fault zone is the cumulative product of multiple slip cycles (Figure 3). In the following, we summarize some of the processes active in fault zones during the seismic cycle with bearing on the magnetic properties of fault zones.

Thermochemical reactions and pseudotachylytes. During an earthquake (Figure 3a), the mechanical energy due to the high seismic slip rates is converted into heat; it constitutes the largest part (~80% to 90%) of the total earthquake energy budget (Pittarello et al., 2008; Scholz, 2019). Frictional heating will quickly raise the temperature in the slip zone after rupture (Rice, 2006). Considering typical seismic slip rates (1 m/s) and total slip distance (tens of centimeters to meters) at a fault plane, the related temperature rise is <100°C near Earth's surface but can become >1100°C at seismogenic depths (>5 km) (e.g., McKenzie & Brune, 1972). The temperature rise may promote thermal decomposition or dehydration of certain mineral phases and the formation of breakdown products (e.g., Di Toro et al., 2011, Figure 3a). This also pertains to the magnetic minerals (see section 4.3 for a detailed discussion). The temperature rise within the slip zone is sometimes sufficient to trigger melting of the host rock minerals (typically >1000°C, e.g., Spray, 2010). Quick, quench cooling of these local melt pockets of millimeter to decimeter scale produces glasses or partly devitrified glasses, called pseudotachylytes (Figure 1a; e.g., A. Lin, 2008; A. Lin et al., 2005; McKenzie & Brune, 1972; Philpotts, 1964;

Sibson & Toy, 2006; Spray, 2010; Swanson, 1992). One should realize that the wording pseudotachylyte is also in use to describe any aphanitic, dark colored fault rock or amorphous material formed during shear deformation (see Rowe & Griffith, 2015). Throughout this review, however, we restrict pseudotachylytes to rocks with a frictional melt origin. Pseudotachylytes commonly have a relatively high concentration of fine-grained magnetite as a result of oxidation of melt-susceptible mafic minerals (e.g., Ferré et al., 2005; Nakamura et al., 2002; O'Hara, 2001; Pittarello et al., 2012; Zhang et al., 2018). This makes pseudotachylytes stand out magnetically, in comparison with their host rocks, so that they are attractive rocks for magnetic characterization (see section 4.4 for a detailed discussion).

Fluid movement in fault zones. Fault zones feature a dense network of fractures and secondary faults and thus act as major fluid conduits in the crust (Bense et al., 2013; Vermilye & Scholz, 1998). Fluids of multiple sources, including meteoric waters, trapped formation brines, mineral dehydration, and volatiles from the deep underlying layers (Hickman et al., 1995; Zoback et al., 2007), can infiltrate into and percolate along fault zones. Overpressurization may occur promoting earthquake nucleation (e.g., Miller, 2013; Scuderi & Collettini, 2016; Sibson, 1992); pore fluid pressurization during frictional heating flashes may induce fault weakening lengthening fault slip time spans (e.g., J. Chen et al., 2017; Miller, 2013; Rice, 2006). Importantly, fluid-related dissolution-precipitation processes are anticipated to be common during all periods of the seismic cycle, that is, the coseismic, postseismic, and interseismic periods (Figure 3; e.g., Bense et al., 2013; J. Chen et al., 2013, 2016; Gratier et al., 2013). This is discussed in section 4.5. These reactions play a critical role not only in physical, chemical, and mechanical evolution of fault rocks (Bradbury et al., 2015; J. P. Evans & Chester, 1995; Goddard & Evans, 1995; Isaacs et al., 2007; Niwa et al., 2015; Sutherland et al., 2012) but also in the very earthquake rupture (Hickman et al., 1995; Sutherland et al., 2012; Zoback et al., 2007).

Earthquake lightning. It is also reported that during large earthquakes (usually with $Mw > 5$), the crustal deformation activates and releases gases and/or electrical charges. These subsequently generate atmospheric electric fields and currents, which in turn affect the atmospheric electric circuit possibly resulting in luminous phenomena (e.g., Derr, 1973; Enomoto et al., 2017; C.-L. Kuo et al., 2011; Lockner et al., 1983; St-Laurent et al., 2006). This transient coseismic electric phenomenon is referred to as earthquake lightning (EQL), which travels along the fault plane and may produce anomalous magnetizations in fault rocks (e.g., fault gouges and pseudotachylytes; Enomoto & Zheng, 1998; Enomoto et al., 2001; Ferré et al., 2005). The mechanisms and magnetic effects are discussed in section 4.6.

All in all, a fault zone should be considered an extremely dynamic system, characterized by specific physicochemical conditions during each of the faulting stages (Figure 3; e.g., Cerchiari et al., 2020; Wibberley et al., 2008). For example, the redox state associated with faulting and accompanying fluid flow varies enormously during seismic slip events (Ishikawa et al., 2008; Yamaguchi et al., 2011). Also, fault rocks are subject to multiple deformation events, often under different physicochemical conditions. Consequently, a fault rock is not simply a granulated product of its protolith but is among the most complex and heterogeneous geological materials. It may be viewed as a low- to medium-grade metamorphic rock (J. P. Evans & Chester, 1995).

Iron features three main valence states, zerovalent, ferrous, and ferric iron (along with several more exotic intermediate forms) and is therefore a sensitive probe of the physicochemical conditions within fault zones. Iron cycling as a consequence of faulting would cause deposition, leaching, and/or chemical alteration of the Fe^{2+} and/or Fe^{3+} in Fe-bearing minerals in fault zones. Very reducing conditions could lead to metallic iron. In principle, this leads to measurable changes in magnetic properties, making rock magnetism a suitable probing technique to decipher faulting processes. Unraveling the magnetic properties of fault rocks thus provides important clues to understand the evolution of fault zones. Also, aspects of earthquake physics and chemistry may be unveiled. In the following section (section 3) we outline the merits of the rock magnetic or mineral magnetic methodology (with emphasis on fault rocks) before detailing the drivers of magnetic changes in fault rocks (section 4).

3. Rock and Mineral Magnetism of Fault Rocks

"Magnetic minerals" or ferromagnetic minerals (sensu lato) refer to minerals that are magnetic at room temperature: iron-titanium oxides, some iron sulfides, and metallic iron; the latter, however, rarely occurs in the Earth's crust. Coupled electron spins over large atomic distances in the crystal structure result in collective

spin behavior. Each magnetic mineral has a magnetic ordering temperature above which it loses its collective magnetism and becomes a paramagnet; on cooling through the ordering temperature the collective magnetic behavior is restored. At low temperatures below ~10–20 K, however, many more minerals order magnetically and low-temperature magnetic instrumentation can evaluate also those minerals.

The magnetic assemblage, concentration of each magnetic mineral, and magnetic granulometry of fault rocks reflect faulting processes. The rock's magnetic features are sensitive to both chemical and physical changes occurring in rocks during the faulting. For example, variations in physical grain size are often reflected in the magnetic granulometry, which is the (inferred) grain-size distribution of magnetic particles in a sample, usually expressed through the dominant magnetic domain structure (Figure 4a). A particle's domain structure is the result of minimizing the overall particle energy of individual magnetic particles. The domain structure or state depends on the size and shape of the magnetic particles, next to being temperature dependent. Crystal defects and the internal stress distribution in the magnetic grains also have their impact on the domain state (Özdemir & Dunlop, 1997), which may be particularly relevant for rocks and minerals that have undergone faulting.

We now provide (approximate) size ranges for the domain state types distinguished for magnetite, by far the most common magnetic mineral in nature. At room temperature, the smallest particles, with a diameter of up to 25 nm are superparamagnetic (SP); they cannot retain a geologically stable natural remanent magnetization (NRM). Next in size, in the 30–80 nm range (for equant grains), particles are single domain (SD). Larger particles, up to a few μm in size, are featuring noncollinear spin structures and possibly even a few domains; they are termed classically pseudo single domain (PSD, Stacey & Banerjee, 1974) but probably more correctly should be referred to as "vortex state" particles (Schabes & Bertram, 1988; see also Almeida et al., 2016, who show examples of particles in a vortex state) as recently proposed by Roberts et al. (2017). SD and PSD or vortex particles are paleomagnetically most stable. Large grains, >5–10 μm or so, contain many domains and are termed multidomain (MD). The reader is referred to Appendix A for further explanation; textbooks include Dunlop and Özdemir (1997), M. E. Evans and Heller (2003), Stacey and Banerjee (1974), and Tauxe (2010). Next to size also particle shape exerts a critical control on domain state threshold sizes. For example, rod-like particles of 0.1 × 0.1 × 1 μm are SD, whereas equant particles of 1 μm can be MD (Figure 4a).

Various types of magnetic measurements and their combinations are used to determine the magnetic carrier(s), their concentration, and (magnetic) grain size. They are categorized along field-, frequency-, and temperature-dependent measurements. Measurement of various types of laboratory-induced remanent magnetizations, that is, anhysteretic remanent magnetization (ARM) and isothermal remanent magnetization (IRM), also yields important information. The fundamentals and applications of rock and mineral magnetism are documented in several textbooks (e.g., Dunlop & Özdemir, 1997; M. E. Evans & Heller, 2003; Maher & Thompson, 1999; Nagata, 1961; Stacey & Banerjee, 1974; Tauxe, 2010; Thompson & Oldfield, 1986) and review papers (e.g., Dekkers, 1997; Hunt et al., 1995; Q. S. Liu et al., 2012; Peters & Dekkers, 2003; Verosub & Roberts, 1995). Below we outline the more relevant approaches for the analysis of fault rocks. In a number of cases also nonmagnetic methods are utilized in concert with magnetic methods to constrain the latter's interpretation. Before describing those magnetic and nonmagnetic methods, however, some specifics on sample collection and preparation for magnetic studies on fault rocks need to be considered. Magnetic property analysis requires physical samples since magnetic changes due to faulting processes may be reflected on the mm to μm scale. This implies drilling and coring rocks through fault zones; borehole logging "only" enables tracking broader (magnetic) aspects of fault zones.

3.1. Samples for Magnetic Studies Into Fault Rocks

As mentioned above, fault zones are narrow zones with widths in the order of centimeters to meters. Particularly, the PSZs are much thinner, in many cases <1 cm (Sibson, 2003). Many fault zone studies, therefore, share a common denominator—only small amounts of sample are available. Such small amounts can be delicate for the more classical geochemical and mineralogical analyses. In contrast, a relatively small amount of material (< ~500 mg) with any shape (e.g., chip, powder, or drilling/cutting residue) is sufficient for a complete set of magnetic analyses. Thus, in principle, magnetic changes at a small scale allow for resolving the faulting-related behavior. Magnetic scanning may reveal changes at the μm scale.

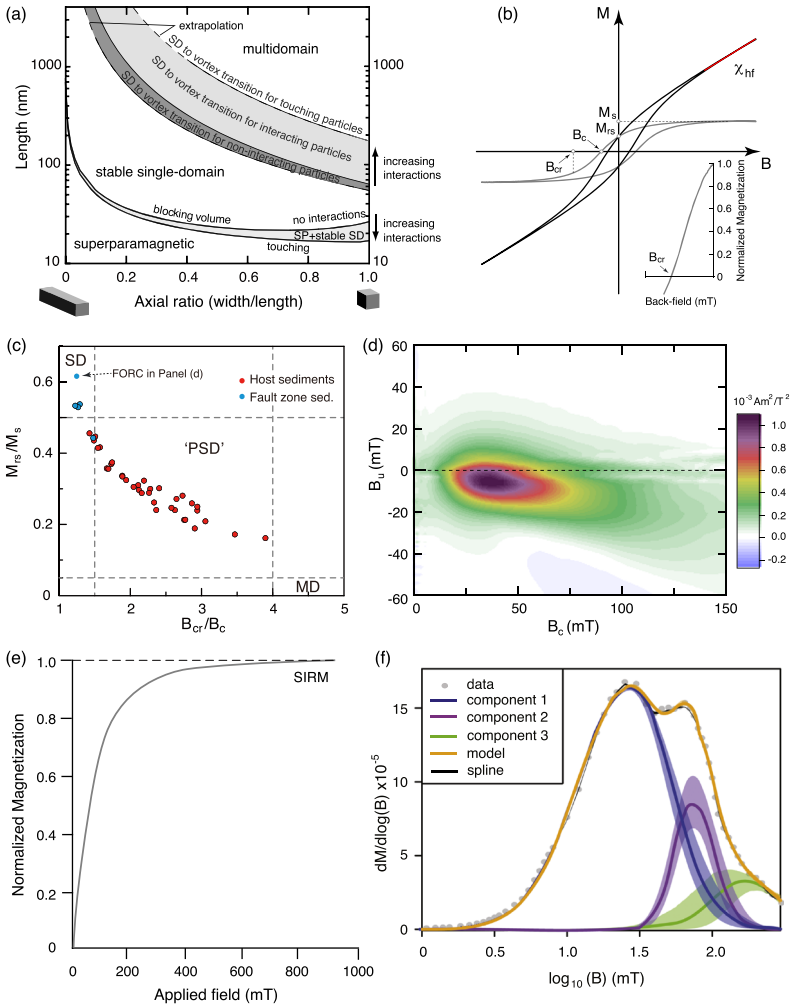

Figure 4. Domain states of magnetite as a function of grain size and shapes, and examples for commonly used plots for high-field magnetic measurements. (a) Illustration of the domain state categories for magnetite at room temperature and their relationship with shape and grain size of the magnetic particles (redrawn from Roberts et al., 2018). (b) Example of a hysteresis loop with definition of M_{rs}, M_s, B_c, and B_{cr}, with the inset showing a backfield demagnetization curve, with the definition of B_{cr}. The high-field slope (typically, $B > 0.7$ T) on the hysteresis loop is defined as high-field magnetic susceptibility (χ_{hf}). The dark and gray lines are the hysteresis loops before and after correction for the nonferrimagnetic matrix contribution, respectively. In this example the correction is a paramagnetic correction as χ_{hf} is positive. (c) Example of a Day plot of the hysteresis ratios M_{rs}/M_s and B_{cr}/B_c. Single domain (SD), pseudo single domain (PSD), and multidomain (MD) boundaries are after Day et al. (1977). Note that recent Day plots often use vortex rather than PSD following Roberts et al. (2018). The data points shown are host and fault zone sediments from the frontal prism in Japan Trench cored by the Integrated Ocean Drilling Program Expedition 343, Japan Trench Fast Drilling Project (JFAST) (reproduced from Yang et al., 2018). The host sediments lie mainly in the PSD (or vortex) field, whereas most of the fault zone samples are located in the SD region. (d) Example of a FORC diagram (first-order reversal curve) for one of the fault zone sediments (FZ697) shown in Figure 4c. B_c is equivalent to particle coercivity, and B_u to the local interaction field. Colors in the diagram represent absolute values of FORC density. The B_c peak centered at 30–40 mT with a prominent "kidney" shape toward higher coercivity suggests the occurrence of SD pyrrhotite. FORC data are from Yang et al. (2018) and are reprocessed with the FORCinel package (Harrison & Feinberg, 2008) with the VARIFORC (Egli, 2013) option used. VARIFORC smoothing parameters: vertical ridge Sc0 = 4, horizontal smoothing factor Sc1 = 7, central ridge Sb0 = 3, vertical smoothing factor Sb1 = 7, horizontal lambda $\lambda c = 0.1$, and vertical lambda $\lambda b = 0.1$. (e) Example of an isothermal remanent magnetization (IRM) acquisition curve. After application of a stepwise increasing magnetic field, the remanent magnetization increases until a maximum value is reached, which is termed saturation IRM (SIRM or M_{rs}). (f) Example of unmixing of an IRM acquisition curve to identify magnetic coercivity distributions using the MAX UnMix package (reprinted from Maxbauer et al., 2016). The sample is an anoxic lake sediment from Baldeggersee, Switzerland, and three coercivity components are identified: detrital magnetite-low coercivity component (Component 1), biogenic magnetite (Component 2), and oxidized magnetite (or hematite)—Component 3.

Anisotropy of magnetic susceptibility (AMS) and/or paleomagnetic studies of fault rocks (see sections 3.5 and 3.6 for details) require oriented samples. Classically, such samples are cylinders of 25 mm diameter × 22 mm height or 20 mm on-a-side cubes (known as standard-size samples), representing a volume deemed statistically representative. Due to the limited width of a fault zone, oriented sampling in a narrow fault zone is a challenge, and "contamination" by the host rock adjacent to the target layer(s) may complicate the interpretation. Also, bias may creep into AMS results due to the unconventionally small sample size dictated by fault rock samples. Almqvist et al. (2020), for example, found that the mean magnetic susceptibility and magnetic anisotropy degree (see section 3.5 for definitions) are inversely proportional with sample size for a set of pseudotachylyte cubes from western Jämtland (central Swedish Caledonides) ranging in volume between ~0.2 and ~0.03 cm^3. "Minicores" of 12 mm diameter × 11 mm long, cubic mini-AMS samples with 1 cm edges, or even down to a size of 3.5 mm on-a-side (hence ~250 times volumetrically smaller than standard-size samples), often work fine. AMS analysis of pseudotachylyte fabric on such 3.5 mm cubes enabled determining the focal mechanisms of ancient earthquakes (Ferré et al., 2015, 2016). Despite sample size issues for very small samples where a cautious and careful interpretation is appropriate, AMS studies on small samples are nonetheless a promising new avenue to unveil detailed geological features (Almqvist et al., 2020; Ferré et al., 2015, 2016; Zhu et al., 2017).

Berndt et al. (2016) demonstrated that samples with a thermoremanent magnetic moment larger than 10^{-11} Am^2 irrespective of their sizes (ranging from the centimeter scale to tens of nm scale) contain enough magnetic particles to be accurate magnetic recorders. Paleomagnetic measurements can thus also be carried out on smaller samples than the standard size samples. Millimeter-sized samples (e.g., Böhnel et al., 2009; Suttie et al., 2010) or even smaller samples of geological materials like single silicate crystals (e.g., zircon, plagioclase, and olivine crystals) can yield accurate paleointensity and paleodirection estimates using ultrahigh sensitivity moment magnetometry and advanced demagnetization techniques (e.g., Berndt et al., 2016; Fu et al., 2017; Sato et al., 2015; Tarduno et al., 2015). These include, but are not limited to, scanning SQUID (superconducting quantum interference device) microscopy (SSM; e.g., Weiss et al., 2007), quantum diamond magnetometry (QDM; e.g., Glenn et al., 2017), and microwave demagnetization (e.g., Suttie et al., 2010). This enables paleomagnetic analyses of the fault rocks. For such studies, oblique drilling across a fault zone may offer a way to orient the samples by making use of the present-day NRM overprint that is present in most samples.

3.2. Field-Dependent Measurements: Low-Field Magnetic Susceptibility

One of the most widely used room temperature magnetic measurements is the low-field magnetic susceptibility (volume specific: κ_{lf}, or mass specific: χ_{lf}), measured in small applied magnetic fields, typically, ~200–300 A/m; that is, several times the strength of the Earth's magnetic field (~25–50 A/m). It is a measure of the "magnetizability" of a sample and expresses in a general way the classes of magnetic materials (e.g., Dunlop & Özdemir, 1997): dominantly ferromagnetic or ferrimagnetic (very high χ_{lf}), paramagnetic (small positive χ_{lf}), or diamagnetic (very small negative χ_{lf}). A rock is an ensemble of ferromagnetic (sensu lato), paramagnetic, and diamagnetic minerals. Therefore, to characterize the ferrimagnetic (χ_{ferri}) component (s) (i.e., magnetite, pyrrhotite, or greigite) in samples, contributions from paramagnetic (χ_{para}), diamagnetic (χ_{dia}), and imperfect antiferromagnetic minerals (i.e., hematite and goethite) should be subtracted from the bulk low-field magnetic susceptibility (χ_{lf}). The imperfect antiferromagnetic minerals are often included in the paramagnetic contribution since their susceptibility does not differ that much. Magnetic susceptibility can also be measured at different frequencies of the applied alternating current (AC) field (typically varying between a few hundreds of Hz to a few kHz), yielding the frequency-dependent magnetic susceptibility, expressed either as a percentage of the low-field susceptibility (κ_{fd}%) or as a mass- (χ_{fd}) or volume-specific number (κ_{fd}). With increasing measurement frequency, the SP/stable SD (SSD) boundary (~25 nm at room temperature for a relaxation time of 100 s) shifts to smaller volumes. Hence, for a given grain-size distribution more grains become blocked at a higher measurement frequency and are SD with a lower susceptibility than SP particles, which explains the difference in susceptibility between the low and high measurement frequency. Frequency-dependent magnetic susceptibility is thus an effective way to determine the concentration of magnetic particles over a small grain size window across the SP/SSD boundary (e.g., Q. S. Liu et al., 2012).

The diamagnetic and paramagnetic magnetic moment increases linearly with applied field up to very high field values; hence, their susceptibility is constant for a given temperature. Also, magnetite's magnetization is linear with the applied magnetic field up to ~800 A/m, that is, the entire field range of low-field susceptometers. However, the magnetization of some other ferrimagnetic minerals, such as pyrrhotite, hematite, and titanomagnetite, shows a marked applied field dependence already in the low field of interest here (de Wall, 2000; Hrouda, 2011; Hrouda et al., 2006; Jackson et al., 1998; Worm et al., 1993). Variation of the magnetic susceptibility as a function of applied field can thus diagnose the presence of these magnetic minerals in fault zones. The bridge-type susceptometers are the most versatile and widely used instruments for susceptibility measurements. This includes field-, frequency-, and temperature-dependent magnetic susceptibility measurements, AMS measurements (see also section 3.5), and for some instruments, measurement of the in-phase and out-of-phase components of the magnetic susceptibility (e.g., Hrouda et al., 2016; Hrouda & Ježek, 2014).

3.3. Field-Dependent Measurements: High-Field Magnetic Measurements

3.3.1. Hysteresis Loops and FORC Diagrams

Magnetic hysteresis loops (Figure 4b) are not only informative of the magnetic mineralogy but also indicative of the dominant domain structure of magnetic minerals in the sample. Saturation magnetization (M_s) is the largest possible magnetization of a sample; it is thus a measure of the total amount of ferromagnetic minerals in the sample. The saturation remanence (M_{rs}) is the corresponding remanent magnetization after removal of the applied field. The coercivity (B_c) and remanent coercivity (B_{cr}) are measures of magnetic stability. The ratios M_{rs}/M_s and B_{cr}/B_c are commonly plotted on the so-called Day plot (Figure 4c; Day et al., 1977; Dunlop, 2002a, 2002b; Dunlop & Özdemir, 1997; Lanci & Kent, 2003) as indicators of domain states and, indirectly, grain size. As an alternative, the plot of M_{rs}/M_s versus B_c, referred to as "squareness plot" in the engineering literature, was proposed to avoid the need of determining B_{cr} and to remove potential ambiguities associated with the B_{cr}/B_c ratio: Particles with markedly different B_c values may have their B_{cr}/B_c largely overlaying complicating interpretation of the domain state (Tauxe et al., 2002). The Day plot is a classic rock magnetic tool and has been used extensively for domain state diagnosis since it was proposed by Day et al. (1977). However, several fundamental ambiguities associated with its interpretation have been documented recently by Roberts et al. (2018). Additional constraints, other than those offered by the Day plot, are required to properly interpret the hysteresis parameters (i.e., dominant domain state) in terms of physical grain size. Beyond the Day plot, the first-order reversal curve (FORC) technique has been developed to derive more information from hysteresis measurements (e.g., Roberts et al., 2000, 2006, 2014; Zhao et al., 2015). FORC diagrams (an example in Figure 4d) provide important insights into not only the magnetic minerals but also the distribution of coercivity and magnetostatic interactions among magnetic particles (see review by Roberts et al., 2014, for more details). Given the interpretive ambiguities in the Day diagram, unmixing of FORC diagrams (Lascu et al., 2015), and determination of remanent, transient, and induced FORC diagrams (P. X. Hu et al., 2018; Zhao et al., 2017) have been suggested as suitable candidates for diagnosing domain state on a component-by-component basis (Roberts et al., 2018). However, when samples are dominantly paramagnetic or antiferromagnetic with only a small ferrimagnetic contribution, the low signal-to-noise ratio prevents acquisition of meaningful FORC data, that is, the ferrimagnetic signal is weak in comparison to the total magnetization (e.g., Jackson & Solheid, 2010). For those samples hysteresis loop measurement with determination of the classic hysteresis parameters is still the foremost way to characterize their magnetic behavior. In addition, hysteresis measurements also allow for assessing the relative magnetic contribution of ferrimagnetic minerals and that of the matrix minerals (i.e., paramagnetic and/or diamagnetic) through comparison of the high-field magnetic susceptibility (χ_{hf}, i.e., the slope of the linear high-field segments of the hysteresis loop, cf. Figure 4b) and the low-field susceptibility (χ_{lf}) of a sample (Figure 4b).

3.3.2. Remanence Measurements at Room Temperature

High-field methods are most commonly used to identify magnetic mineral phases. IRM acquisition curves (Figure 4e) obtained at room temperature in successively increasing direct fields contain a wealth of information about magnetic hardness. Unmixing of IRM acquisition curves along with forward basis functions can provide information that is diagnostic of magnetic mineralogy (Figure 4f; Egli, 2004a, 2004b, 2004c; Kruiver et al., 2001; Maxbauer et al., 2016). Collections of IRM acquisition curves can also be subjected to end member modeling, an inverse bilinear unmixing approach (Heslop & Dillon, 2006; Weltje, 1997).

The end members then serve as basis for a geological interpretation of the variability in the IRM acquisition curves. It has been used for paleoenvironmental analysis, the detection of magnetotactic bacteria (e.g., Just et al., 2012), and in the context of remagnetization, the (partial) resetting of the NRM in rocks at some point during their geological history (e.g., Aben et al., 2014; Gong et al., 2009; Huang et al., 2015).

ARM is generated by placing a sample in a small steady direct current (DC) field, the DC bias field (of the order of the Earth's magnetic field), and superimposing an AC field of which the amplitude is steadily ramped down from a preset initial value to zero. It is a useful laboratory technique for characterizing magnetic particles (Q. S. Liu et al., 2012). It senses SD magnetite particularly well. The different behavior of ARM and χ_{lf} with grain size make plots of ARM versus χ_{lf} (i.e., the Banerjee diagram, Banerjee et al., 1981) or χ_{ARM} (χ_{ARM} = ARM/DC bias field) versus χ_{lf} (i.e., the King diagram, King et al., 1982) useful for detecting grain size changes, in particular for magnetite.

Another rock magnetic parameter, which is often employed to measure the relative contributions of low and high coercivity material to a sample's saturation isothermal remanent magnetization (SIRM), is the S-ratio. It compares the SIRM obtained in a saturating forward field with the IRM obtained subsequently in a suitable backfield (usually a reversed field of 0.3 T, yielding $IRM_{-0.3T}$). The classic S-ratio, $S_{classic}$, is defined as (e.g., Thompson & Oldfield, 1986) follows:

$$S_{classic} = -IRM_{-0.3T}/SIRM \quad (1)$$

It scales from −1 (only high coercivity material) to 1 (only low coercivity material). It can also be defined as (Bloemendal et al., 1992) follows:

$$S = (1 - IRM_{-0.3T}/SIRM)/2 \quad (2)$$

or

$$S_{forward} = IRM_{0.3T}/SIRM \quad (3)$$

where the $IRM_{0.3T}$ is remanent magnetization acquired in a forward field of 0.3 T. The S-ratios in Definitions (2) and (3)—the latter is also called "forward S-ratio" (Heslop, 2009)—scale from 0 to 1; they provide a measure of the relative contribution of the low coercivity material to the total remanence. It should be realized that numeric values of Definition (1) on the one hand versus (2) and (3) on the other are different and cannot be used interchangeably without the definitions being specified. When the S-ratio approaches unity, in general, ferrimagnetic minerals are dominant over antiferromagnetic minerals, and vice versa. However, it is important to note that variations in the relative concentration of high- and low-coercivity phases are nonlinear and interpretation of the S-ratio is nonunique, because it is not solely a function of mineral type but is also influenced by factors such as grain size and substitution. The S-ratio is an example of so-called closed data (i.e., data within certain bounds like fractions or percentages); the additive-log-ratio transform (e.g., Swan & Sandilands, 1995) has been suggested to obtain meaningful descriptive statistics for the S-ratio information (Heslop, 2009).

3.4. Temperature-Dependent Magnetic Measurements

3.4.1. High-Temperature Magnetic Measurements

High-temperature magnetic analyses, either in-field measurements or remanence measurements, are among the most diagnostic measurements for assessing magnetic mineralogy because magnetization decreases with increasing temperature and becomes 0 at and above the magnetic ordering temperature since the magnetic mineral has become a paramagnet. The magnetic ordering temperature is named Curie temperature (T_C) for ferromagnet and ferrimagnet and Néel temperature (T_N) for imperfect antiferromagnetic materials (Dunlop & Özdemir, 1997). For example, magnetite and hematite have T_C and T_N values of 578°C (Figure 5a) and 675°C (Figure 5b), respectively (Dunlop & Özdemir, 1997). The magnetite-ulvöspinel (Fe_3O_4-Fe_2TiO_4) solid solution series and the hematite-ilmenite (α-Fe_2O_3-$FeTiO_3$) solid solution series show a marked range in ordering temperatures respectively from 578°C to −153°C (T_N of ulvöspinel) and from 675°C to −233°C (T_N of ilmenite) (Dunlop & Özdemir, 1997). With increasing Ti substitution ordering temperatures decrease approximately linearly. Goethite has a T_N of ~120°C (Figure 5c), which decreases below room temperature with increasing Al substitution (Q. S. Liu et al., 2006). Goethite can accommodate up to ~32 mol% Al substitution with a corresponding magnetic ordering temperature of

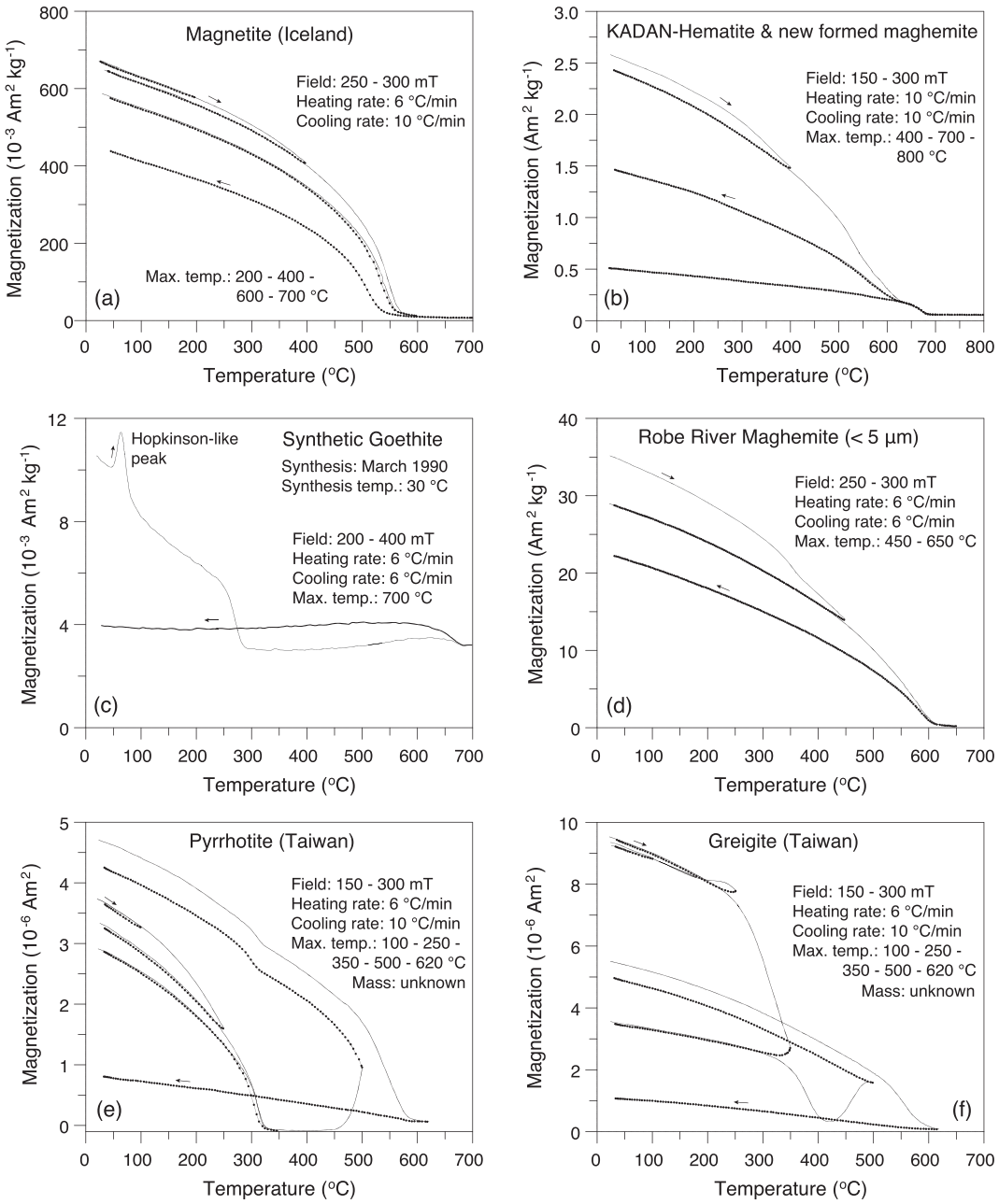

Figure 5. Examples of thermomagnetic curves of some common magnetic minerals, showing their high-temperature behavior including Curie or Néel temperatures. "Stepwise" thermomagnetic analyses were performed in air with a modified horizontal translation Curie balance (Mullender et al., 1993) in Paleomagnetic Laboratory Fort Hoofddijk, Utrecht University (The Netherlands). Details on samples, heating/cooling rates, temperature cycles, and applied fields are given in each panel. Kadan hematite (panel b) is from the Czech Republic and Robe River maghemite (panel d) is from Western Australia. The Hopkinson peak (panel c) is a manifestation of superparamagnetism: the coercivity of the goethite is very high (tens of teslas at room temperature) in comparison of the field range used in the thermomagnetic analysis. Then the magnetic moment can be considered a "low-field" susceptibility which goes through a maximum at the Néel/Curie temperature.

−58°C (Murad & Bowen, 1987). Maghemite has a T_C of 645°C (Figure 5d; Özdemir & Banerjee, 1984), but it often inverts to hematite before the T_C is reached: Depending on grain size and amount of substitution maghemite can invert to hematite at any temperature between 250°C and 1000°C (Dunlop & Özdemir, 1997). A typical inversion range for fine-grained maghemite is between 300°C and 400°C (e.g., Q. S. Liu et al., 2005). Monoclinic pyrrhotite has a T_C of 325°C (Figure 5e); T_C is slightly lower for

Ni-substituted pyrrhotite (Kontny et al., 2000; Schwarz & Vaughan, 1972). T_C remains undetermined for greigite because greigite decomposes before the T_C can be measured (like the situation of maghemite): It exceeds 400°C (Roberts et al., 2011). Diagnostic for greigite is its thermochemical alteration to a nonmagnetic phase starting at ~200°C and finishing at ~350°C when heated in air (Figure 5f; Dekkers et al., 2000; Reynolds et al., 1994; Roberts, 1995; Torii et al., 1996). At higher temperatures, above 400°C magnetite forms which in turn is converted to hematite above 500–550°C yielding the typical "greigite-in-air" thermomagnetic signature. To date, greigite has not been reported in fault rocks; however, discrimination between greigite and pyrrhotite is essential for fault zone magnetic studies, as the latter is commonly present as product of thermal alteration of pyrite in fault zones. In addition, with stepwise thermal demagnetization of three orthogonal IRM components the thermal behavior of high-, intermediate-, and low-coercivity magnetic phases can be evaluated separately (Lowrie, 1990).

3.4.2. Low-Temperature Magnetic Measurements

A major disadvantage of high-temperature measurements is that the magnetic signal may be obscured by newly formed magnetic mineral(s) during the thermal treatment. This applies to in-field measurements in particular. During measurements at low temperature, down to 4 K, thermochemical alteration is nonexistent because the sample is not heated. Therefore, low-temperature measurements are increasingly utilized in rock magnetism (Dunlop & Özdemir, 1997; Q. S. Liu et al., 2012; Moskowitz et al., 1998; Rochette et al., 1990). They are designed to determine magnetic ordering temperatures below room temperature and whether or not so-called low-temperature transitions in magnetic minerals occur. For example, the well-known Verwey transition (T_V) at ~120 K or −153°C (Figure 6a; Verwey, 1939) is diagnostic of magnetite, when it undergoes a crystallographic phase transition from a cubic to a monoclinic structure. Similarly, the Morin transition (T_M, ~250 K) at which hematite's magnetic structure undergoes a spin flop, a change in orientation with respect to its crystal structure, is a key indicator of the presence of (crystalline) hematite (Figure 6b; Morin, 1950). Monoclinic pyrrhotite exhibits the Besnus transition at 30–34 K (Figure 6c; Besnus & Meyer, 1964; Dekkers et al., 1989; Rochette et al., 1990, 2011). Goethite shows an increasing magnetization with decreasing temperature (Figure 6d; Guyodo et al., 2006; Rochette & Fillion, 1989). The low-temperature behavior with possible magnetic transitions is usually measured with a so-called magnetic properties measurement system (MPMS); both in-field and remanent magnetizations are measured as a function of applied field and temperature between 1.8 and 400 K. The most commonly used measurement sequences and their advantages have been described in detail by Bilardello and Jackson (2013).

However, one must exercise caution when interpreting low-temperature data to avoid ambiguities as some minerals show similar features at the same temperature range. At low temperatures other Fe-bearing materials, for example, Fe or Mn carbonates (siderite ($FeCO_3$), and rhodochrosite ($MnCO_3$)) order magnetically at 37 and 34 K, respectively (Frederichs et al., 2003; Housen, Banerjee, & Moskowitz, 1996). Vivianite $Fe_3(PO_4)_2{\cdot}8H_2O$) orders as well below 20 K (Frederichs et al., 2003). Fe-bearing silicates (clay minerals, chlorite, amphiboles, and pyroxenes) may also order below 15–20 K because of low thermal vibration at those low temperatures. SP particles show distinctive low-temperature behavior (e.g., Chang et al., 2009); spin glasses may freeze in and iron oxide coatings around silicates may order below 50 K (e.g., Franke et al., 2007). Therefore, low-temperature measurements deliver very useful information, but their interpretation requires expert knowledge. One should perform more elaborate measurement strategies (e.g., Bilardello & Jackson, 2013; Kars et al., 2011) or combine the results with other magnetic and/or nonmagnetic measurements. A nice example is the study of Kars et al. (2011). Through applying a magnetic field of 5 μT inside the SQUID MPMS during the cooling of a room temperature SIRM to detect the presence of a magnetic ordering temperature, they successfully diagnosed siderite and rhodochrosite in overmatured claystones from a borehole in the Netherlands and in outcrop samples from the Borneo Prism; the previous interpretation of fine-grained pyrrhotite had to be abandoned.

3.5. Anisotropy of magnetic susceptibility and remanence

The magnetic anisotropy of rocks, that is, the magnetic properties of a given sample vary depending on the sample orientation, results from the contributions of ferromagnetic (sensu lato), paramagnetic, and diamagnetic minerals. Detailed coverage on the theoretical background, mineral sources, measurement procedures, quantification, geological applications, and advantages and limitations of AMS and anisotropy of magnetic remanence (AMR), hereafter collectively called "magnetic fabric," can be found in several textbooks and

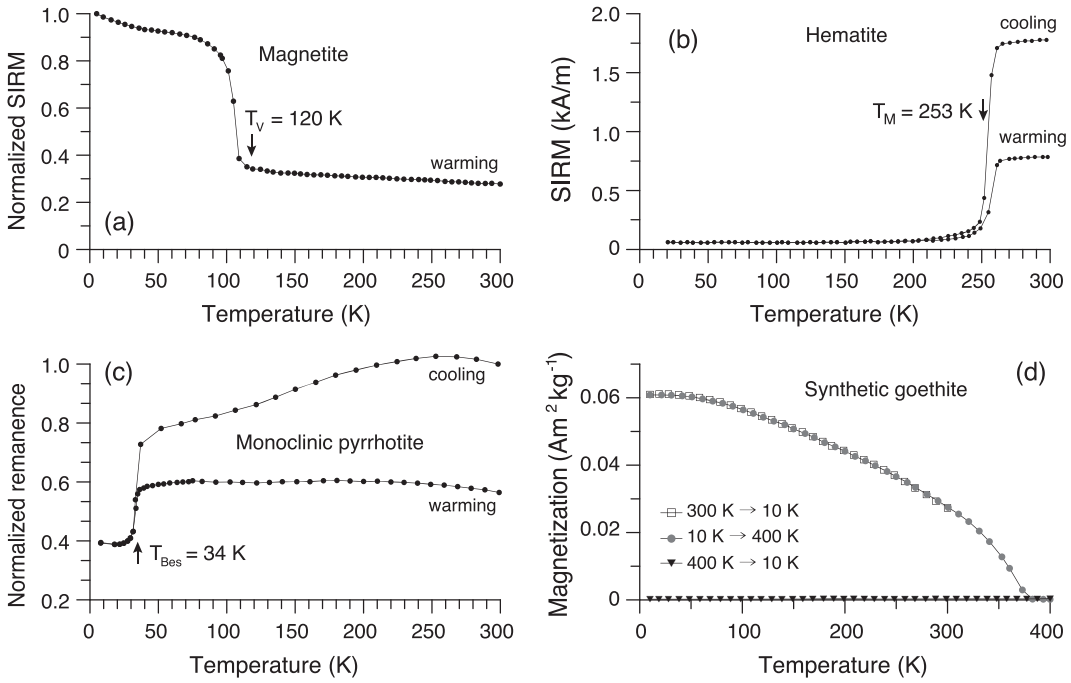

Figure 6. Low-temperature treatment of (S)IRM for some common magnetic minerals, showing the low-temperature transition of magnetite (a), hematite (b), and monoclinic pyrrhotite (c). (a) Warming curve of SIRM acquired in 2.5 T at 5 K of a 37 nm sized stoichiometric magnetite showing the Verwey transition (T_V) at ~120 K typical of magnetite (Verwey, 1939). Data are from Özdemir et al. (1993). (b) Low-temperature cycling of a 2.5 T SIRM at 300 K of a MD hematite crystal (0.24 mm × 2.15 mm × 3.2 mm in size) from Mount Wright, Québec (Canada), showing its Morin transition (T_M) at ~250 K (Morin, 1950). Data are from Özdemir et al. (2008). (c) Low-temperature cycling of SIRM imparted at 300 K with a 4 T field for monoclinic pyrrhotite illustrating the Besnus transition (T_{Bes}) at 30–34 K (Besnus & Meyer, 1964; Rochette & Fillion, 1988; Rochette et al., 1990). The sample with grain size of 250–150 μm was separated magnetically from a pyrite/pyrrhotite skarn collected from Temperino in Tuscany, Italy (Dekkers, 1988; low-temperature data are from Dekkers et al., 1989). (d) Low-temperature cycling (300–10–400–10 K) of an IRM acquired at 300 K in a 2.5 T field for a synthetic goethite sample showing its low-temperature magnetic behavior. Data are from Guyodo et al. (2006).

review papers (Borradaile & Henry, 1997; Borradaile & Jackson, 2004, 2010; Ferré, Gébelin, et al., 2014; Hirt, 2007; Hrouda, 1982; Jackson, 1991; Martín-Hernández et al., 2004; Martín-Hernández & Ferré, 2007; Parés, 2015; Potter, 2004; Rochette et al., 1992; Tarling & Hrouda, 1993). Below we briefly outline the rationale for AMS approaches.

AMS depicts geometrically the orientation and degree of alignment of the preferred orientations of mineral grains, the mineral grain spatial distribution or their lattice-preferred orientation, and the shape or crystalline anisotropy of the grains in a rock (Figures 7a and 7b; e.g., Ferré, Gébelin, et al., 2014; Martín-Hernández & Ferré, 2007). It is commonly expressed by a symmetric second-order tensor (Tarling & Hrouda, 1993) and described by a triaxial ellipsoid with principal axis' lengths equal to the eigenvalues of the magnetic susceptibility tensor, $\kappa_{max} \geq \kappa_{int} \geq \kappa_{min}$, which correspond to the maximum, intermediate, and minimum susceptibility axes, respectively (Figure 7b). The degree of anisotropy of the ellipsoid is measured by the parameter P (Nagata, 1961) or the "corrected" P, P_j (Jelínek, 1981), which are respectively defined as follows:

$$\kappa_{max}/\kappa_{min} \tag{4}$$

and

$$P_j = \exp\left\{2\left[(\ln\kappa_{max} - \ln\kappa_m)^2 + (\ln\kappa_{int} - \ln\kappa_m)^2 + (\ln\kappa_{min} - \ln\kappa_m)^2\right]\right\}^{1/2} \tag{5}$$

where κ_m is the mean magnetic susceptibility, $\kappa_m = (\kappa_{max} + \kappa_{int} + \kappa_{min})/3$. The shape of the ellipsoid is characterized by the parameter T (Jelínek, 1981), which is defined as follows:

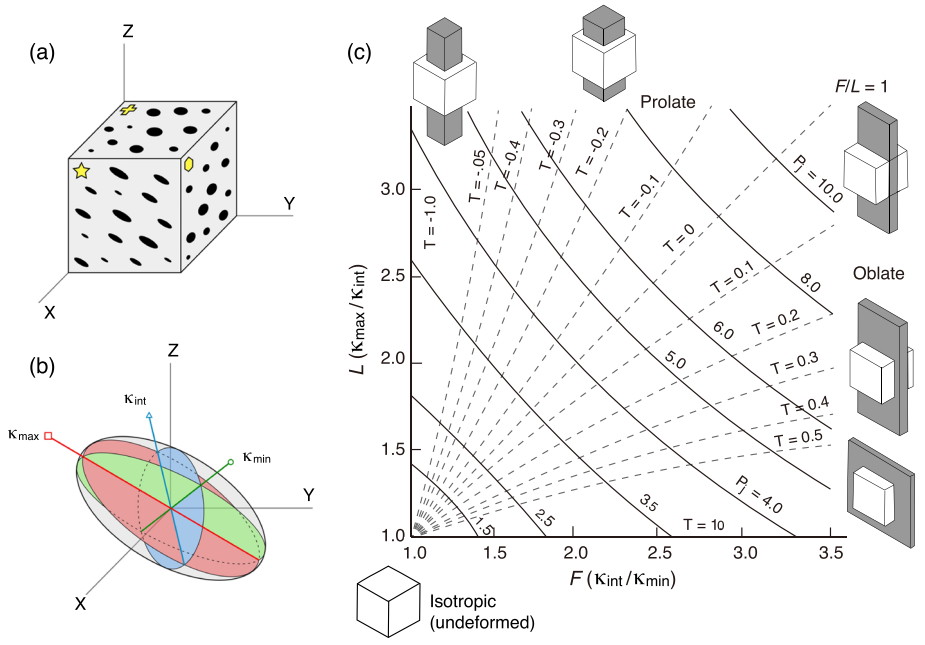

Figure 7. Principle of the AMS method for revealing petrofabrics. (a) A schematic diagram of a rock fabric. (b) The AMS ellipsoid is composed of three orthogonal principal axes: κ_{max}: maximum, κ_{int}: intermediate, and κ_{min}: minimum. The κ_{max} and κ_{min} axes, respectively, correspond to long and short axes of grains or crystals. (c) Flinn diagram of the lineation (L) versus foliation (F) illustrating the shapes of AMS ellipsoids in terms of the corrected degree of anisotropy (P_j, Tarling & Hrouda, 1993). The shape parameter (T) is also shown. Figures 7a and 7b are reprinted from Cho et al. (2015), and Figure 7c is modified from Dubey (2014).

$$T = 2\ln(\kappa_{int}/\kappa_{min})/\ln(\kappa_{max}/\kappa_{min}) - 1 \tag{6}$$

T ranges over the spectrum of ellipsoid shapes (Figure 7c): $0 \le T \le 1$ for oblate ellipsoids (disk shaped), $-1 \le T \le 0$ for prolate ellipsoids (rod shaped), and $T = 0$ for neutral ellipsoids. Along with T, the magnetic lineation L,

$$L = \kappa_{max}/\kappa_{int} \tag{7}$$

and magnetic foliation F,

$$F = \kappa_{int}/\kappa_{min} \tag{8}$$

are most informative to describe the AMS ellipsoid (Tarling & Hrouda, 1993). They are commonly plotted on a so-called Flinn diagram (Figure 7c; Flinn, 1965; Jelínek, 1981).

AMS can detect incipient deformation well before other strain indicators (e.g., Almqvist & Koyi, 2018; Burmeister et al., 2009). The low-field AMS, with assets of ease of data acquisition (minutes) and sensitivity (down to one per mille), has been used almost exclusively in classic petrofabric analysis studies (e.g., Borradaile, 1988; Graham, 1966; Hrouda, 1982; Martín-Hernández et al., 2004). In the context of fault rocks—of special interest here—we note the extensive review by Ferré, Gébelin, et al. (2014) on magnetic fabrics in ductile shear zones. In addition, measurement of AMS at high fields (e.g., Ferré et al., 2004; Hrouda & Jelínek, 1990; Kelso et al., 2002; Martín-Hernández & Ferré, 2007; Martín-Hernández & Hirt, 2001; Rochette et al., 1992), and temperature-dependent AMS (Issachar et al., 2016, 2018; Parés & van der Pluijm, 2014; Schmidt et al., 2007) have been proposed to separate the ferrimagnetic from the nonferrimagnetic (i.e., paramagnetic and diamagnetic) contributions to the AMS. Recently, frequency-dependent AMS was proposed to determine both the presence of SP particles and the relative tensor contributions of the SP and larger size fractions to the overall magnetic fabric (Hrouda & Ježek, 2014).

This would help to evaluate the occurrence of grain fining of preexisting magnetic particles as a consequence of the intensive shearing during earthquake slip (see section 4.2).

The measurement of magnetic remanence-related anisotropies is much more time consuming and therefore less utilized. It includes measurement of anisotropy of anhysteretic remanent magnetization (AARM) (e.g., Issachar et al., 2018; Jackson et al., 1991), anisotropy of isothermal remanent magnetization (AIRM) (e.g., Kodama & Dekkers, 2004; Stephenson et al., 1986), and anisotropy of thermal remanent magnetization (ATRM) (Borradaile & Lagroix, 2000; Hirt, 2007). Such AMR data have been suggested to be an efficient way to characterize the individual contributions of ferrimagnetic and antiferromagnetic minerals (Martín-Hernández & Ferré, 2007). Ferrimagnetic and paramagnetic/diamagnetic minerals in fault rocks are usually formed at different faulting stages and/or through different faulting-related process (e.g., frictional heating and fluid-rock interactions; see section 4). Those minerals, therefore, may reflect diverse deformation paths. Examination of AMR across a fault zone might thus help diagnosing the subfabric carried by the newly formed ferrimagnetic mineral(s) due to seismic frictional heating. Also, the thermal remanent magnetization (TRM) imprint across fault zones may be evaluated, providing insights into the dynamic deformation processes in a fault zone. The AMR techniques, including instrumental requirements, measurement strategy, and pros and cons compared to standard low-field AMS measurements, have been discussed in detail by Martín-Hernández and Ferré (2007).

3.6. Paleomagnetic Considerations

The NRM of rocks is constituted of one or several component(s) that as a rule of thumb represent(s) different times in the geological history of that rock. The same pertains to fault rocks: The faulting generates frictional heat that (partially) resets the existing NRM. To properly isolate these NRM components, stepwise alternating field or thermal demagnetization should be carried out with a sufficient number of demagnetization steps according to standard paleomagnetic practice (e.g., Tauxe, 2010). The NRM demagnetization behavior is visually inspected on vector endpoint plots (also referred to as Zijderveld plots; Zijderveld, 1967), and the paleomagnetic directions are typically determined with principal component analysis (Kirschvink, 1980). Different NRM components in fault rocks, especially the new so-called "secondary" component(s) formed during the rupturing itself (see section 4.7), may hold valuable information on faulting-related effects (e.g., Chou, Song, Aubourg, Lee, et al., 2012; Ferré, Geissman, et al., 2014; Leibovitz, 2016).

3.7. Nonmagnetic Measurement Techniques

Fault rocks contain mixed magnetic mineral assemblages of potentially different origin, grain size, and relative concentrations. Several types of magnetic measurements must therefore be used in concert to properly identify magnetic carriers and minimize ambiguities. In some cases, the magnetic results are supplemented by data acquired with what is referred to as "nonmagnetic techniques" to further unravel their nature and causal links to faulting processes. The most frequently used nonmagnetic techniques include, but are not limited to, the following: Mössbauer spectroscopy (e.g., Dyar et al., 2006), scanning electron microscopy (e.g., Reed, 2005), transmission electron microscopy (e.g., McLaren, 2005), X-ray diffraction analysis (e.g., Lavina et al., 2014), electron probe microanalysis (e.g., Reed, 2005), magnetic force microscopy (e.g., Grütter et al., 1995), electron spin resonance (e.g., Fukuchi, 2003; Pan & Nilges, 2014), and diffuse reflectance spectroscopy (e.g., Torrent & Barrón, 2008). All these measurements can provide important insights into the valency of Fe in minerals, preferred grain alignment, grain size, and geochemistry of Fe-bearing minerals, and help constraining the magneto-mineralogical interpretation.

4. Drivers for Changes in Magnetic Properties of Fault Rocks

As mentioned above, faulting is a complex process involving various physical and chemical changes, which complicates the interpretation of fault rocks by any type of measurement, thus including the rock magnetic approach reviewed here. The magnetic properties of fault rocks are determined by several mechanisms. In this section we focus on those for which a consensus has been reached. These include (i) strain-induced magnetic changes, (ii) grain-size variations of preexisting magnetic minerals by grain fining, (iii) thermochemical reactions induced by frictional heating, (iv) coseismic frictional melting with pseudotachylyte formation,

(v) chemical alteration and neomineralization due to fluid percolation, (vi) IRM acquisition due to EQL, and (vii) remagnetization of the NRM due to physicochemical processes.

4.1. Strain-Induced Magnetic Changes

Stress and related strain effects may have significant influence on magnetic properties of rocks. Stresses (differential or even hydrostatic) can directly affect the behavior of ferrimagnetic mineral grains, especially (titano-)magnetite through the effect of magnetostriction (also known as piezomagnetism; e.g., Bezaeva et al., 2015; Kapička, 1988, 1992; Kean et al., 1976). Strain may cause reorientation and/or internal deformation of ferrimagnetic grains (e.g., Borradaile, 1988; Till & Moskowitz, 2014). This would lead to changes in a variety of magnetic properties, the most important of which are magnetic anisotropy, changes in remanence orientation and intensity, and changes in bulk magnetic properties such as coercivity and magnetic susceptibility (e.g., Bezaeva et al., 2015; Borradaile, 1996; Gattacceca et al., 2007; Gilder et al., 2004, 2006; Jackson et al., 1993; Jiang et al., 2013; Kapička, 1988, 1992; Kapička et al., 2006; Kean et al., 1976; Louzada et al., 2010). For example, up to 25% shortening due to axial compression in a set of synthetic magnetite-bearing "calcite sandstone" samples irreversibly increases their coercivity and magnetic anisotropy but decreases their mean magnetic susceptibility and the remanence component parallel to the shortening axis (Jackson et al., 1993). Brittle or semibrittle fault rocks generally form in the upper ~10–15 km of the Earth's crust. The vertical effective stress at this depth interval is about 160–240 MPa, calculated from an average rock density (2,600 kg m^{-3}) under the assumption of hydrostatic pore fluid pressure. The stress sensitivity of magnetic susceptibility for various rocks ranges roughly from 0.8 to 1.3×10^{-3} MPa^{-1} (unit: one over pressure per unit area; e.g., Kapička, 1988; Kean et al., 1976). The stress may induce decreases in a rock's magnetic susceptibility ranging from 12% to 30%, if only the vertical effective stress is taken into consideration. In this context, the potential stress effects on magnetic properties of fault rocks cannot be ignored, at least not in seismogenic zones. It has been documented that changes in magnetization of stressed rocks due to local accumulation of stress may induce transient anomalies in the local geomagnetic field prior to an earthquake, referred to as piezomagnetism or tectonomagnetism (e.g., Sasai, 2001; Yamazaki, 2013).

However, an interpretation is complicated by many factors, such as variations in magnetic carriers (magnetic mineralogy, concentration, and grain size), ambient magnetic field, stress loading pattern (e.g., hydrostatic or uniaxial, shock or static, single or cycling), and duration (e.g., Gilder et al., 2006, 2018; Kapička, 1992; Louzada et al., 2010; Volk & Feinberg, 2019). For example, pressure loading removes part of the remanent magnetization of a rock when the pressure is applied in a zero ambient magnetic field, a procedure conveniently termed pressure demagnetization (e.g., Bezaeva et al., 2010; Gattacceca et al., 2007; Jiang et al., 2013; Louzada et al., 2010, 2011; Pozzi, 1975; Volk & Feinberg, 2019; Volk & Gilder, 2016). The higher the pressure, the more remanence is removed. A detailed compilation of the available experimental pressure demagnetization data on (titano-)magnetite-, (titano-)hematite-, and pyrrhotite-bearing rocks is provided in Louzada et al. (2011). In contrast, a rock acquires magnetic remanence when the (cycling) pressure loading is taking place in a magnetic field; such remanence is known as pressure remanent magnetization or piezo-remanent magnetization (Nagata, 1966). The higher the ambient magnetic field, the more remanence is acquired for a given pressure (Nagata & Carleton, 1969). Also, with increasing Ti substitution, the magnetostriction coefficient of magnetite increases (Dunlop & Özdemir, 1997; Gilder & Le Goff, 2008). Thus, the magnetic susceptibility and remanence of titanomagnetite are much more sensitive to the stress regime than stoichiometric magnetite (Dunlop & Özdemir, 1997; Gilder & Le Goff, 2008). Moreover, the effect of pressure on magnetic susceptibility generally decreases with decreasing magnetic grain size; the acquisition of pressure remanent magnetization or demagnetization is quite efficient in large MD grains in comparison to small SD particles (e.g., Gilder et al., 2006; Kean et al., 1976; Volk & Feinberg, 2019).

4.2. Grain Fining of Preexisting Magnetic Particles

A fault core evolves by grain comminution consisting of early bulk fragmentation and late abrasion of grains (e.g., Billi, 2005; Hattori & Yamamoto, 1999; Sammis & Ben-Zion, 2008; Storti et al., 2007), reflecting a progressive reduction in grain size. So, in fault rocks the intensive shearing also may cause widespread splitting of ferromagnetic (sensu lato) grains (if present) into (much) finer material (Figure 3a). Magnetic susceptibility of ferrimagnetic particles depends strongly on grain size when the grains are close to the SP/SSD threshold with SP particles having a distinctly higher magnetic susceptibility than SSD particles

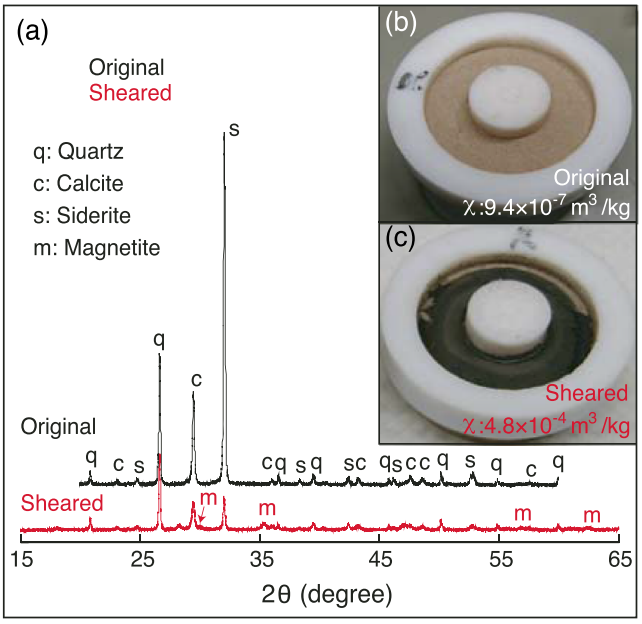

Figure 8. Results of a high-velocity friction experiment on a simulated fault gouge consisting of a 1:1:1 mixture of siderite, quartz, and calcite under a normal stress of 1.3 MPa and at a slip rate of 2.0 m/s conducted by Han et al. (2007). (a) The sheared gouge shows markedly lower X-ray diffraction (XRD) peak intensities in comparison to the original siderite-bearing gouge. The X-ray diffractogram also shows new magnetite peaks on the sheared gouge. The gouge color changes from (b) pale brown before the experiment to (c) black after the experiment, with an increase in magnetic susceptibility (χ) of a few orders magnitude, supporting the XRD interpretation of magnetite.

(e.g., Walden et al., 1999). Thus, magnetic susceptibility may be elevated in fault rocks, even when there is no change in the total concentration of magnetic minerals. Measuring frequency-dependent magnetic susceptibility and low-temperature magnetic measurements are powerful means for estimating the SP particle contribution (e.g., Banerjee et al., 1993; Q. S. Liu et al., 2012). Effects of grain fining as a consequence of shearing can thus be evaluated by these two approaches. The identification of comminuted nanograined magnetic particles is also informative on fracture energetics of fault gouge, as calculation of total grain surface area is a common approach to estimate the fracture energy associated with fault gouge formation (e.g., Aretusini et al., 2017; Chou, Song, Tsao, et al., 2014; Wilson et al., 2005).

4.3. Thermochemical Reactions Induced by Frictional Heating

The transient high temperatures involved in ruptures induce thermochemical reactions within the fault zone (Figure 3a), including decomposition and transformation of Fe-bearing minerals, particularly in the PSZ (e.g., Han et al., 2007; Pei, Zhou, et al., 2014; Tanikawa et al., 2007, 2008; Yang et al., 2018, 2019). Fe-bearing minerals that are widely present in fault zones are siderite ($FeCO_3$), lepidocrocite (γ-FeOOH), goethite (α-FeOOH), pyrite (FeS_2), smectite (Ca, Na, H) (Al, Mg, Fe, Zn)$_2$(Si, Al)$_4$O$_{10}$(OH)$_2$-xH$_2$O) and chlorite ((Mg, Fe, Li)$_6$AlSi$_3$O$_{10}$(OH)$_8$). Most relevant thermal reactions are described below.

1. Siderite's thermal decomposition product is magnetite (Koziol, 2004; Pan et al., 2000) according to:

$$3FeCO_3 + 0.5O_2 \xrightarrow{400\text{–}580^\circ C} Fe_3O_4 + 3CO_2 \quad (9)$$

To illustrate this reaction, high-velocity friction experiments (to simulate seismic slip in the laboratory) on siderite-bearing fault gouge by Han et al. (2007) are insightful: they revealed that siderite was thermally decomposed to nanocrystalline magnetite. This changed the gouge color from pale brown to black and increased the magnetic susceptibility by nearly 3 orders of magnitude (Figure 8). It thus leaves a prominent magnetic imprint of seismic slip in a fault zone, even when siderite is present only in minor amounts (Han et al., 2007; Tanikawa et al., 2008).

2. Lepidocrocite is one of the four iron oxyhydroxides known in nature. It is a paramagnet at ambient temperature and commonly occurs in fault gouges developed from granitic rocks (Fukuchi et al., 2005). On annealing it converts to antiferromagnetic hematite (α-Fe_2O_3) with strongly ferrimagnetic maghemite (γ-Fe_2O_3) as an intermediate phase (Fukuchi, 2003; Gendler et al., 2005). The conversion of lepidocrocite to maghemite (γ-Fe_2O_3) starts at ~200°C, and the thermal dehydroxilation is completed at ~300–350°C, followed by inversion of maghemite to hematite (Gehring & Hofmeister, 1994; Gendler et al., 2005). Maghemite is stabilized by its surface energy, so it is often prominently present as fine particles (T. Chen et al., 2005). Particularly maghemite leaves a magnetic imprint, due to its ferrimagnetic nature.

$$2\gamma - FeOOH \xrightarrow{\sim 200\text{–}350^\circ C} \gamma - Fe_2O_3 + H_2O \rightarrow \gamma - Fe_2O_3 \xrightarrow{> 500^\circ C} \alpha - Fe_2O_3 \quad (10)$$

3. Goethite, another iron oxyhydroxide, thermodynamically the most stable under ambient conditions, also commonly occurs in fault zones. It dehydroxilates to hematite with traces of magnetite or magnetite/hematite aggregates between 240°C and 400°C (Dekkers, 1990; Gualtieri & Venturelli, 1999;

Özdemir & Dunlop, 2000; Yang et al., 2019). The magnetite in particular can be sensed readily by rock magnetic techniques.

$$2\alpha - \mathrm{FeOOH} \xrightarrow{\sim 240\text{–}400^{\circ}\mathrm{C}} \alpha - \mathrm{Fe_2O_3}(+\gamma - \mathrm{Fe_2O_3}/\mathrm{Fe_3O_4}) + \mathrm{H_2O} \quad (11)$$

4. Pyrite is often found as accessory mineral in faults developed within siltstones (e.g., Chou, Song, Aubourg, Song, et al., 2012) and other sediments (e.g., Yang et al., 2018). It decomposes to pyrrhotite (FeS_x, $1 \leq x < 1.08$) as a result of heating to temperatures >500°C under reducing conditions that prevail in the subsurface (Bhargava et al., 2009; Toulmin & Barton, 1964). Pyrrhotite is strongly ferrimagnetic and its occurrence makes a magnetic imprint.

$$\mathrm{FeS_2} \leftrightarrow \mathrm{FeS}_x + (1 - 0.5x)\mathrm{S_2} \quad (12)$$

5. Smectite and chlorite are among the most common constituents of fault gouge. On heating they desorb iron which is precipitated as magnetite. Fine-grained magnetite is produced when heating smectite over 250°C in the laboratory; nucleation and growth of the magnetite grains proceed up to ~450–500°C (Hirt et al., 1993; Yang et al., 2019). Thermochemical reactions of the iron adsorbed to chlorite (particularly chamosite) result in the neoformation of magnetite on heating to 400–700°C (Tanikawa et al., 2008).

Newly formed ferrimagnetic minerals (i.e., magnetite, maghemite, and pyrrhotite) as consequence of the aforementioned thermochemical reactions may increase magnetic susceptibility and magnetization of fault rocks up to a few orders of magnitude (e.g., Han et al., 2007; Mishima et al., 2006, 2009; Tanikawa et al., 2007, 2008; Yang et al., 2012a, 2018, 2019). These newly formed magnetic minerals can be readily diagnosed by the different rock magnetic measurements (or combinations thereof) discussed in section 3. It is necessary to exclude the possibility that the elevated magnetic susceptibility is caused by fining of ferrimagnetic particles before attributing it to the magnetomineralogical changes. However, frictional heating is essentially constrained to the PSZ itself: The temperature rise induced by frictional heating decays exponentially away from the PSZ, as widely reported in modeling results (e.g., Fulton et al., 2013; Yang et al., 2018; Yang, Chen, et al., 2013). Therefore, frictional heating acts prominently only on a very narrow (millimeters to centimeters) zone enclosing the PSZ. Its effects attenuate quickly in other parts of a fault zone, for example, the damage zone.

4.4. Coseismic Frictional Melting With Pseudotachylyte Formation

As mentioned earlier, pseudotachylytes may occur within seismic slip zones (e.g., Ferré et al., 2012, 2017; Hirono, Ikehara, et al., 2006; A. Lin, 2008; A. Lin et al., 2005; Otsuki et al., 2009; Rowe & Griffith, 2015; Sibson & Toy, 2006), due to frictional heating that raises the temperature for a short time above the rock's melting point. The oxygen fugacity in the highly localized melt pockets is generally 2–4 log units above the fayalite-magnetite-quartz buffer (~−11 log units at ~1000°C and 110–160 MPa, e.g., O'Hara & Huggins, 2005). Pseudotachylytes are often more magnetic than their parent rocks, due to the presence of fine-grained PSD/SD ferrimagnetic minerals, predominantly magnetite, that form due to oxidation of mafic silicates during the melting and subsequent quenching (Ferré et al., 2005, 2012, 2017; Ferré, Geissman, et al., 2014; Nakamura et al., 2002; O'Hara, 2001; Pittarello et al., 2012; Zhang et al., 2018). This enables a potentially excellent recording of the NRM in the pseudotachylytes during cooling through the blocking temperature, that is, the NRM is a TRM and should be considered a primary remanence, representing the time of pseudotachylytes cooling, that is, shortly after the rupture itself. In such a context, the paleomagnetic baked contact test and examination of the additivity of partial TRM (e.g., Tauxe, 2010), which reveals the unblocking temperature spectrum and its gradient across a fault zone, would be a means to locate the zones with the highest temperatures in the pseudotachylyte vein zones. Recently, Zhang et al. (2018) found metallic iron in vacuum fusion experiments (in argon) on cataclasites from Borehole No. 2 of the WFSD project. It was formed by the reducing action of Fe-bearing minerals above 1300°C. They proposed that the presence of

metallic iron could be another reason for the magnetic highs of pseudotachylytes. Similarly, studies on high-pressure high-temperature effects in other disciplines, such as impact glasses (e.g., Rochette et al., 2015, 2019), fulgurite (e.g., Essene & Fisher, 1986), shocked Martian meteorites (e.g., Van de Moortèle et al., 2007), have also documented that metallic iron was formed from reduction of more oxidized material. It is hard to identify the metal nanoparticles with conventional mineralogical techniques (e.g., scanning electron microscopy [SEM], Raman spectrometry, and Mössbauer spectroscopy; cf. Van de Moortèle et al., 2007), the presence of metallic iron in natural pseudotachylytes may thus have been overlooked in previous studies.

4.5. Chemical Alteration Due to Fluid Percolation

Fault rocks can be susceptible to disaggregation and dissolution by fluids during the coseismic, postseismic, and interseismic periods (cf. section 2 and Figure 3). The short-duration pulses of hot fluid induced by frictional heating during the seismic slip (Ishikawa et al., 2008; Muir-Wood, 1994) can easily dissolve preexisting Fe-bearing minerals (e.g., pyrite, siderite, and Fe-silicates) whereby Fe^{2+} is liberated (Humbert et al., 2012; Kopp & Humayun, 2003) (Figure 3a). This is followed by precipitation of (among others) ferrimagnetic minerals during the postseismic period because of the low solubility of iron (oxy)(hydr)oxides (Figure 3b). During interseismic periods that last for very long times, fluids, both of meteoric and connate origin infiltrate the fault zone and percolate along a dense microcrack and macrocrack network (Figure 3c). Fluid circulation would lead to destabilization of iron-bearing (clay) minerals in fault zones, with release of Fe^{2+} that dissolves in the fluid and is subsequently transported (Grosz et al., 2006; Hashimoto & Kaji, 2012; Just & Kontny, 2012). The Fe^{2+}-rich fluids thus are potential sources to precipitate magnetic minerals (Pechersky & Genshaft, 2001). Upon reaction with an Fe^{2+}-bearing fluid at temperatures up to 250°C and the most common pH ranges (i.e., pH = ~4.5 at 250°C to ~6.5 at 50°C; Ohmoto, 2003), for example, hematite will transform to magnetite. Magnetite in turn can be transformed to hematite in acidic solutions, with ferrous iron getting into solution (i.e., a so-called nonredox reaction, cf. Ohmoto, 2003):

$$\alpha\text{–}Fe_2O_3 + H_2O(\text{fluid}) + Fe^{2+} \leftrightarrow Fe_3O_4 + 2H^+ \tag{13}$$

Reaction of lepidocrocite with dissolved Fe^{2+} can form magnetite in alkaline media (Cornell & Schwertmann, 2003):

$$2\gamma - \text{FeOOH} + Fe^{2+} \rightarrow Fe_3O_4 + 2H^+ \tag{14}$$

Similarly, the breakdown of pyrite produces goethite or hematite depending on temperature and pH. High temperature and low pH generally favor hematite over goethite (Cornell & Schwertmann, 2003): at low temperature and high pH (slightly alkaline conditions)

$$4FeS_2 + 15O_2 + 10H_2O\ (\text{fluid}) \rightarrow 4\ \alpha - \text{FeOOH} + 8H_2SO_4 \tag{15}$$

or at high temperature and low pH (moderately acidic conditions)

$$4FeS_2 + 15O_2 + 8H_2O\ (\text{fluid}) \rightarrow 2\ \alpha - Fe_2O_3 + 8H_2SO_4 \tag{16}$$

Magnetic properties of fault zones thus change drastically on (partial) removal of preexisting magnetic minerals and/or formation of new (magnetic) minerals (e.g., Chou, Song, Aubourg, Song, et al., 2012; Yang, Chen, et al., 2013; Yang, Yang, et al., 2016). However, the migration paths and composition of fault fluids may vary enormously over time and space, as fault zones act as fluid-flow conduits or barriers at different stages in their development (Goddard & Evans, 1995). This leads to temporal and spatial changes in redox state of a fault zone as function of episodic fault rupture and healing cycles during the lifetime of the fault (Yamaguchi et al., 2011). Thus, precipitation products of fluid circulation (e.g., iron oxides, iron hydroxides, and/or sulfides) are highly dependent not only on the physical and chemical conditions (permeability, temperature, pressure, redox and pH, etc.) and chemical composition of the fluids but also on the fluid/rock ratio and the lithology of the fault zones (Chou, Song, Aubourg, Song, et al., 2012; Grosz et al., 2006; Guichet et al., 2006; Yang, Chen, et al., 2013; Yang, Yang, et al., 2016).

4.6. EQL-Induced IRM Acquisition

EQL currents have been reported on several occasions during large earthquakes (e.g., Fidani, 2010; Heraud & Lira, 2011; Kamogawa et al., 2005; J. Y. Liu et al., 2015; St-Laurent et al., 2006; Thériault et al., 2014). However, the underlying formation mechanism is still controversial. A flurry of mechanisms have been put forward to explain the charge generation in the subsurface during earthquake motion: piezomagnetism, piezoelectricity, electrokinetic flow processes, opening of the tips of cracks, stress-activation of positive holes, and hydromechanical rupture (Enomoto et al., 2017; Freund et al., 2007; Losseva & Nemchinov, 2005; St-Laurent et al., 2006). Regardless of its formation mechanism, the coseismic electric current is expected to travel along the fault plane, which often acts as a good electrical conductor with a conductivity of up to 4 orders higher than the surrounding insulating host rocks (Ferré et al., 2005). According to the Biot-Savart law, a transient strong azimuthal magnetic field will be produced perpendicular to the fault plane (Ferré et al., 2005, 2012; Losseva & Nemchinov, 2005). In this arrangement—lamellar conductive rocks enveloped by insulating margins—fault gouge, pseudotachylite generation veins, parallel or near parallel to the fault plane, will readily acquire an IRM. This IRM is a secondary NRM termed "earthquake lightning-induced remanent magnetization (EQLIRM)" (Enomoto et al., 2001; Enomoto & Zheng, 1998; Ferré et al., 2005, 2012). EQLIRM is distinct from lightning NRM in rocks struck by surface lighting; in the latter the lightning IRM remagnetization pattern is circular (either clockwise or counterclockwise) centered on the lightning-bolt impact location, coupled with a decrease in magnetization intensity away from the electric bolt (e.g., Losseva & Nemchinov, 2005; Verrier & Rochette, 2002). In the context of EQLIRM fault rocks, several paleointensity tests (e.g., Ferré, Geissman, et al., 2014; Gattacceca & Rochette, 2004) and normalization of the NRM intensity by M_s are helpful to discriminate high NRM caused by a strong ambient magnetic field from that caused by high concentrations of magnetic minerals. If the latter can be excluded, the high NRM then may be attributed to a strong magnetic field induced by seismically generated electrical currents.

4.7. Secondary NRM Acquisition Due to Physicochemical Processes in Fault Zones

The EQLIRM dealt with in the previous section is a rather special case. In general, neoformed magnetic minerals (resulting from any thermochemical reaction and/or fluid-rock interaction) may carry a chemical remanent magnetization (CRM). Also, the mere cooling of a slip zone (hot coseismic fluids included) would lead to an imprint of a (partial) TRM in a fault zone (Figure 9). These newly imprinted NRM components in and near the slip zone are oriented parallel to the contemporaneous local geomagnetic field (Chou, Song, Aubourg, Lee, et al., 2012). Evidently, a NRM direction will be different in a fault zone when the (latest or most intense) rupture occurred any time later than the formation of the original rocks. The fault gouge can retain the magnetic record during interseismic periods. However, these newly imprinted NRM components may be (partially) overprinted again during later seismic events (Figure 9; see also Chou, Song, Aubourg, Lee, et al., 2012).

Often, several of the aforementioned mechanisms act simultaneously; it is necessary to find support for individual mechanisms and/or their acting in concert to better understand the magnetic changes within a fault zone. For instance, the removal or decrease in concentration of certain magnetic mineral(s), and grain fining of magnetic particles that might be induced by the faulting, can readily be evaluated by concentration-dependent magnetic properties and grain-size-dependent properties, respectively. This is a foremost asset of rock magnetic techniques.

5. Magnetic Properties and Faulting Processes

5.1. Indicator of Seismic Slip Records

Proper slip zone identification is crucial to understand earthquake generation processes and paleoseismology (e.g., Rowe & Griffith, 2015). Estimating earthquake recurrence rates requires proper identification of slip zones that accommodated historic earthquake events. Also, the most intense slip conditions may be revealed. These are fundamental ingredients for seismic risk assessment. However, to find robust evidence of seismic slip is not straightforward from a practical point of view. It is to be expected that the aforementioned faulting-related magnetic changes should leave a trace in the rock record, thus making magnetic property analysis a potential indicator of seismic slip.

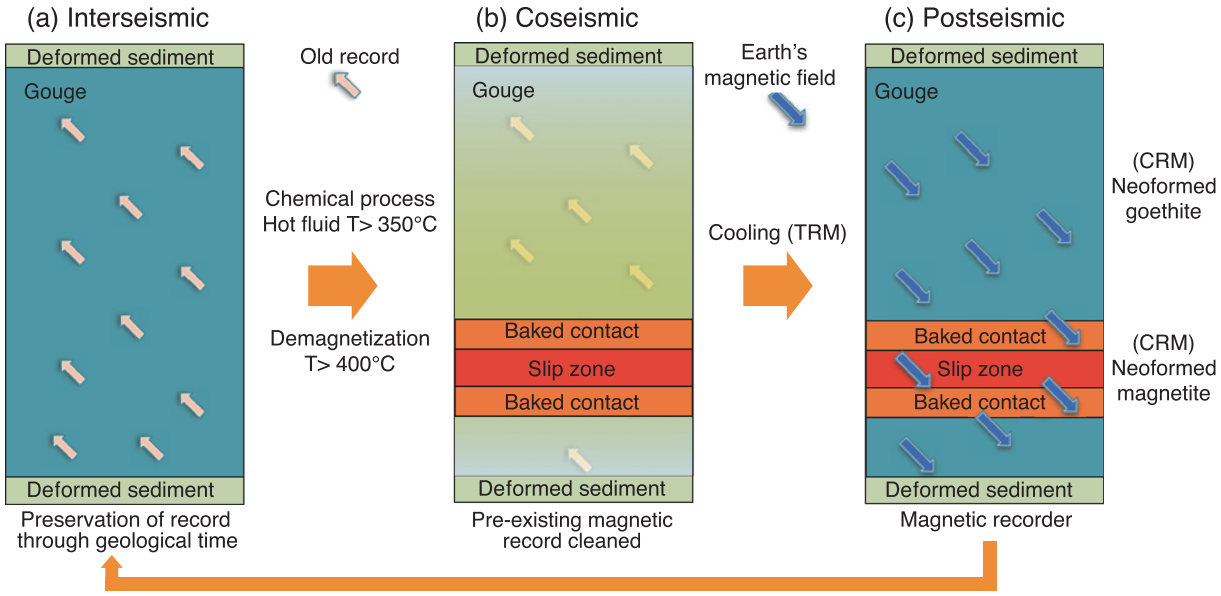

Figure 9. A conceptual model showing the magnetic recording cycle in fault gouge of the Fault Zone FZB1136, TCDP Hole-B, which accommodated the Taiwan 1999 Chi-Chi earthquake (reprinted from Chou, Song, Aubourg, Song, et al., 2012). (a) During an interseismic period, in the fault gouge the magnetic record of the last earthquake is preserved through geological time. (b) During a coseismic period, the elevated temperature and chemical degradation lead to a partial-to-complete demagnetization of the preexisting magnetic record in the slip zone and the "baked contact" zone. (c) During the subsequent postseismic period, cooling of the slip zone and/or hot coseismic fluids leads to an imprint of TRM, while the neoformed magnetic minerals resulting from any form of chemical process may carry a CRM. The newly imprinted (T)CRM component(s) thus leave(s) a magnetic record of the recent earthquake event.

5.1.1. Magnetic Locating of Pseudotachylyte Veins

Classically, pseudotachylytes have been considered as the only definitive evidence of ancient seismic activity (Cowan, 1999; Rowe & Griffith, 2015). They are well known as "earthquake fossils" and less prone to natural alteration on geological timescales (A. Lin, 2008). A strong NRM is often observed in pseudotachylyte veins due to the presence of abundant PSD/SD magnetite (Figure 10; Ferré et al., 2005). This makes (paleo)magnetic measurements a robust way to locate pseudotachylyte veins, providing further linkage to past seismic events, such as the kinematic solution (see section 5.4.1 for details). In addition, it is believed that magnetic properties of pseudotachylytes are controlled by oxygen fugacity and thus vary systematically with depth of formation (Ferré et al., 2012, 2017; Ferré, Geissman, et al., 2014; O'Hara & Huggins, 2005). Pseudotachylytes that formed at shallower depths (<10–12 km) commonly exhibit coseismically formed maghemite or hematite (e.g., Fukuchi, 2003; Petrik et al., 2003), while those formed at intermediate crustal depths (~20 km) are generally dominated by magnetite (e.g., Davidson et al., 2003; Ferré, Geissman, et al., 2014; Nakamura & Nagahama, 2001). In contrast, pseudotachylytes formed at even greater depths tend to be ilmenite-dominated (e.g., Ferré, Geissman, et al., 2014; Moecher & Steltenpohl, 2009). Therefore, rock magnetic properties are informative on the ambient conditions of the earthquake rupture (Ferré et al., 2017; Ferré, Geissman, et al., 2014).

5.1.2. Coseismic/Postseismic Neoformed Magnetic Minerals

Coseismic and/or postseismic neoformed magnetic minerals along with their related anomalies in magnetic properties have also been widely reported during the recent "rapid response" fault zone drilling campaigns after major earthquakes. These include the Taiwan Chelungpu Fault Drilling Project (TCDP) following the 1999 Chi-Chi earthquake (e.g., Hirono, Lin, et al., 2006; Kano et al., 2006), the WFSD drillings following the 2008 Wenchuan earthquake (e.g., H. Li et al., 2015; Pei, Li, et al., 2014; Wang et al., 2014; Zhang et al., 2017), and the Japan Trench Fast Drilling Project (JFAST) following the 2011 Tohoku-oki earthquake (e.g., Brodsky et al., 2020; Fulton et al., 2013; W. Lin et al., 2013; Yang et al., 2018). In TCDP Hole-B, the Fault Zone FZB1136, the PSZ of the 1999 Chi-Chi earthquake was estimated to contain up to ~200 ppmv magnetite from the magnetic susceptibility and saturation IRM peaks (Figure 11; Chou, Song, Aubourg, Song, et al., 2012; Chou, Song, Aubourg, et al., 2014). One should bear in mind that the parameters used here (i.e., magnetic susceptibility and saturation IRM) are dependent on both magnetic particle size and concentration of magnetic minerals (e.g., Dunlop & Özdemir, 1997; Peters & Dekkers, 2003; Walden et al., 1999;

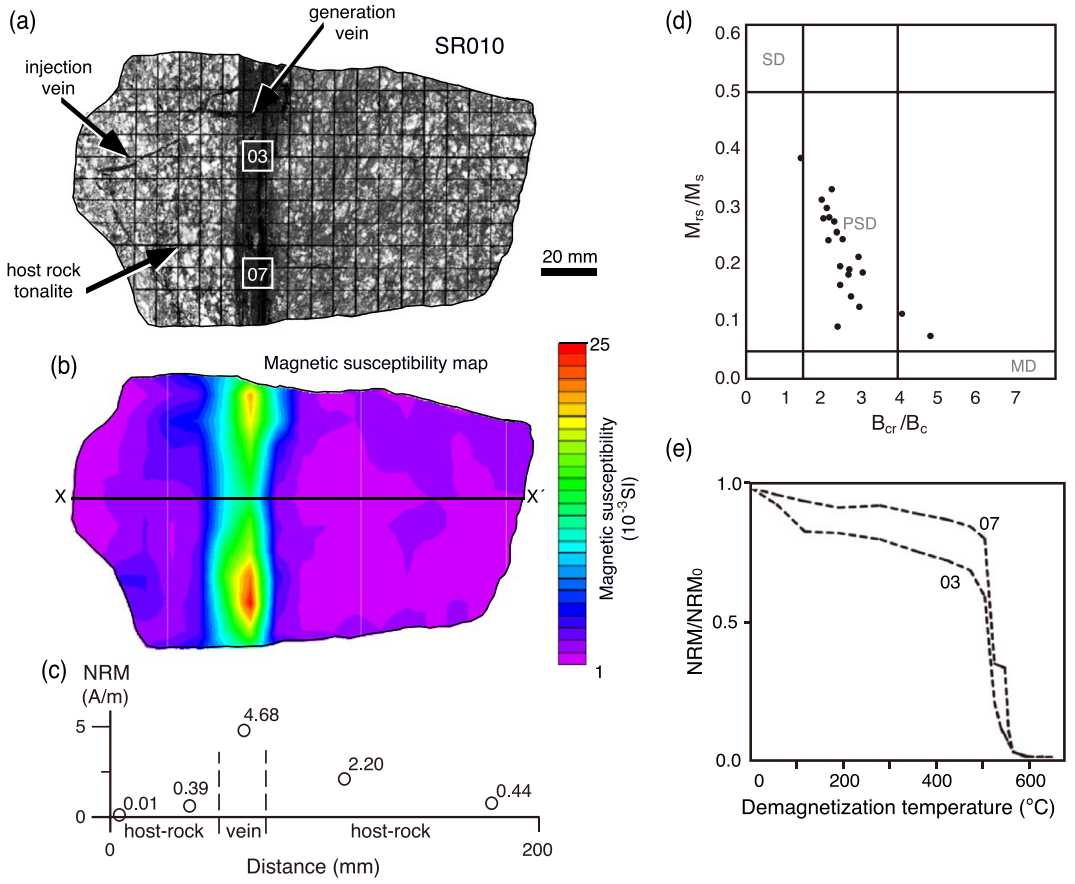

Figure 10. (a) Image of a slab sample across a generation pseudotachylyte vein from the Santa Rosa Mountains, California and (b) the spatial variation in the magnetic susceptibility of the slab. The map was produced by interpolation over a grid of 170 susceptibility measurements performed with a Bartington MS-2F probe with a sensitivity of 2×10^{-6} SI. Each 10 mm a data point was collected. (c) NRM intensity along the X-X′ profile in Figure 10b. (d) Hysteresis properties of pseudotachylyte veins plotted on a Day plot. Most specimens display hysteresis behavior consistent with PSD grains. (e) NRM thermal decay curves of the two samples (Nos. 03 and 07) obtained from the pseudotachylyte veins (Figure 10a), indicating low-Ti magnetite as the principal remanence carrier. Figures 10a–10d and Figure 10e are reproduced from Ferré et al. (2005) and Ferré, Geissman, et al. (2014), respectively.

see also section 3). Therefore, one has to take into account that estimates of magnetic mineral concentrations based on these two parameters yield a range of possible concentrations rather than a single value (evidently with an uncertainty envelope). In contrast, usage of saturation magnetization (M_s) to this end leads to a single number for the magnetic mineral concentrations in a given fault rock sample because M_s is only proportional to the concentration of magnetic minerals in a sample. In Hole WFSD-1, magnetic susceptibility peaks occur at the fault zone FZ590 which was inferred to have accommodated the 2008 Wenchuan earthquake. The peaks were credited to newly formed magnetite due to the thermal decomposition of Fe-bearing clays (e.g., smectite and chlorite) by frictional heating during seismic slip (Pei, Li, et al., 2014; Yang et al., 2012a). In the JFAST drill hole, partial thermal alteration of pyrite to pyrrhotite was exclusively identified in three slip zones developed in the frontal prism sediments (Yang et al., 2018). The reactions were induced by seismic frictional heating and related coseismic hot fluids (Figure 12), thus intimately associated with earthquake events (Yang et al., 2018). Examination of the magnetic mineral assemblage in fault zones may therefore be a prospective way for identifying the most recent PSZ (Cai et al., 2019; Chou, Song, Aubourg, et al., 2014; Chou, Song, Aubourg, Song, et al., 2012; Yang et al., 2012a, 2018, 2019).

5.1.3. Seismically Imprinted NRM Components

As mentioned in section 4.7, newly imprinted NRM component(s), that is, TRM and/or CRM, may also leave a (paleo)magnetic record of recent seismic slip. For instance, in the aforementioned slip zone TCDP

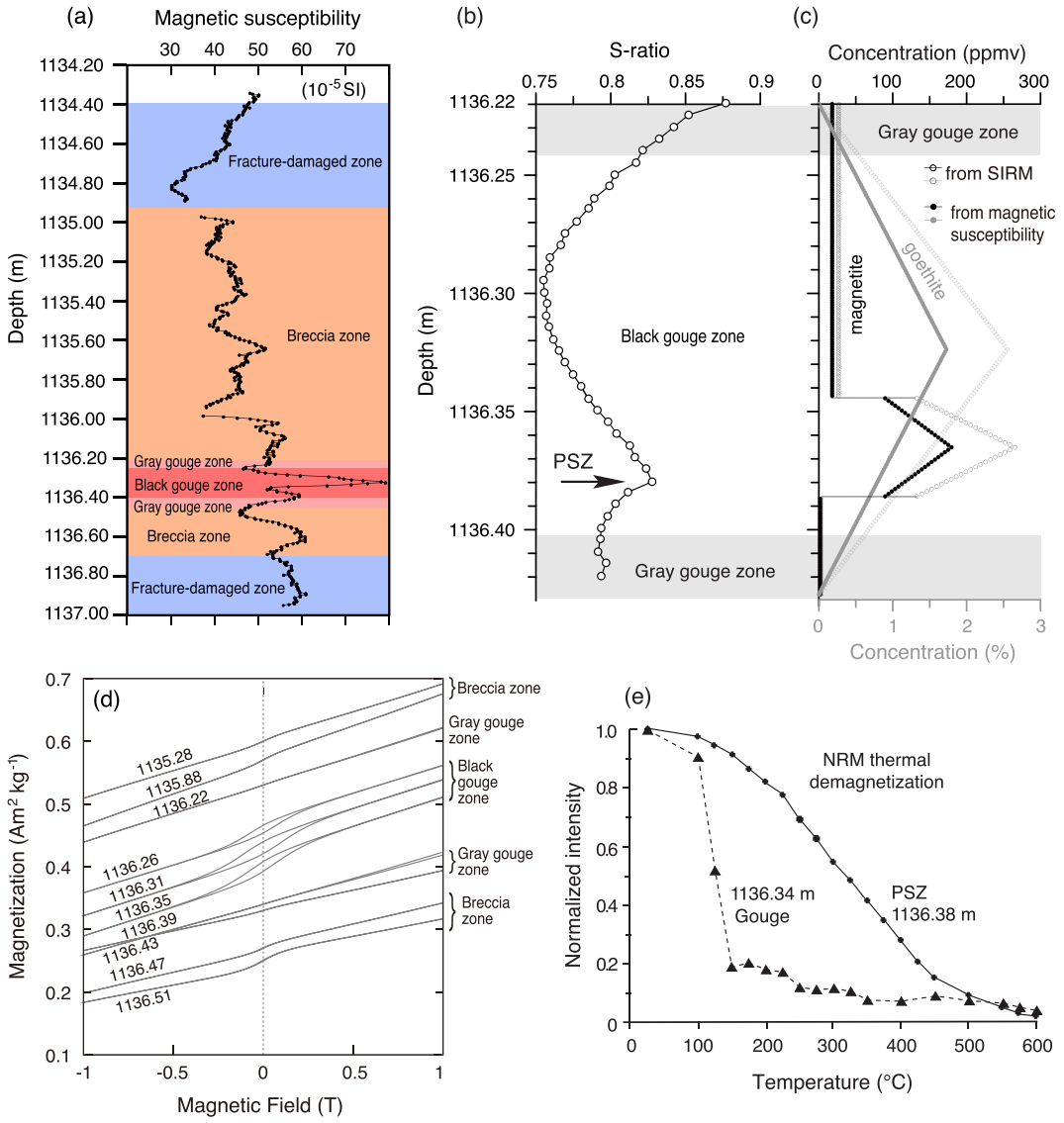

Figure 11. Magnetic susceptibility (a), S-ratio (b), and estimated concentration profiles of magnetite and goethite (c) in the Fault Zone FZB1136, TCDP Hole-B (Taiwan). The PSZ is characterized by a peak in the magnetic susceptibility (a) and the S-ratio (b), which is consistent with a large amount of magnetite (c). The concentrations of magnetite and goethite are estimated from the magnetic susceptibility and SIRM of the core samples using a quantitative model (for details on the modeling strategy, see Chou, Song, Aubourg, et al., 2014). The lowest value of the S-ratio is located near the center of the fault gouge, corresponding to the highest concentration in goethite (c). (d) Magnetic hysteresis loops and (e) NRM thermal decay curves for selected samples from the Fault Zone FZB1136. Within the gouge (e.g., the sample at 1136.34 m), the principal maximum unblocking temperature (T_b) of ~120°C is consistent with the Néel temperature of goethite, while in the PSZ (e.g., sample at 1136.38 m), the maximum T_b is close to 580°C, indicating the presence of magnetite as main magnetic carrier. The latter concurs with the open hysteresis loops saturated below 0.3 T in Figure 11d. These observations suggest that the magnetic susceptibility anomaly at the Fault Zone FZB1136 (Figure 11a) is attributed to the formation of magnetite, as a result of the thermal decomposition (>400°C) of paramagnetic minerals (e.g., pyrite, siderite, and chlorite) during the 1999 Chi-Chi earthquake. Figures 11a and 11d are adapted from Hirono et al. (2007) and Mishima et al. (2009), respectively; Figure 11e is compiled from Chou, Song, Aubourg, Song, et al. (2012); data in Figures 11b and 11c are from Chou, Song, Aubourg, Song, et al. (2012) and Chou, Song, Aubourg, et al. (2014), respectively.

FZB1136, a stable single NRM component with a direction very close to the present-day Earth's field was identified within an ~16 cm thick fault gouge zone (Figure 13; Chou, Song, Aubourg, Lee, et al., 2012). It is therefore inferred to be the coseismic paleomagnetic record of the recent 1999 Chi-Chi earthquake (Chou, Song, Aubourg, Lee, et al., 2012). In contrast, NRM records of two other slip zones (i.e., FZB1194

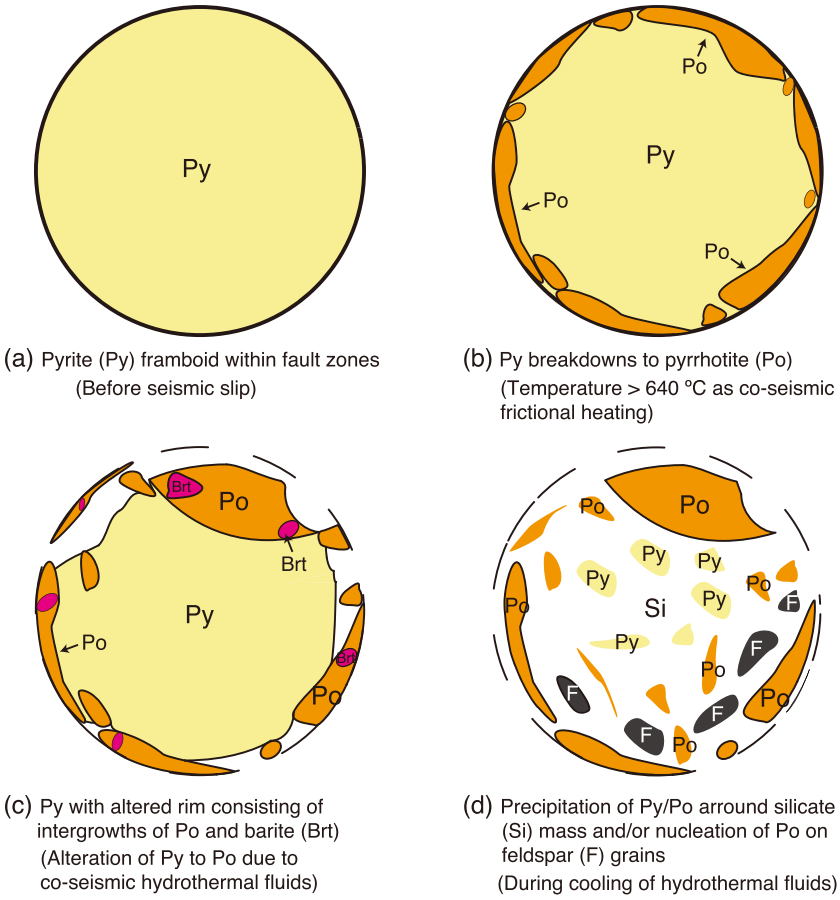

Figure 12. A cartoon showing the thermal alteration of preexisting pyrite with neoformation of pyrrhotite as a result of seismic frictional heating and subsequent coseismic hydrothermal fluids in a pyrite-bearing fault zone during an earthquake (reprinted from Yang et al., 2018). During the seismic slip, (a) pyrite in the slip zone thermally decomposes to pyrrhotite once the temperature is over ~640°C and (b) a pyrrhotite rim surrounding the pyrite core is formed indicating an incomplete reaction. (c) Leaching by coseismic hot fluids, pyrite is altered and an intergrown rim of pyrrhotite and barite is formed. (d) Precipitation of pyrite/pyrrhotite around the silicates and/or nucleation of pyrrhotite on feldspar grains occurs at expense of iron and sulfur released by destabilization of pyrite and other minerals in fault zone, during cooling of the coseismic hot fluids. The reader is referred to Yang et al. (2018) for more details.

and FZB1243) show directions far away from the present-day field that were probably acquired before the Brunhes-Matuyama reversal (0.78 Ma). They thus have recorded ancient earthquake events and were not reactivated during the 1999 Chi-Chi earthquake; otherwise, these slip zones would have been overprinted, at least partially (Chou, Song, Aubourg, Lee, et al., 2012).

5.1.4. Earthquake-Induced AMS Fabric

AMS analysis of clastic dikes (see Appendix A for definition) has also successfully identified the unique magnetic fabrics of dikes emplaced by injection due to seismically triggered fluidization. In the Dead Sea Basin (Israel), one of the most active tectonic areas in the Middle East, for instance, host sediments appear to be characterized by oblate AMS ellipsoids with vertical axes of the minimum magnetic susceptibility (κ_{min}) that indicate a normal sedimentary magnetic fabric, whereas the liquefied sediments are characterized by triaxial fabrics with subvertical κ_{int} axes and subhorizontal κ_{max} axes parallel to the dike strike (Levi et al., 2006a). Similar AMS fabrics have been reported by Jayangondaperumal et al. (2010) in the Himalayan frontal thrust (in the western Himalaya), by Lakshmi et al. (2017) in the Dauki fault (Shillong Plateau, India), and by Cho et al. (2017) in the Dadaepo Basin (SE Korea). These contrasting magnetic fabrics have provided crucial evidence for seismically triggered fluidization of clastic materials. Furthermore, Levi et al. (2018) recently proposed a plot of the magnetic lineation versus the shape parameter of the AMS ellipsoid to distinguish different seismites formed in soft sediments, that is, damage zones, gouges, earthquake-triggered folds,

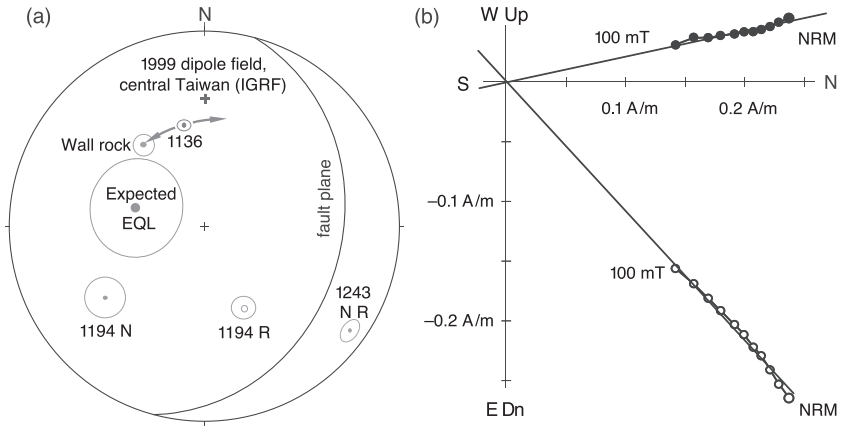

Figure 13. NRM record in the TCDP fault gouge that hosts the principal slip zone of the 1999 Chi-Chi earthquake (Taiwan) (reproduced from Chou, Song, Aubourg, Lee, et al., 2012). (a) Equal-area stereoplot showing the Chelungpu fault plane, the mean paleomagnetic components recorded in the three fault zones (FZB1136, FZB1194, and FZB1243) and the wall rock of the TCDP Hole-B, and the expected orientation of the earthquake lightning (EQL) NRM, with an error of ±20° in declination. Solid and open symbols indicate the downward and upward hemispheres, respectively. The wall rock's main component lies away from the modern magnetic field, which is indicated as the 1999 international geomagnetic reference field (IGRF) model magnetic vector in central Taiwan by a bold plus symbol (+). The FZB1136 fault gouge component is closest to the modern magnetic field and statistically different from the hypothetical EQL direction. In the FZB1194 and FZB1243 gouges, both normal and reversed components are oriented southerly. (b) Orthogonal plot of AF demagnetization of the NRM in FZB1136 gouge (depth of 1,136.33 m). Open and solid circles represent projection of the vector on the vertical and horizontal planes, respectively.

and breccia layers. It enabled categorizing seismites that underwent different deformation processes into distinct groups in the above-mentioned Dead Sea fault system (cf. Figure 4 in Levi et al., 2018). This illustrates that AMS can be also used as a potential petrofabric tool for recovering paleoseismic records in soft sediments (Levi et al., 2006a, 2006b, 2014, 2018).

5.2. Thermal History of Seismic Slip

Estimation of the temperature rise induced by frictional heating during an earthquake provides crucial information on faulting weakening mechanisms (e.g., frictional melting, thermal decomposition of carbonates, and thermal pressurization), the prevailing dynamic shear stress, slip velocity, and displacement (e.g., Di Toro et al., 2009; Scholz, 2019; Sibson, 1977; Yao et al., 2016). At the same time, earthquake energy budgets as a whole can be assessed (e.g., Scholz, 2019). Here, temperature information derived from melt thermodynamics from experimental igneous petrology data, and pyrometamorphism in principle could be very useful. The approach is widely used to quantitatively determine melting and crystallization temperatures (e.g., Berman et al., 1995; Ghiorso & Gualda, 2015; Palmer et al., 2015). However, the minerals (e.g., olivine, clinopyroxene, biotite, and garnet) typically used as "temperature proxy" are often not occurring in fault rocks, in particular in fault gouges. This unfortunately complicates a straightforward application to fault zone problems.

Thermal anomalies associated with seismic slip have been traced during the recent rapid postearthquake fault drilling projects after major earthquakes, such as the TCDP, the WFSD, and the JFAST projects (respectively, Fulton et al., 2013; Kano et al., 2006; H. Li et al., 2015). In contrast to expectation, only very weak bulk temperature anomalies (<0.5°C) were identified across these fault zones. The thermal anomalies also appear to be much lower than predicted from the fault strength deduced from the in situ stress measurements and laboratory rock friction data (e.g., Brodsky et al., 2020; Fulton et al., 2013; Tanaka et al., 2006; Ujiie et al., 2013). The temperature within a slip zone is locally elevated by coseismic frictional heating to quite variable maximum temperatures, even at shallow crustal levels. This is surmised from widely reported thermochemical reactions: clay mineral reactions (e.g., Brantut et al., 2008; L.-W. Kuo et al., 2011), decarbonation reactions (e.g., Han et al., 2007; Rowe, Fagereng, et al., 2012), amorphization (Aretusini et al., 2019; Rowe et al., 2019), trace element partitioning features (e.g., Ishikawa et al., 2008; Tanikawa et al., 2015), graphitization of carbonaceous material (e.g., Kuo et al., 2014; Oohashi et al., 2011), thermal maturation of

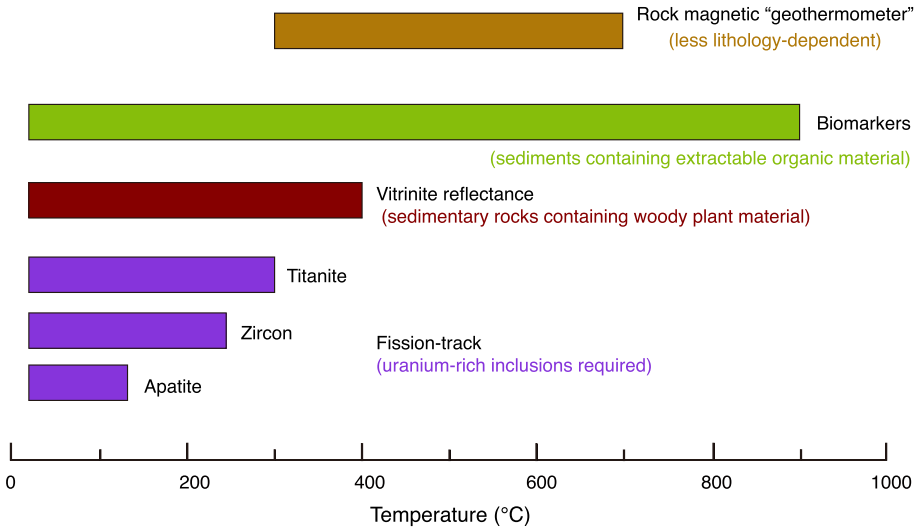

Figure 14. Comparison of the proposed provisional rock magnetic "geothermometer" (Yang, Dekkers, & Zhang, 2016) with other, more conventional, seismic frictional heating thermometers, including vitrinite reflectance, fission-track, and biomarkers. The text next to each approach refers to the conditions where the respective thermometers can be applied. The bar widths indicate their working temperature ranges. The reader is referred to the main text and Yang, Dekkers, and Zhang (2016) for more details.

organic molecules (e.g., Coffey et al., 2019; Rabinowitz et al., 2017; Savage et al., 2014), fission track signatures (e.g., D'Alessio et al., 2003), vitrinite reflectance anomalies (e.g., Maekawa et al., 2014; Sakaguchi et al., 2011), and occasionally the occurrence of pseudotachylytes (e.g., Otsuki et al., 2009; Zhang et al., 2017). These diagnostic features provide important constraints on the temperatures in the PSZ that prevailed during previous earthquake events. However, each of these approaches requires fairly specific conditions to be applicable. For example, vitrinite reflectance and biomarkers can only be applied to sediments that contain certain types of organic matter, and fission tracks require the presence of uranium-rich inclusions in certain minerals. Also, most approaches only provide information on a certain temperature threshold or a fairly narrow range in temperature. Vitrinite reflectance, for instance, indicates temperatures <400°C (Mukhopadhyay, 1992); higher temperatures cannot be diagnosed. Fission tracks indicate ~120–300°C because they are developed in that temperature window (Figure 14, also see Yang, Dekkers, & Zhang, 2016, for more details). Thus, to achieve a complete picture of frictional heating, yet other approaches are desired, complementary to existing methods.

Here, magnetic properties can be used at our advantage. Neoformation of ferrimagnetic minerals through thermochemical reactions of Fe-bearing minerals induced by frictional heating is deemed widespread in seismic fault zones (see section 4.3). This opens up a new perspective in estimating the temperature experienced during seismic slip (e.g., Chou, Song, Aubourg, Song, et al., 2012; Fukuchi et al., 2005, 2007; Han et al., 2007; Hirono et al., 2009; D. Liu et al., 2016; Mishima et al., 2006; Tanikawa et al., 2007, 2008; Yang et al., 2019, 2018; Yang, Dekkers, & Zhang, 2016). For example, a strong magnetic susceptibility anomaly in fault gouge was observed at the Fault Zone FZB1136, in TCDP Hole-B (Figure 11a). It has been attributed to the formation of large amounts of magnetite (Figures 11c–11f): paramagnetic minerals (e.g., pyrite, siderite, and chlorite) decomposed at high temperatures (>400°C) during the Chi-Chi earthquake (Chou, Song, Aubourg, et al., 2014; Mishima et al., 2006, 2009). Pyrrhotite was also identified within the FZB1136 gouge as suggested by FORC diagrams (Figure 15): this provides evidence for thermal decomposition of pyrite at temperatures >500°C (Chou, Song, Aubourg, Song, et al., 2012). The aforementioned occurrence of pyrrhotite in slip zones in the Japan Trench frontal prism sediments constrains the peak temperature of seismic frictional heating to between 640°C and 800°C, combining magnetic information with microscopy observations and pyrite-to-pyrrhotite reaction kinetics (Yang et al., 2018). These results provide crucial temperature constraints for understanding the earthquake energy dissipation and weakening mechanisms, as frictional heating is regarded as the foremost factor controlling fault weakening (e.g., Bizzarri, 2009; Yao et al., 2016).

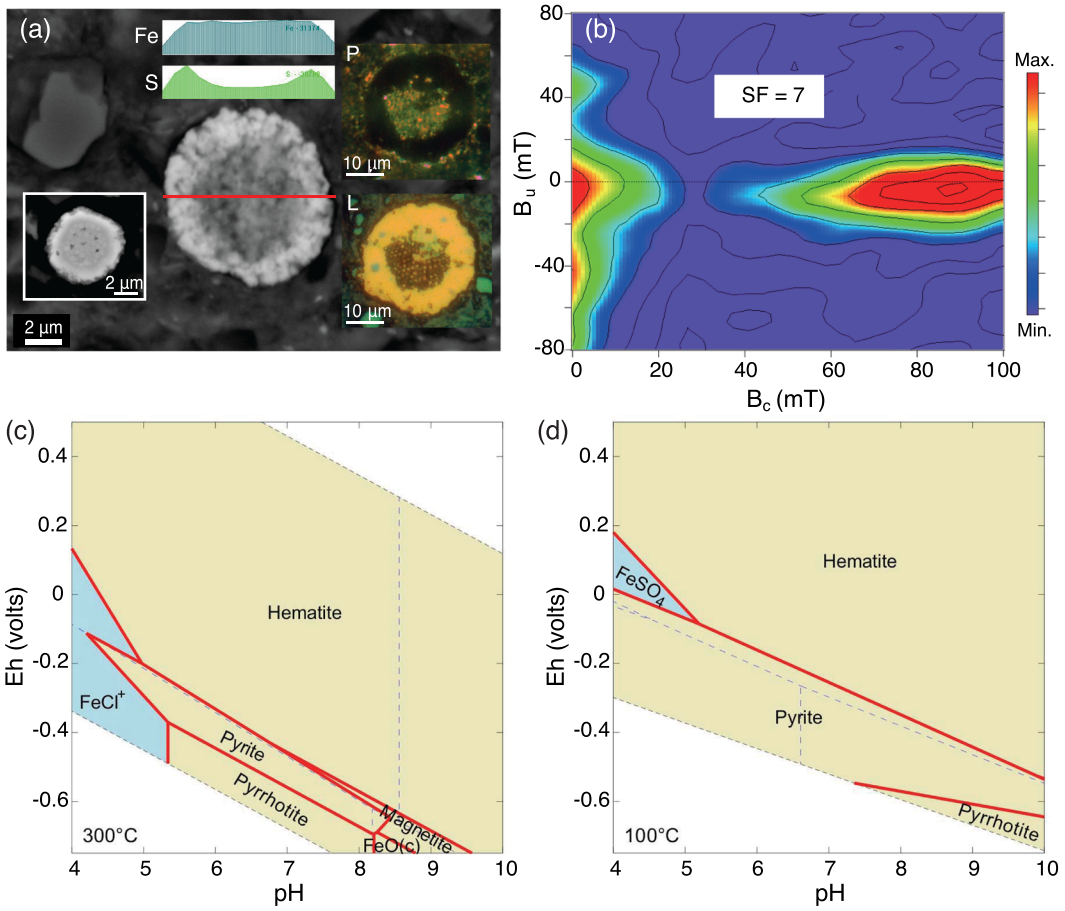

Figure 15. (a) Backscatter SEM images of a pyrrhotite-pyrite grain in the FZB1136 gouge in TCDP Hole-B, Taiwan. The framboidal pyrrhotite core has a 1–10 μm pyrite rim. With crossed polars under reflected light microscopy the pyrrhotite core remains bright and the isotropic pyrite rim is black (insets) (P: cross-polarized reflected light image; L: reflected light image with plane polars). Pyrrhotite is inferred to have formed from high-temperature decomposition of pyrite (>500°C) during coseismic slip of repeated earthquakes, while pyrite resulted from retrograde metamorphism of pyrrhotite during cooling of coseismic fluids. (b) FORC diagram for the FZB1136 gouge. A coercivity peak at 90 mT reveals the presence of magnetically interacting pyrrhotite. (c and d) Modeled Eh-pH diagrams showing the stability of pyrite and pyrrhotite at fluid temperatures of 300°C and 100°C inferred for the fault gouge zone of FZB1136 in TCDP Hole-B. The pyrite stability field at lower Eh values increases with decreasing temperature from 300°C to 100°C, whereas that of pyrrhotite field shrinks to a small range with high pH values (8–10) at 100°C, suggesting that pyrite formed as a result of retrograde alteration of pyrrhotite. The presence of pyrite rims on pyrrhotite cores in the framboids (Figure 15a) supports this retrograde interpretation. Compiled from Chou, Song, Aubourg, Song, et al. (2012).

Recently, a preliminary rock magnetic fault zone "geothermometer" was developed, which is utilizing magnetic susceptibility versus temperature measurements during cycling in the laboratory to increasingly elevated temperatures (Yang, Dekkers, & Zhang, 2016). The thermochemical expression of magnetic phases in a rock should not change unless the rock is heated in the laboratory beyond the maximum temperature it underwent in nature (e.g., Hrouda et al., 2003; Spassov & Hus, 2006). This approach is very similar to estimating temperatures of ancient fires and burnt structures in archeology (Jordanova et al., 2018). In the Japan Trench subduction plate boundary décollement, cored by the JFAST project, maximum temperatures were determined ranging from ~300°C to over 500°C close to the multiple slip surfaces of previous earthquakes (cf. Figure 6b in Yang, Dekkers, & Zhang, 2016). The rock magnetic geothermometer of fault rocks is less dependent on lithology requirements. Moreover, it offers resolution in the 300–700°C temperature range, which is difficult to assess with other geothermometers (Figure 14). It thus is a promising complementary approach for assessing temperature anomalies in slip zones.

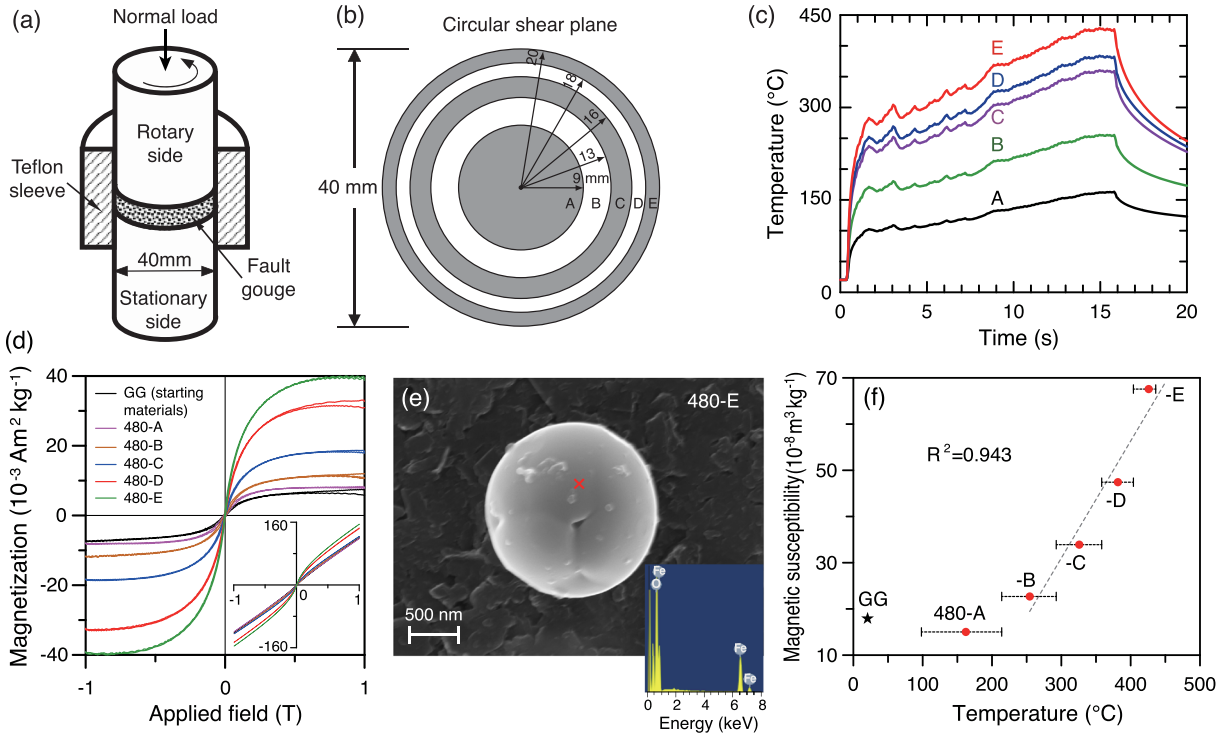

Figure 16. Rock magnetic properties of experimentally sheared natural fault gouge with a high-velocity apparatus (compiled from Yang et al., 2019). (a) A schematic diagram of the rotary shear high-velocity friction (HVF) testing machine. (b) Sampling strategy after the HVF experiment. The sheared plane is divided into five annuluses with equivalent slip velocities during the experiments. The slip rate and displacement are 0 at the center and reach maximum values at the edge. (c) Modeled temperature due to frictional heating in the different annuluses as a function of slip time. The reader is referred to Yang et al. (2019) for more details on the equations and modeling strategy. (d) Hysteresis loops after and before (insets) correction for the paramagnetic contribution of the starting material and run products after the experiments. The starting material is dominated by paramagnetic Fe-bearing minerals; run products contain an increasing amount of magnetite with slip distance. (e) SEM picture of an Fe oxide spherule with some adhered smaller particles present in the outermost annulus of the sheared gouge. Inset is EDS spectrum for the analyzed spot marked by the red cross. (f) Magnetic susceptibility of run products linearly increases with the estimated peak temperatures experienced during the experiment, suggesting enhancement of the newly formed magnetite with increasing temperature due to frictional heating. GG indicates the starting material; red dots mark the run products. R^2 is the coefficient of determination of the line fits.

Substantial magnetic enhancement is also observed experimentally in high-velocity friction experiments on natural fault gouges with increasing slip distance (e.g., Fukuchi et al., 2005; Tanikawa et al., 2007; Yang et al., 2019). Magnetite, occurring as spherical and sintered irregular aggregates (Figure 16), was formed during friction experiments on fault gouges from the Yingxiu-Beichuan fault. The original gouges are essentially paramagnetic with one gouge containing minor goethite (~4 wt%); magnetite is the result of thermochemical reactions of iron adsorbed on clay minerals (smectite and chlorite) and/or alteration/reduction of goethite. Higher frictional heating temperatures (equivalent to longer slip distances) led to higher values of magnetic susceptibility and magnetization and to larger grain sizes of the newly formed magnetite as indicated by decreasing coercivity (Yang et al., 2019). Changes in magnetic parameters appear to be linear with the (calculated) temperature rise induced by frictional heating (Figure 16f). Therefore, magnetic properties of fault rocks can be used not only to detect seismic frictional heating but also to evaluate the amount of frictional work associated with seismic slip (Tanikawa et al., 2007, 2008; Yang et al., 2019). Clearly, further experimental work is required to establish a (semi)quantitative relation between magnetic parameters and the heat production rate (and thus temperature rise) due to sliding. Only then meaningful extrapolation to natural conditions would be allowed.

However, as discussed in section 4.5, fluid infiltration is widely present in a fault zone. During the postseismic and long-term interseismic periods, fluids of either meteoric or deep origin (or a combination) may infiltrate into and percolate through the fault zone. Therefore, the latest coseismically imprinted magnetic records (i.e., the aforementioned newly formed ferrimagnetic minerals, and consequent high magnetic susceptibility and magnetization) could be erased or overprinted soon after the earthquake. It is reported that

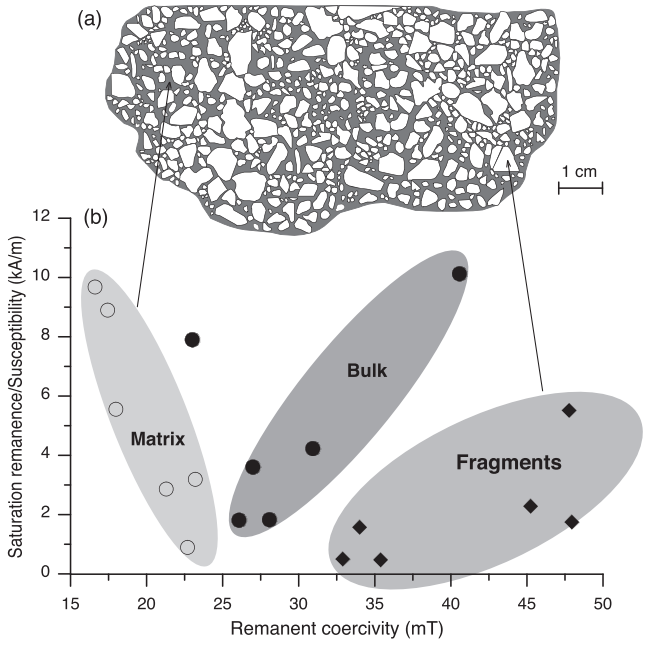

Figure 17. (a) Sketch of a typical cemented fault breccia from the rupture zone of the 2008 Wenchuan earthquake (Sichuan Province, China). The fault breccia is characterized by the formation of host rock derived fragments embedded within a finer-grained matrix. (b) A plot of remanent coercivity (B_{cr}) versus the ratio of the saturation remanence and magnetic susceptibility (M_{rs}/χ) shows that the matrix, fragments of the fault breccias, and bulk samples fall into three groups, suggesting the presence of different magnetic carriers in the two components (fragments and matrix) of fault breccias (adapted from Yang, Chen, et al., 2013).

fault properties can be measurably changed 2 years after an earthquake (Brodsky et al., 2009), and the fluid infiltration would be one of the most important factors driving these changes (Yang, Yang, et al., 2016). Thus, there would be a rare opportunity to gain crucial information by observing such transient magnetic changes related to a specific rupture only immediately after a large earthquake (typically within a couple of years).

5.3. Fingerprint of Fluid Infiltration in Fault Zones

Fluid flow, a major actor in fault zones, is intimately linked to the nucleation, propagation, arrest, and recurrence of earthquake ruptures (e.g., J. Chen et al., 2017; J. P. Evans & Chester, 1995; Goddard & Evans, 1995; Hickman et al., 1995; Kerrich et al., 1980; Miller, 2013; Rice, 2006; Terakawa et al., 2010; Williams et al., 2017; Zoback et al., 2007). Detailed characterization of neoformed and/or altered magnetic minerals due to fluid-rock interaction, as discussed in section 4.5 is thus important for understanding the fluid-related processes.

In the 16 cm thick gouge of the Fault Zone FZB1136 in TCDP Hole-B drilled into the Chelungpu fault in Taiwan, the presence of goethite was demonstrated by thermal demagnetization of NRM (Figure 11e), measurements of the room temperature SIRM acquired in 2.5 T during cycling between 300 and 400 K, and transmission X-ray microscopy (Chou, Song, Aubourg, Lee, et al., 2012; Chou, Song, Aubourg, Song, et al., 2012). Its maximum concentration was estimated to be ~1% from the magnetic susceptibility and SIRM values of the gouge (Figure 11c). The goethite is argued to have been formed during cooling of a hot coseismic fluid (>350°C) shortly after the 1999 Chi-Chi earthquake (Chou, Song, Aubourg, Lee, et al., 2012; Chou, Song, Aubourg, Song, et al., 2012). The coseismic fluids were richer in iron in the center of the gouge zone than at the edges, as demonstrated by the pattern of modeled goethite concentration across the gouge (Figure 11c; see Chou, Song, Aubourg, et al., 2014, for detailed modeling strategy). On cooling of hot fluids after the earthquake, Eh-pH conditions are inferred to have changed (Chou, Song, Aubourg, Song, et al., 2012, Figures 15c and 15d), which led—next to the formation of goethite—to partial oxidation of magnetite, and some retrograde alteration of pyrrhotite to pyrite (Figure 15a).

Also in the rupture zone of the 2008 Wenchuan earthquake, a marked contrast in magnetic properties was identified for the two components in the fault breccia, fragments, and matrix. The matrix has a relatively higher magnetic susceptibility and magnetization but a lower coercivity than the fragments (Figure 17). The contrast was attributed to fault fluids that caused selective dissolution and precipitation of Fe-bearing minerals in the fault breccias during previous earthquake cycles. The matrix is more prone to fluid-related effects than the fragments due to its finer grain size and thus larger specific surface (Yang, Chen, et al., 2013). Magnetite concentrations were found to decrease starting with the host rock, via fault breccia, to (proto)cataclasite. In addition, both low- and high-field magnetic susceptibility show close relationships with chlorite that is a hydrothermal alteration product, as well as with the immobile elements (e.g., TiO_2 and P_2O_5; cf. Figures 13 and 14 in Yang, Yang, et al., 2016). Since those elements are essentially immobile during fluid-rock interaction processes, they can be used to infer the losses of mobile elements by mechanical wear and dissolution, for example, by evaluating patterns in ratios of immobile to mobile elements. Finally, low- and high-field magnetic susceptibility are also positively correlated with the mass losses of fault rocks estimated with the isocon method of geochemical mass balance (e.g., Tanaka et al., 2001). These observations suggest that magnetite depletion and precipitation of Fe-bearing clay minerals occurred in these fault rocks—exhumed from the shallow crust—plumbed by fluid-assisted processes (Figure 18; see Yang, Yang, et al., 2016, for details). Hence, magnetic properties of fault rocks represent an expression of fluid infiltration within fault zones. Further work is necessary to establish a possible causal link between the specifics of magnetic minerals and the fault fluid properties (e.g., chemistry, temperature, and pressure).

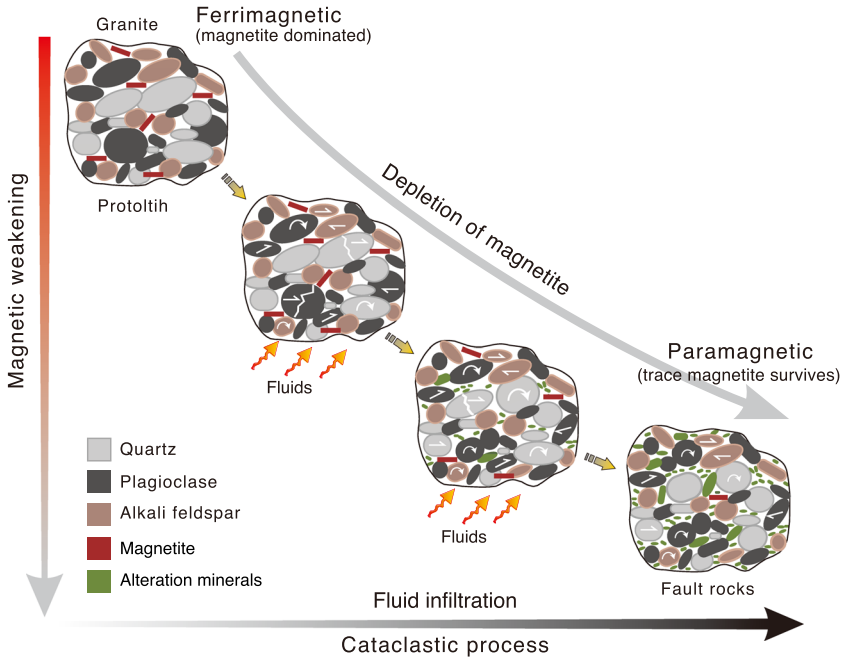

Figure 18. A simple conceptual model illustrating the fluid-assisted cataclastic process (reprinted from Yang, Yang, et al., 2016). Cataclasis transforms a granite protolith with magnetite as the dominant magnetic carrier to essentially paramagnetic fault rocks, that is, cataclasite, fault breccia, and gouge, in the Yingxiu-Beichuan fault (Longmen Shan thrust belt, China), which accommodated most of the displacement of the 2008 *Mw* 7.9 Wenchuan earthquake (for details the reader is referred to Yang, Yang, et al., 2016).

5.4. AMS and Strain Geometry in Fault Zones

Based on exchange equilibria, various mineral assemblages (e.g., phengite, sphalerite, hornblende, and clinopyroxene) have been used as "geobarometer" to define differential stress conditions in crustal rocks (see Reverdatto et al., 2019, for a review). However, these "stress proxy" minerals are usually absent in fault zones. This is also the case for more conventional strain markers (e.g., fossils, ooids, pebbles, and nodules) (Hayman et al., 2004). This makes it difficult to quantify the stress/strain conditions and deformation fabrics in fault zones. Magnetic fabric analysis, validated for various rock types and in different structural settings (e.g., Borradaile & Henry, 1997; Hrouda, 1982; Martín-Hernández et al., 2004; Parés, 2015; Tarling & Hrouda, 1993), is a widely used tool to examine deformation in geologic structures characterized by large strain gradients such as shear zones (for a review, see Ferré, Gébelin, et al., 2014). However, to date only a few studies have targeted brittle fault rocks in the shallow crust (e.g., Casas-Sainz et al., 2018; Chou, Song, Lee, et al., 2014; Louis et al., 2008; Marcén et al., 2019; Nakamura & Nagahama, 2001; Román-Berdiel et al., 2019; Solum & van der Pluijm, 2009; Yeh et al., 2007). In contrast to the ductile mylonitic rocks, brittle fault rocks are typified by frictional sliding as dominant deformation process (e.g., Schmid & Handy, 1991; Sibson, 1977; see section 2 for details). This involves grain rotation, fracturing, and translation of (magnetic) minerals in fault rocks. The shear effects are reflected in magnetic fabric changes and provide clues on the strain states in fault zones, as outlined below.

5.4.1. Kinematics of Fault Slip

The orientation of the magnetic fabric provides constraints on the kinematics of fault slip (e.g., Casas-Sainz et al., 2018; Elhanati et al., 2020; Ferré et al., 2015, 2016; Hayman et al., 2004; Levi et al., 2014; Marcén et al., 2019; Solum & van der Pluijm, 2009). In the seismically active Dead Sea Basin (Israel), for example, the original depositional fabric, characterized by a subvertical κ_{min} axis and scattered κ_{max} and κ_{int} axes, is well preserved ~2 m away from the fault plane. In contrast, the principal AMS axes of the deformation-driven fabrics, which could be observed up to tens of cm from the fault plane, are coaxial with the instantaneous strain ellipsoids calculated with the fault plane solutions (Figure 19). Such magnetic fabrics are interpreted to result from the local strain field during the past earthquakes (Levi et al., 2014). Another illustrative example is the study of fault rocks from the Chelungpu fault (Taiwan). AMS fabrics

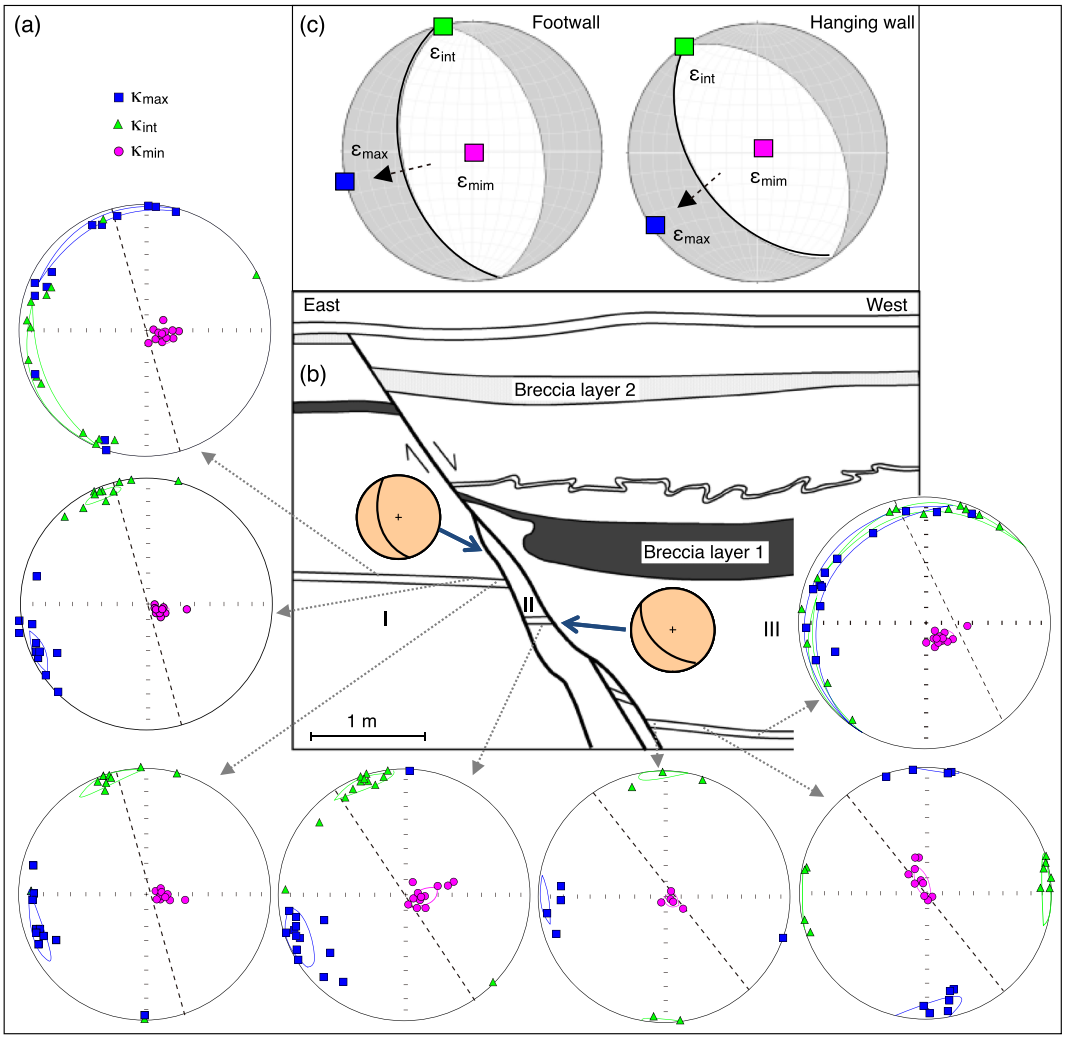

Figure 19. Comparison of magnetic fabrics and fault plane solutions across a normal fault in the Lisan Formation, Masada Plain (Israel), in the Dead Sea basin, where numerous $M > 6$ earthquake events occurred during the last 70,000 years (compiled from Levi et al., 2014). (a) Lower hemisphere equal-area projections of principal AMS axes of the late Pleistocene soft rocks in the footwall (I), intermediate block (II), and hanging wall (III). Dashed lines indicate the strike direction of the nearby fault strands. The two small stereograms in Figure 19b show the orientations of the fault strands. (c) Two fault planes and moment-tensor solutions calculated for the footwall and hanging wall. Dashed arrows mark the dip-slip direction. ε_{max}, ε_{int}, and ε_{min} are the instantaneous maximum, intermediate, and least principal strain axes, respectively. The principal AMS axes of soft rocks close to the three late Pleistocene syndepositional normal faults resemble the fault plane solutions.

revealed that the compressional stress orientation is identical to the regional stress regime and that the magnetic foliation planes of fault gouges are consistent with thrust dip-slip displacement across the gouge zones (Yeh et al., 2007). Also recently, Ferré et al. (2015) reported for the first time a successful determination of the full kinematic solution (slip plane, direction, and sense) of a prehistoric (20.1 ± 0.5 Ma) seismic event through AMS analysis of pseudotachylyte veins in the Dora Maira Massif (Italy; Figure 20). The analysis relies on the notion that AMS of fault pseudotachylytes arises from coseismic viscous flow of the frictional melt and therefore is tracking the direction of slip (Ferré et al., 2015). These studies demonstrate that magnetic fabrics can be employed not only to detect the local strain field but also to determine fault plane solutions of previous earthquakes.

5.4.2. Strain State Across Fault Zones

Stress and strain information across a fault zone are crucial ingredients for our understanding of earthquake generation and related slip behavior. Rocks that host (future) faults, in particular unlithified and

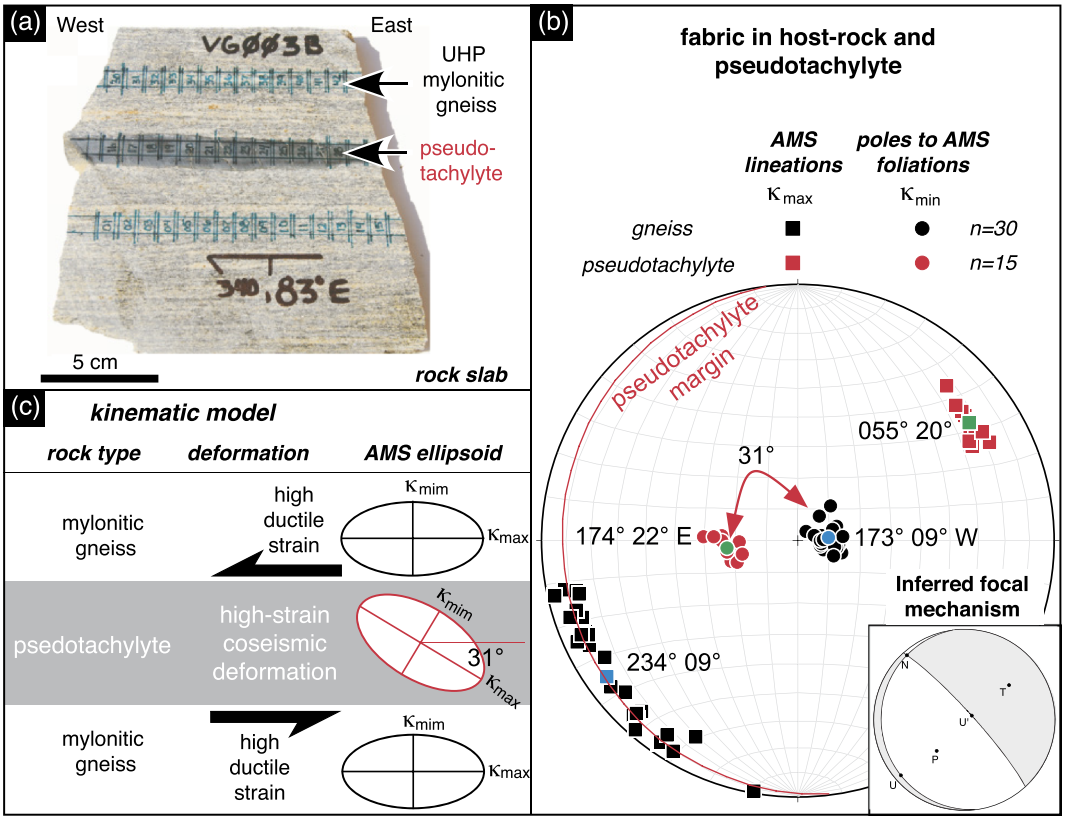

Figure 20. Focal mechanism of a prehistoric earthquake deduced from magnetic fabrics of pseudotachylyte veins (the Dora Maira massif, western Italian Alps) (compiled from Ferré et al., 2015). (a) Macroscopic view of the pseudotachylyte generation vein developed in the host mylonitic gneiss. (b) Comparison of magnetic fabrics of the host gneiss (in black) and pseudotachylyte (in red). The host gneiss (with corrected degree of magnetic anisotropy P_j of 1.38 ± 0.10) has a subhorizontal magnetic foliation and magnetic lineation. In contrast, the pseudotachylyte foliation (with P_j of 1.08 ± 0.01) has an angle of 31° with that of the host gneiss. It is formed as a result of rapid cooling of the melt and recorded viscous flow parallel to the seismic slip direction (c), and thus revealing a top-to-west sense of shear and a normal fault focal mechanism.

unconsolidated sediments, respond to the progressive tectonic loading by the development of a preferred orientation of the constituent (magnetic) minerals. This fabric is commonly coaxial with the axes of the strain ellipsoid; more specifically, the pole to the magnetic foliation is widely regarded as the orientation of the maximum shortening strain (e.g., Cifelli et al., 2004; Parés, 2015). Therefore, comparison of the magnetic fabrics in host rocks bounding the fault zone and fault rocks sheds light on how the strain state varies across the fault zone. For example, AMS analysis revealed an abrupt change in strain state across the plate boundary fault zone (décollement) at shallow depths near the Japan Trench (Yang, Mishima, et al., 2013): The AMS data of the prism sediments above the décollement depict the maximum strain direction of lateral shortening due to the WNW convergence of the Pacific plate, while those of the underthrust sediments appear to point to a classic sedimentary compaction fabric, thus a vertical, uniaxial strain (Figure 21). The plate boundary décollement between the Pacific and North American plates is thus decoupled over the long term, which favors the propagation of coseismic slip along it (Yang, Mishima, et al., 2013). Such strain decoupling across a décollement zone revealed by AMS fabrics was also reported at the Nankai Trough (Owens, 1993; Ujiie et al., 2003), the Costa Rica margin (Housen & Kanamatsu, 2003), the Barbados accretionary margin (Hounslow, 1990; Housen, Tobin, et al., 1996), and the Chile Triple Junction region (Collombat et al., 1995). AMS is thus an excellent indicator for incremental strain that sensitively reflects the stress state across a fault zone.

5.4.3. Deformation Mechanism of Fault Zones in the Shallow Crust

Fault breccia and cataclasite are considered to have been deformed via cataclastic flow (Hayman et al., 2004). It is a specific deformation mechanism that involves continuous brittle fracturing and comminution

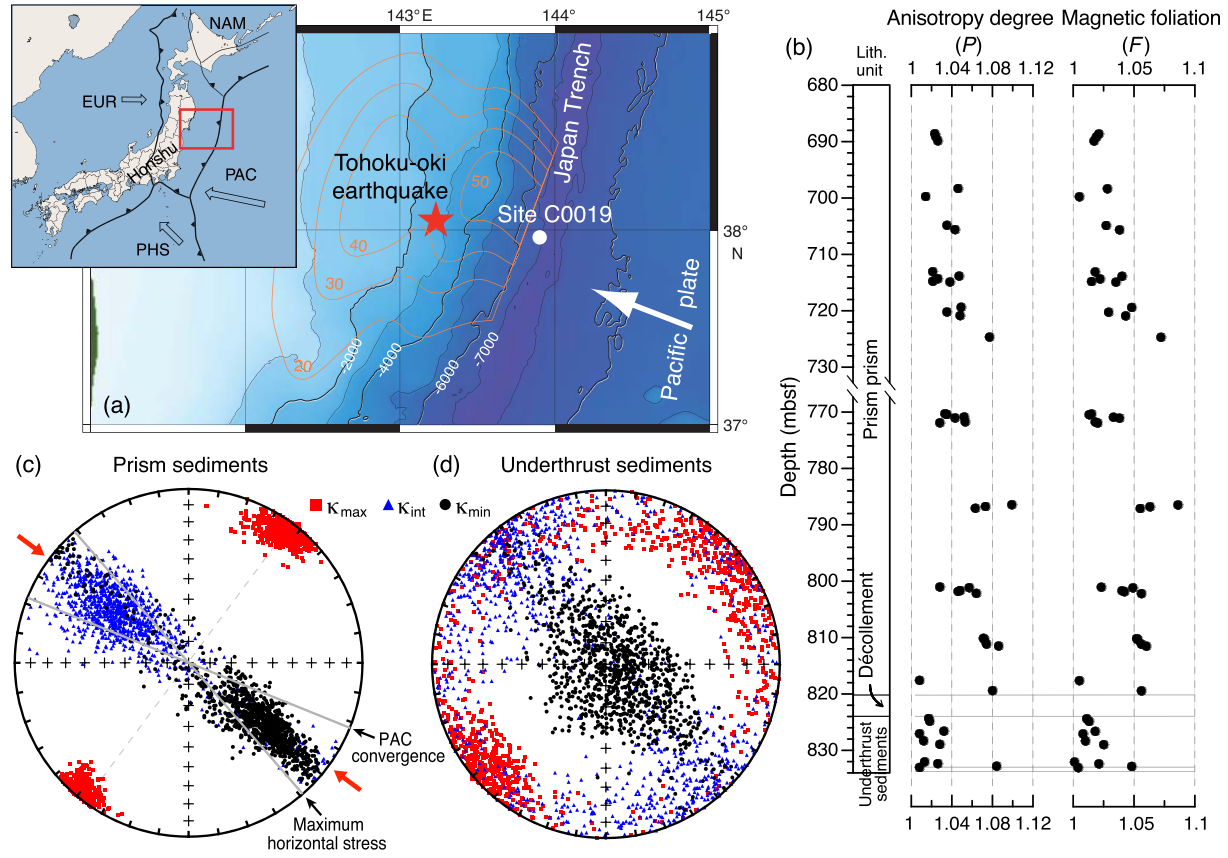

Figure 21. (a) The general plate configuration of the Japanese island arc and map of the 2011 *Mw* 9.0 Tohoku-oki earthquake portion of the Japan Trench, showing the location of the IODP Expedition 343 drill site with a filled white circle. The red star indicates the epicenter of the earthquake. White arrow indicates the Pacific plate (PAC) convergence vector with a rate of~85 mm/year (Argus et al., 2011). (b) Downcore profiles of degree of anisotropy (*P*) and magnetic foliation (*F*). Both progressively increase with depth in the frontal prism and suddenly drop just below the décollement, mostly showing small values in the underthrust sediments. Equal-area, lower hemisphere projections of the bootstrapped κ_{max}, κ_{int}, and κ_{min} directions for (c) the prism sediments ($n = 34$) and (d) the underthrust sediments ($n = 22$). The AMS fabric pattern of the prism sediments is consistent with horizontal tectonic shortening (red arrows in Figure 21c) nearly parallel to the PAC convergence direction in the Japan Trench, as well as the maximum horizontal stress deduced from borehole breakouts (W. Lin et al., 2013). The AMS in the underthrust sediments represents a vertical, uniaxial strain, that is, an initial sedimentary compaction fabric. These very different AMS patterns reveal an abrupt strain change across the plate boundary décollement at shallow depths and imply that large coseismic slip occurred along a weak décollement that is mainly decoupled over the long term. Compiled from Yang, Mishima, et al. (2013) with data from Argus et al. (2011) and W. Lin et al. (2013).

of grains with frictional sliding and rolling of the fragments with respect to one another (Twiss & Moores, 1992). Magnetic grain size reduction occurring during cataclastic flow is expected to decrease the grain-scale anisotropy of the AMS carriers (Ferré, Gébelin, et al., 2014; Jackson et al., 1993). This may explain why notably weak and even nearly isotropic AMS tensors were determined in strongly fractured granites in the Nojima Fault in Japan (Nakamura & Nagahama, 2001). In contrast, fault gouges are inferred to be the product of granular flow (Twiss & Moores, 1992) which involves the rolling and sliding of rigid particles (Morgan, 1999; Morgan & Boettcher, 1999). In this process, the physical rearrangement of the magnetic minerals primarily results in an increase in the AMS parameters (e.g., *P* and *F*). One should bear in mind, however, that brittle fault rocks often host secondary minerals that not necessarily relate directly to strain. For example, in the Fault Zone FZB1136 in TCDP Hole-B the magnetic foliation and anisotropy degree are lowest in the PSZ itself, whereas the highest values appear in the fault gouge where goethite is present (Chou, Song, Lee, et al., 2014). The goethite was formed postseismically by the action of thermal fluids (Chou, Song, Aubourg, Song, et al., 2012, see also section 5.3). Therefore, caution is appropriate when interpreting the deformation mechanisms based on the AMS analysis of brittle fault rocks (e.g., Román-Berdiel et al., 2019). Microscopic inspection of whether or not secondary minerals are present is recommended.

The magnetic fabric of pseudotachylytes is providing a snapshot of the ambient stress during or immediately after seismic slip (e.g., Ferré et al., 2015, 2016; Molina-Garza et al., 2009). In the Chiapas Massif (Mexico), for example, the magnetic fabrics of the host granitoid rock and the pseudotachylyte veins are essentially parallel, with nearly east-west and steep magnetic foliations. However, the AMS fabric of the host rock is dominantly prolate, while that of the pseudotachylytes veins is markedly oblate. This suggests that the veins underwent a pure shear deformation (i.e., viscous breaking) during cooling (Molina-Garza et al., 2009), again illustrating that AMS analysis delivers important insights into the deformation mechanism of fault zones.

5.5. Magnetic Records of Coseismic Electric Currents

As mentioned earlier, several faulting-related magnetization processes contribute to the NRM acquisition of pseudotachylytes, including coseismic TRM acquired upon cooling of the melt below the Curie temperature, EQL-induced IRM acquisition (EQLIRM), and postseismic CRM due to both devitrification and alteration (Ferré et al., 2012; Leibovitz, 2016). Deciphering these magnetization components is crucial to the understanding the pseudotachylytes' microstructures and the timing of their development.

Coseismic TRM is restricted to the local melt pockets and records the direction and intensity of the geomagnetic field at the time of cooling. It is straightforwardly demagnetized thermally in the laboratory. In contrast, EQLIRM typically displays an anomalously high NRM value in pseudotachylytes with characteristic directions at a high angle to the fault plane. There is no geometric relationship to the past or present directions of the geomagnetic field (Leibovitz, 2016). Thus, rock magnetic and paleomagnetic analyses of the pseudotachylytes do provide independent constraints on the origin(s) of the NRM in pseudotachylytes. Anomalously high NRM recorded in a pseudotachylyte, which would require a magnetic field (much) stronger than the typical Earth's magnetic field, then points to EQLIRM as the dominant NRM acquisition process.

Indeed, such abnormally high NRM intensities have been reported for fault rocks (fault gouge and pseudotachylytes) along or near the fault plane where large earthquakes occurred (e.g., Enomoto & Zheng, 1998; Enomoto et al., 2001; Ferré et al., 2005, 2012; Ferré, Geissman, et al., 2014). For instance, pseudotachylyte with an abnormally high NRM (~132 A/m), up to 300 times higher than that of the granitic host rock (tonalite), was found in the Santa Rosa Mountains near Palm Springs, California, USA (Ferré et al., 2005). These pseudotachylyte veins typically have a moderate-coercivity, well-defined, single component NRM isolated with stepwise progressive alternating field demagnetization (cf. Figure 6a in Ferré et al., 2005). For comparison, typical NRM values of volcanic rocks that cool in the Earth's magnetic field range from 0.1 to 10 A/m depending on their chemical composition. Mafic and ultramafic rocks are more magnetic than felsic rocks. To acquire the reported high NRM, the fault rocks and pseudotachylytes must have been exposed to a strong local magnetic field, several orders of magnitude higher than the typical Earth's main field (Ferré et al., 2005). The most likely source of the required strong magnetic field is believed to be the coseismic electric currents produced by EQL (Ferré et al., 2005). In the Nojima Fault (Japan), the coseismic electric current was estimated to be as high as ~1 kA during the 1995 Kobe earthquake through simulation of the EQL-induced sintering of the fault gouge using spark plasma sintering experiments (Enomoto et al., 2001). Such a large current is expected to produce a strong pulsed magnetic field, in which the foliated fault gouges acquired an IRM which resulted in a very large NRM: ~430 times higher than that of the granitic fault breccia, and ~70 times higher than that of the adjacent mudstone (Enomoto et al., 2001; Enomoto & Zheng, 1998).

6. Comparison of Magnetic Methods to Other Approaches

The magnetic properties of fault rocks can provide intriguing insights into faulting processes. The number of magnetic studies on fault rocks, however, is rather limited to date. A broad-scale comparison of fault rock magnetic data with other more classical approaches is therefore currently in its infancy. Below we assemble the information concerning the temperature of frictional heating and the stress/strain state of the fault retrieved from magnetic and nonmagnetic thermal and strain indicators. This comparison is only possible in a few fault zones that accommodated large earthquakes, where data from multiple techniques are available.

Table 1
Comparison of Peak Temperatures of Frictional Heating Estimated by Magnetic and Nonmagnetic Approaches in Three Fault Zones That Accommodated Large Magnitude Earthquakes

Peak temperatures	Indicators/methods	Note
TCDP Hole B Fault Zone FZ1136; hosted the 1999 Chi-Chi (Taiwan) earthquake (Mw 7.6)		
>400°C	Thermal decomposition of paramagnetic minerals[a,b,c,d]	Magnetic indicators
>500°C	Pyrrhotite formation via thermal breakdown of pyrite[e]	
>350°C	Fluid-mobile trace element anomalies[f]	Nonmagnetic indicators/methods
>300–400°C	Vaporization of water during thermal pressurization[g]	
626 ± 25°C	Vitrinite reflectance[h]	
~ ≥ 700°C	Infrared and Raman spectra of carbonaceous materials[i]	
900–1100°C	Clay mineral anomalies (FZ1111 in Hole A that corresponds to FZ1136 Hole B)[j]	
~1200°C	Thermal decomposition or breakdown of siderite into nanosized grains[k]	
0.06°C residual temperature anomaly 6 years after the earthquake	Direct borehole observation[l]	
Japan Trench subduction plate boundary fault zone; hosted the 2011 Mw 9.0 Tohoku-oki earthquake		
>300–500°C	Rock magnetic "geothermometer"[m]	Magnetic indicators
640–800°C	Reaction of pyrite to pyrrhotite[n]	
120–900°C	Organic biomarker thermal maturity[o]	Nonmagnetic indicators/methods
0.31°C residual temperature anomaly 16 months after the earthquake	Direct borehole observation[p]	
<1250°C	Modeled with plausible slip durations and slip zone thicknesses, and a friction coefficient of 0.08[p]	
Nankai Subduction Zone (Japan) associated with the 1944 Tonankai Mw 8.1 earthquake		
<400°C	No thermal decomposition of paramagnetic minerals occurred[q]	Magnetic indicators
<300°C	Fluid-mobile trace elements, Raman spectra of carbonaceous material, and inorganic carbon content[q]	Nonmagnetic indicators/methods
390 ± 50°C	Vitrinite reflectance[r]	
<250°C	Infrared spectroscopy, clay mineral anomalies, trace-element geochemistry, and isotope geochemistry[s]	

[a]Mishima et al. (2006). [b]Mishima et al. (2009). [c]Tanikawa et al. (2007). [d]Tanikawa et al. (2008). [e]Chou, Song, Aubourg, Song, et al. (2012). [f]Ishikawa et al. (2008). [g]Boullier et al. (2009). [h]Maekawa et al. (2014). [i]Hirono et al. (2015). [j]L.-W. Kuo et al. (2011). [k]W.-H. Li et al. (2019). [l]Kano et al. (2006). [m]Yang, Dekkers, and Zhang (2016). [n]Yang et al. (2018). [o]Rabinowitz et al. (2020). [p]Fulton et al. (2013). [q]Hirono et al. (2009). [r]Sakaguchi et al. (2011). [s]Hirono et al. (2014).

6.1. The Seismic Frictional Heating Temperature

Frictional heating during seismic slip is evidently registered in all minerals in the slip zone, not only in magnetic minerals. Nonmagnetic minerals include hydrous, clay, and carbonate minerals. Thus, frictional heating might be traced and cross calibrated by a variety of thermal indicators (Table 1). In the Fault Zone FZ1136, TCDP Hole-B, the peak temperature during the 1999 Chi-Chi earthquake was >400–500°C, inferred from the thermal decomposition of paramagnetic minerals with the formation of ferrimagnetic minerals (Table 1; Chou, Song, Aubourg, Song, et al., 2012; Mishima et al., 2006, 2009; Tanikawa et al., 2007, 2008). This estimate concurs with others based on nonmagnetic thermal indicators: The signature of mobile trace elements in the fault fluid indicates a frictional heating peak temperature >350°C (Ishikawa et al., 2008). That temperature is estimated at >300–400°C based on the vaporization of water during thermal pressurization (Boullier et al., 2009). These peak temperatures estimates are lower than the estimate of 626 ± 25°C from a kinetic model of vitrinite thermal maturation (Maekawa et al., 2014), and the infrared and Raman estimates from carbonaceous fault materials (≥700°C, Hirono et al., 2015). The clay mineral signature would indicate that the peak temperature could even be up to 900–1100°C (L.-W. Kuo et al., 2011). Most recently, nanometric geochemical analysis of fault gouge revealed that most of the siderite in the slip zone has been evaporated into nanosized grains, suggesting that the peak temperature reached as high as ~1200°C (W.-H. Li et al., 2019). While the actual peak temperature is still not well defined, the existence of frictional heating has been definitively verified by the 0.06°C residual temperature anomaly measured 6 years after the 1999 Chi-Chi earthquake rupture through direct borehole temperature logging (Table 1; Kano et al., 2006). A similar situation exists in the Japan Trench subduction plate boundary fault zone which accommodated the large slip of the 2011 Tohoku-oki earthquake (Table 1) with a thermal of anomaly of 0.31°C measured 16 months after rupture (Fulton et al., 2013).

The peak temperature estimates obtained by different methods thus appear to be quite variable. A possible reason could be that different thermal proxies sense correctly certain temperature intervals only (cf. Figure 14, see also Rowe & Griffith, 2015; Yang, Dekkers, & Zhang, 2016). Another reason could be that the majority of the temperature estimates take equilibrium conditions as their basic premise, which may not apply to the timescales of fault slip (e.g., Savage et al., 2018). This clearly warrants further work. However, at present we may deduce that peak temperature estimates of fault rocks inferred from magnetic properties are reasonably in line with the majority of other methods and provide at least a lower bound on the temperature rise due to seismic frictional heating.

In other cases examination of magnetic assemblages can provide an upper limit for the temperature of the frictional heating. This is the case in the Nankai subduction zone (Japan) associated with the 1944 Tonankai *Mw* 8.1 earthquake, where the absence of thermal decomposition of paramagnetic minerals indicates a peak temperature <400°C (Table 1; Hirono et al., 2009). This peak temperature estimate is corroborated by estimates from other thermal indicators, such as the fluid-mobile trace element signature, the Raman spectral features of carbonaceous material, and the inorganic carbon content (these parameters all indicate <300°C, Hirono et al., 2009, 2014). Also, vitrinite reflectance data (peak temperature 390°C, cf. Sakaguchi et al., 2011) support the magnetic information. It further shows that magnetic property analysis of fault rocks can provide at least a reasonably robust thermal record of earthquake slip. It should be realized that the amount of frictional heating can vary widely for different earthquakes; the related temperature rise is as yet rather poorly constrained by any individual method. Therefore, all approaches are subject to ongoing testing and refinement. Combined application, reconciliation and cross calibration of different thermometers would thus yield the most robust picture. This is also where the magnetic methods will be playing an important role.

6.2. Stress Orientations

In the Japan Trench subduction fault zone, the maximum AMS axes of sedimentary rocks in the frontal prism align northeast-southwest (36.6 ± 11.3°, Figure 21c, Yang, Mishima, et al., 2013). This is nearly perpendicular to the direction of the Pacific plate convergence (~292°, Argus et al., 2011) and the maximum horizontal stress orientation (319 ± 23°) deduced from the azimuths of borehole breakouts (W. Lin et al., 2013; see Appendix A for definition). The accretionary prism sediments thus probably have undergone layer parallel shortening due to the convergence of the Pacific plate. Similar AMS patterns have also been reported in the TCDP core samples, where the magnetic ellipsoids are coaxial with the (palaeo)stress ellipsoids deduced from fold axes, fault analysis, and borehole breakouts (cf. Figure 14b in Louis et al., 2008). Hence, these observations provide a strong validation of the reliability of AMS as a (palaeo)stress indicator within fault systems.

7. Remaining Challenges

The foregoing discussion illustrates that the rock magnetic approach is very promising to unveil valuable information pertaining to faulting processes. Comparison of magnetic and nonmagnetic approaches, as low as the number of comparative studies at this moment, yields a broad agreement among most of the approaches. Moreover, they have improved our understanding of the magnetic signatures of fault rocks.

Nonetheless, some essential questions pertaining to the mechanisms that underlie the magnetic changes in fault rocks remain currently unanswered. Most importantly, the reaction kinetics of Fe-bearing (magnetic) mineral reactions under the extreme faulting conditions (i.e., fast heating, intensive mechanical milling, and nanocrystallization) are not well understood. On the other hand, other than the protolith lithology, magnetic properties of fault rocks are strongly affected not only by physicochemical conditions (temperature, pressure, oxygen fugacity, pH, etc.) during rupture but also by alteration and chemical differentiation within a fault zone during the other stages of the seismic cycle, that is, the postseismic, and interseismic periods (e.g., Bense et al., 2013; Ferré et al., 2017; O'Hara & Huggins, 2005; Yamaguchi et al., 2011). This complicates the magnetic signature interpretation of fault rocks. The individual impact of each stage of the seismic cycle must be untangled before a full understanding of faulting behavior is obtained. For example, fluid-rock interaction plays a key role in the alteration, removal, and/or neoformation of Fe-bearing minerals in fault zones. Unfortunately, the associated kinetics are presently rather poorly understood (e.g., Chou, Song, Aubourg, Song, et al., 2012; Yang, Chen, et al., 2013; Yang, Yang, et al., 2016). Also, identification of a

PSZ and the signature of frictional heating of individual earthquake events are not "one to one", as a fault zone is the cumulative product of many earthquake cycles, and thus, several PSZs may stack together in a fault gouge. These challenges warrant future work.

Next, we identify some attractive research avenues to help addressing these concerns, including (1) extensive magnetic analysis on fault rocks after friction experiments, (2) laboratory simulation of fault fluid percolation, (3) emerging technology for resolving faulting imprinted NRM components, (4) magnetic fabric analysis of brittle fault rocks, and (5) synergy of interdisciplinary approaches in mineral-magnetic studies.

7.1. Extensive Magnetic Analysis on Fault Rocks After Frictional Experiments

Friction impacts the formation and/or destruction of Fe-bearing (magnetic) minerals. Mechanical milling in air can completely transform hematite to magnetite (Petrovský et al., 1996, 2000; Zdujić et al., 1998); mechanical friction in argon favors the thermal decomposition of pyrite into pyrrhotite (H.-P. Hu et al., 2002) while mechanochemical decomposition of siderite due to crushing may produce magnetite (Criado et al., 1988). Similar processes can readily occur in seismic slip zones during earthquakes (e.g., J. P. Evans et al., 2014). Experimental calibration of the reaction kinetics on time-temperature paths similar to those expected on fault surfaces during seismic slip may enable precise determination of the concomitant temperature rise. Therefore, laboratory high-speed friction experiments using rotary shear apparatus (e.g., Di Toro et al., 2010; S. Ma et al., 2014) on natural and synthetic fault gouges are promising to precisely constrain the processes that occurred in a fault zone during rupture. Such experiments could be carried out on samples with various compositions focusing on the suite of Fe-bearing minerals and under different conditions (e.g., variable oxygen fugacity, permeable/impermeable, high vapor pressure, hydrostatic, and elevated temperature). Real-time records of physical parameters, that is, temperature, velocity, stress, displacement, provide high-resolution information on the "flash-heating" effects due to the friction. Therefore, studies should ideally integrate mineral magnetic, mineralogical, geochemical, and microscopic aspects on fault gouges before and after experimental shearing. Also, they should be complemented by kinetic chemical modeling and temperature modeling. With such data, our understanding of the evolution of Fe-bearing (magnetic) mineral(s) within the PSZ during slip will be put on a much stronger footing. In addition, similar experiments under low-speed conditions (as low as the mm/year range, cf. Collettini et al., 2014, and S. Ma et al., 2014) may shed light on the possible magnetic response during earthquake nucleation.

7.2. Laboratory Simulation of Fluid Percolation

Fluids along fault zones are generally of multiple sources (Zoback et al., 2007). Their migration paths and compositions vary markedly over time and space, as fault zones act as fluid conduits or barriers at different stages in their development, that is, the coseismic, postseismic, and interseismic periods (Bense et al., 2013). This leads to temporal and spatial changes of the redox state in a fault zone as a function of episodic fault rupture and healing cycles during the lifetime of a fault (Yamaguchi et al., 2011). Laboratory simulation of such processes with natural and/or synthetic fault rocks under controlled physicochemical conditions (i.e., temperature, pressure, redox state, pH, and fluid-rock ratio) thus would be a promising way to improve our understanding of alteration, removal, and/or neoformation of magnetic minerals as a result of fluid infiltration. Answers may be retrieved from characterizing the Fe-bearing and associated minerals which are precipitated or recrystallized, such as iron oxides, iron hydroxides, iron carbonates, and/or iron sulfides, in incorporation with thermochemical equilibrium modeling under the specific experimental physicochemical conditions.

7.3. Emerging Technology for Resolving Faulting Imprinted NRM Components

Isolation and characterization of faulting-induced NRM components are expected to yield valuable information on faulting-related effects. With the exception of a few early studies on paleomagnetic dating of fault rocks (e.g., Grønlie & Torsvik, 1989; Hailwood et al., 1992; Torsvik et al., 1992); however, little attention has been paid to newly imprinted "secondary" coseismic/postseismic NRM components, such as related (p)TRM or CRM (e.g., Chou, Song, Aubourg, Lee, et al., 2012, see section 5.3) and potential EQLIRM (e.g., Ferré et al., 2012; see section 5.5). This is most likely dictated by the amount of sample material needed for the required precise determination of paleomagnetic signatures by classic paleomagnetic measurements.

Alternative options include the aforementioned SSM and QDM. The SSM is capable of mapping magnetic fields with high spatial resolution (better than 100 μm at room temperature and 4 μm or better at

cryogenic temperatures), with a limiting magnetic moment sensitivity of ~1×10^{-14} Am^2 at a sensor-to-sample distance of 200 μm (e.g., Fukuzawa et al., 2017; Pastore et al., 2018). It has been successfully applied in various paleomagnetic studies, such as on lunar glass spherules and Hawaiian basalt (Weiss et al., 2007) and ferromanganese crust (Noguchi et al., 2017). In the fault slip context, magnetic stripes with positive and negative polarities subparallel to the slip surface were recently detected by Fukuzawa et al. (2017) on the Nojima Fault gouge (Japan) within an area of 1 cm × 1 cm, using SSM. Such NRM distribution patterns in fault gouge could provide a means to distinguish prehistorical periods of earthquake activity on the slip zone with the help of the geomagnetic polarity timescale. The QDM is a combination of superior spatial resolution (5 μm), magnetic sensitivity (20 μT μm/$Hz^{1/2}$), and wide field of view (4 mm) (Glenn et al., 2017). It can image both remanent and induced magnetization of geological samples at room temperature (Glenn et al., 2017). These emerging microscopic magnetic scanning techniques enable micrometer-scale paleomagnetic studies of fault zones. They also offer spatially well-resolved measurements of magnetic signals of the narrow fault zones. Thus, they represent a very promising way to resolve the cumulative frictional heating effects in PSZs caused by recurrent (historical) earthquakes.

7.4. Magnetic Fabric Analysis of Brittle Fault Rocks

Fault zones are most complex study targets. The caveats put forward by Ferré, Gébelin, et al. (2014) for ductile shear zones also apply to brittle fault rocks in the shallow crust. First, mineral assemblages and mechanical properties of fault zones are heterogeneous between and within the different fault zone compartments that is, damage zone, fault breccia, and fault gouge. The AMS fabrics in each zone could well have their individual strain relationship. Meanwhile, faulting-related process (frictional heating and fluid-rock interactions) tends to induce alteration of mineral assemblages that would not necessarily relate to strain (e.g., Just et al., 2004). The observed changes in AMS thus cannot be solely attributed to deformation and evidently complicate the relation of AMS with strain in a fault zone. As an example, the AMS fabric of fault gouges in the Nojima Fault (Japan) is isotropic (Nakamura & Nagahama, 2001). However, it is anisotropic in the Chelungpu Fault in Taiwan (Yeh et al., 2007). Integrated rock magnetism, mineralogy and geochemistry, microstructural observations, and possibly the determination of other magnetic fabrics (high field and low temperature) and the AMR analysis are desired to fully unravel the relation between magnetic fabric and the deformation mechanisms operating during faulting.

In addition, the neoformed magnetic minerals and paramagnetic/diamagnetic minerals in fault rocks may well be formed at different faulting stages or events and could have distinct deformation paths. For example, diamagnetic fabric of coccolith calcite from the plate boundary Dead Sea Fault indicates tectonic strain, while the paramagnetic fabric of clays preserves the depositional fabric (Issachar et al., 2018). Thus, evaluation of the relative contributions from the ferrimagnetic, paramagnetic, and diamagnetic components to the bulk AMS (e.g., Ferré et al., 2004; Hrouda & Jelínek, 1990; Kelso et al., 2002; Martín-Hernández & Ferré, 2007) and examination of the (weak) field dependence of AMS, as well as the out-of-phase and in-phase components of AMS, could be insightful into the dynamic deformation processes in a fault zone.

7.5. Synergy of Interdisciplinary Approaches in Mineral-Magnetic Studies

The various structural domains of a fault zone that is, fault core, damage zone, and host rock, have a very diverse level of faulting effects and number of rupture episodes. Attention should thus be paid not only to bulk magnetic properties of these different fault rocks (e.g., fault breccia, cataclasite, and fault gouge) but also the different components of fault rocks should be considered individually. Fault breccia, for instance, generally comprises a mixture of fragments with different grain sizes, set in a finer-grained, clay-rich matrix (Figure 17a). With their heterogeneous hydraulic structure and specific surface, alteration associated with faulting processes (fluid percolation in particular) acts on them to quite different extents (Yang, Chen, et al., 2013; Yang, Yang, et al., 2016). Consequently, an assessment of the relative contributions of different components in fault rocks to the overall magnetization, and unraveling their individual alteration processes are of great help for understanding the changes in magnetic minerals as a fault zone evolves. This could be achieved through combination with mineralogical, geochemical, and microscopic analyses, other than mere rock magnetic examination of the iron-bearing minerals (e.g., Fe oxides, Fe hydroxides, Fe sulfides, Fe carbonates, or Fe-silicates) in fault materials.

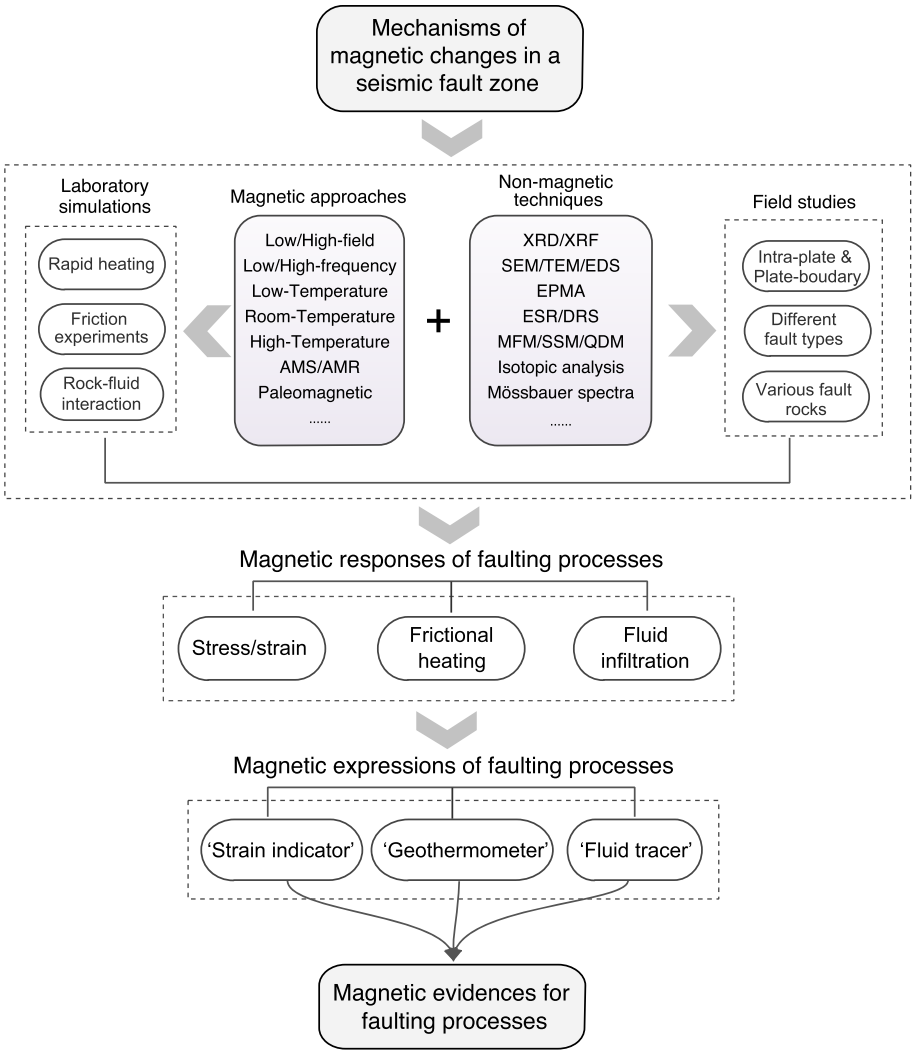

Figure 22. A flowchart for the magnetic property analysis of fault rocks. Multidisciplinary and integrated approaches incorporating field studies, laboratory simulations, high-resolution microscopy, and numerical modeling are proposed as a most promising way to gain a full appreciation of the magnetic response to dynamic physicochemical processes in fault zones. With a research effort along such lines, better rock magnetic "strain indicators," "geothermometers," and "fluid tracers" are expected to become available for fault zone studies. XRD, X-ray diffraction; XRF, X-ray fluorescence; SEM, scanning electron microscopy; TEM, transmission electron microscopy; EDS, energy dispersive spectroscopy; EPMA, electron probe microanalysis; ESR, electron spin resonance; DRS, diffuse reflectance spectroscopy; MFM, magnetic force microscopy; SSM, scanning SQUID microscopy; and QDM, quantum diamond magnetometry.

The thickness of PSZ and microstructures in fault zones is often at the millimeter to even micrometer scale (e.g., Boullier, 2011; Fondriest et al., 2013; Sibson, 2003; Siman-Tov et al., 2013). Thus, with magnetic studies at a microscale one should be able to gather most meaningful information on temperature changes within a PSZ. Next to the above-mentioned SSM and QDM, advanced techniques for magnetic imaging at microscale/nanoscale are recommended in future studies, including but not limited to magnetic tunnel junction for mapping magnetic fields with high spatial resolution and field sensitivity (e.g., Lima et al., 2014) and synchrotron radiation analysis that enables imaging the three-dimensional structures of nanosized magnetic minerals (e.g., Chou, Song, Tsao, et al., 2014), as well as the deformation microfabrics in fault zones (e.g., Fusseis et al., 2014). Orientation statistics from three-dimensional structure of magnetic particles then become valuable, which could be matched with, for example, AMS or other magnetic techniques (e.g., Petri et al., 2020).

8. Conclusions

We have examined the pros and cons of rock magnetic methods applied to fault zones. After identifying candidate mechanisms for magnetic changes in fault rocks, we summarize the recent advances of such studies on fault rocks, highlighting the insights that were gained from these studies. It has been demonstrated that the rock magnetic properties can be employed as "strain indicator", "geothermometer", and "fluid tracer" in fault zones. This opens a new window into investigating faulting processes.

This emerging subdiscipline is promising and challenging at the same time. Magnetic properties of fault rocks hold many secrets that await discovery; multidisciplinary and integrated approaches are crucial to gain a full appreciation of magnetic response to dynamic physicochemical processes in fault zones (Figure 22). Other than magnetic investigations of fault rocks from earthquake faults, laboratory experiments (friction experiments, milling, rapid thermal treatment, and fluid percolation, etc.) on both natural and synthetic fault rocks should be taken into consideration. Additionally, kinetic, equilibrium, and thermodynamic modeling incorporating the results of field studies and laboratory simulations should be included. All of these efforts would serve to unraveling the mechanisms responsible for magnetic changes in a fault zone, and contribute to the development and refinement of rock magnetic "strain indicators", "geothermometers", and "fluid tracers" in fault zones. This will ultimately yield a better tool for illuminating faulting processes.

Appendix A: Glossary

A.1 Part I: Rock Magnetic Terms

- *Anisotropy of (low-field) magnetic susceptibility (AMS)*: The low-field susceptibility varies slightly as a function of orientation of the sample with respect to the applied field (with a strength of up to several times the Earth's magnetic field). This variation is described by a symmetric tensor, the AMS tensor. AMS reflects the statistical alignment of crystallographic directions and/or shape in platy or elongate grains. Next to AMS also the anisotropy of various remanences imparted in the laboratory is occasionally evaluated, mostly the AARM.
- *Antiferromagnetic*: A state of magnetic order with two ferromagnetic sublattices of equal size aligned antiparallel so that (ideally) no net magnetic moment results. In practice, a small magnetic moment persists because of small deviations from the perfect antiparallel state or defects in the crystal structure. Example: hematite.
- *Chemical remanent magnetization (CRM)*: The NRM imparted to magnetic minerals by chemical processes, at any temperature below their Curie temperatures, in the presence of an ambient geomagnetic field. Chemical processes involve grain growth beyond the SP grain size or thermochemical alteration of existing magnetic minerals to other magnetic minerals.
- *Coercive force (B_c) and coercivity of remanence (B_{cr})*: see magnetic hysteresis loop and parameters.
- *Curie temperature* (T_C): As the temperature increases in a ferromagnetic (sensu lato) material, interatomic distances increase, and the magnetic exchange interaction that describes the collective ordering of atomic magnetic moments becomes weaker. At T_C, the thermal energy overcomes the exchange energy, and individual atomic magnetic moments become independent (they lose their long-range ordering) so that the material becomes paramagnetic. Named after the French physicist Pierre Curie (1859–1906).
- *Diamagnetic*: A material is diamagnetic when all electron spins are paired. When exposed to a magnetic field, a diamagnetic material tends to reduce that magnetic field: Its susceptibility is negative (the induced magnetization is opposite to the applied field). The value is very small and independent of temperature. Examples: quartz (SiO_2) and calcite ($CaCO_3$).
- *Ferrimagnetic*: A state of magnetic order in which two ferromagnetic sublattices of unequal magnitude are aligned antiparallel to each other. Example: magnetite.
- *Ferromagnetic*: A state of magnetic order in which all atomic magnetic moments are aligned parallel to each other. Example: metallic iron.
- *First-order reversal curve (FORC) diagrams*: FORCs are partial hysteresis loops determined with the following procedure: (1) a positive saturation field is applied, (2) the field is ramped down to a lower reversal field, and (3) the magnetization of the sample is measured, while the applied field is ramped upward to positive saturation again. A series of FORCs is measured for a set of reversal fields that are increasingly

away from positive saturation, and a FORC distribution is calculated as the mixed second derivative of magnetization with respect to field spacing; it is displayed in a so-called FORC diagram. FORC diagrams provide information about the distribution of switching fields (i.e., coercivities) and interaction fields for all magnetic particles that contribute to a hysteresis loop. They are widely used to characterize samples in rock and mineral magnetism.

- *Frequency-dependent magnetic susceptibility*: The difference between susceptibility measurements made at two frequencies (e.g., 0.47 and 4.7 kHz), expressed either as a percentage of the low frequency or as an absolute susceptibility value (i.e., in $m^3\ kg^{-1}$ for mass-specific susceptibility or in dimensionless units for volume-specific susceptibility). This measurement denotes the presence of magnetically "viscous" ferrimagnetic (magnetite or maghemite) grains lying at the stable single domain (SSD)/SP boundary.
- *Hysteresis parameters*: see magnetic hysteresis loop and parameters.
- *In-phase and out-of-phase magnetic susceptibility*: When measuring susceptibility in low alternating magnetic fields, the measured specimen is magnetized by a weak field sinusoidally varying in time: $H(t) = H_0\cos(\omega t)$, where H_0 is the field amplitude, ω the angular frequency, and t the time. The magnetic response is measured, most conveniently represented by magnetization $M(t)$. In diamagnetic, paramagnetic, and many ferromagnetic (sensu lato) materials, the magnetization also varies sinusoidally being in phase with the applied field. The magnetization to field ratio then maintains a constant value that represents the susceptibility. In some ferromagnetic materials, however, the magnetization is not in phase with the applied field but lags behind the field usually because of electrical conduction. In that case M' and M'' are the in-phase and out-of-phase magnetization components, respectively. Then, the in-phase susceptibility is $\chi' = M'/H_0$ and the out-of-phase susceptibility is $\chi'' = M''/H_0$. See Hrouda et al. (2016) for more details.
- *Magnetic domain*: A portion of a ferromagnetic/ferrimagnetic material in which the atomic magnetic moments are aligned. In a magnetic material, magnetic domains serve to reduce the magnetostatic energy due to the aligned spontaneous magnetization. Fine magnetic grains are SD, and larger grains contain several magnetic domains. The magnetic domains form a structure in which the magnetic moments of individual magnetic domains cancel each other out as much as possible. As a result, the spontaneous magnetization of the overall magnetic body is reduced, leading to a lower magnetostatic energy state which represents a most stable energy configuration.
- *Magnetic susceptibility*: A measure of the ease with which a substance can be magnetized in small, Earth-like, applied magnetic fields. The magnetic moment divided by the field strength in units of H (i.e., $A\ m^{-1}$) is the susceptibility. Volume susceptibility (κ) is the induced magnetization per unit volume divided by the field strength, and is a dimensionless quantity. Mass-specific susceptibility (χ) is the magnetic moment expressed per unit of mass divided by the field strength; it has units of $m^3\ kg^{-1}$, that is the inverse of the specific density of a material. Magnetic susceptibility depends principally on the type and concentration of magnetic minerals in a sample; grain-size dependence is marginal (with the exception of superparamagnetism that occurs below ~25 nm at room temperature).
- *Magnetic remanence*: Magnetization that persists in the absence of an applied magnetic field. It differs from induced magnetization that disappears on removal of an applied field.
- *Magnetic hysteresis loop and parameters*: A hysteresis loop results when the in-field magnetization of a sample is measured as the inducing field is cycled between high positive and negative values. A hysteresis loop can be measured at any temperature; most hysteresis loops are acquired at room temperature. The shape of the hysteresis loop yields pertinent information about the magnetic mineral(s) present in a sample and most importantly on their grain size. The maximum-induced magnetization that can be induced in a sample is termed the saturation magnetization (M_s). The corresponding remanence, when the applied field is reduced to 0, is the saturation remanence (M_{rs}), and the reversed magnetic field required to reduce the magnetization to zero is the coercive force (B_c). The coercivity of remanence (B_{cr}): The oppositely directed magnetic field required to demagnetize the saturation remanent magnetization to zero. The M_{rs}/M_s ratio is often plot against the B_{cr}/B_c ratio, named the Day plot (after Ron Day) which features magnetic grain size regions. Without additional information on the magnetic mineralogy and their oxidation state interpretations in terms of grain size should be exercised with caution.
- *Magnetic saturation*: The maximum magnetic moment a sample can achieve. Increasing the field strength even further does not impart a higher magnetic moment.

- *Magnetic vortex state*: The transitional state between SD and MD particles, more traditionally termed PSD. When a SD particle becomes larger the magnetic moments tend to "flower out" in the corners of that particle. This state is termed flower state. In slightly larger particles the atomic spin magnetic moments curl within the particle around one or more cores. This state is called vortex state. An ideal vortex has a low magnetostatic energy because the particle's residual magnetic moment is low. Vortex cores may evolve into classic magnetic domains in yet slightly larger grains.
- *Magnetostatic interactions*: When magnetic particles are located sufficiently close to each other, their magnetic fields will interact. The interaction field depends on the configuration of neighboring particles and will be stronger if more adjacent particles are magnetized in the same direction. Magnetostatic interactions are an important factor to explain the magnetic properties of closely spaced aggregates or intergrown magnetic particles in earth materials.
- *Magnetostriction*: a property of ferromagnetic (sensu lato) materials which causes them to expand or contract in response to an external magnetic field. It is considered to be a coupling effect between the magnetic energy and the mechanical energy observed in ferromagnetic materials under the influence of the external magnetic field.
- *Multidomain (MD)*: With increasing grain size, the magnetostatic energy of a magnetic particle increases. To minimize this energy, a particle will begin to nucleate domain walls at a critical grain size threshold. These walls divide the particle into two or more magnetic volumes or domains. The magnetization is uniform in each domain, but it differs in direction from domain to domain. The transition between small grains with only one domain (termed SD) and MD grains is not sharp; a size range exists with a noncollinear spin structure that may contain a few domains.
- *Natural remanent magnetization (NRM)*: The remanent magnetization that has been acquired naturally (i.e., not artificially acquired in a laboratory). It is the remanent magnetization of a rock that is present before any laboratory experiments are carried out. This preserves a record of the Earth's magnetic field at the time the mineral was laid down as sediment or crystallized in magma. In many cases, that original NRM component—termed primary NRM—can be retrieved from the composite NRM with paleomagnetic techniques. Thus, with paleomagnetic data the original position of rock units can be reconstructed, so their plate tectonic movement can be quantified.
- *Néel temperature* (T_N): In antiferromagnetic substances, the individual magnetic moments are aligned antiparallel to one another below a certain critical temperature, which is known as Néel temperature (T_N). In practice, Curie and Néel temperature are being used interchangeably. Named after the French physicist Louis Néel (1904–2000).
- *Paramagnetic*: The magnetic state in materials with uncompensated electron spins that do not behave collectively, that is each free electron spin is an individual atomic magnet. In an applied magnetic field these moments will partially align to that applied field: A paramagnetic material will be magnetized in the direction of its inducing magnetic field. When the field is removed, the induced magnetic moment disappears instantaneously. Paramagnetism is proportional to the inverse of the absolute temperature.
- *Pseudo single domain (PSD)*: A magnetic structure that is intermediate between the single-domain (SD) and MD states. A PSD particle contains more than one domain (up to ~5–7) but exhibits many of the stable magnetic properties typical of SD particles. See also magnetic vortex state.
- *Saturation magnetization (M_s), saturation remanent magnetization* (M_{rs}): see hysteresis loops.
- *Single domain (SD)*: A uniformly magnetized magnetic particle with a single magnetic domain. In most ferromagnetic and ferrimagnetic minerals, SSD grains are extremely small (the SD size range in equant magnetite is ~30–80 nm at room temperature).
- *Superparamagnetism (SP)*: Class of magnetic behavior exhibited by very small particles (< ~25–30 nm in magnetite at room temperature) with relaxation times (the magnetic decay time equivalent to the half-life of radioactive elements) smaller than laboratory timescales (typically taken at 100 s). For these particles, atomic magnetic moments align in low, Earth-like, applied magnetic fields to produce a strong induced magnetization that is rapidly attenuated by thermal vibration after removal of the field (seconds to minutes).
- *Thermal remanent magnetization (TRM), also thermoremanent magnetization*: The remanent magnetization that is acquired by a sample when it is cooled in the ambient geomagnetic field, from above the Curie temperature of the constituent magnetic minerals.

A.2 Part II: Fault Rock and Faulting-Related Terms

- *Borehole breakout*: Drilling-induced compressive failures of the borehole wall occur once the stress exceeds the strength of the rock or sediment. Their geometry is believed to replicate reliably the orientation and magnitude of in situ principal stress. Borehole breakouts are deemed to be key indicators of the stress state in the subsurface. See Zoback et al. (2003) for more details.
- *Brittle deformation*: Deformation involving a "throughgoing discontinuity" in the rock. It includes tensile cracking, shear fracturing, and frictional sliding. Brittle deformation occurs when the stresses on a rock exceed the failure strength of the rock, causing a loss of cohesion.
- *Cataclasite*: A fine-grained, cohesive fault rock that generally forms at shallow depths in the crust (typically from ~5 to ~10–15 km), dominantly by brittle deformation processes such as microcracking and abrasion. It may be subdivided according to the relative proportion of finer-grained matrix into protocataclasite (with 10–50% matrix), mesocataclasite (with 50–90% matrix) and ultracataclasite (90–100% matrix).
- *Cataclastic flow* :Distributed brittle deformation associated with motion of rock particles on a large collection of cracks and/or frictional surfaces.
- *Clast*: Fragments of rock surrounded by a finer-grained matrix.
- *Clastic dike*: A seam of sedimentary material that fills in an open fracture and cuts across sedimentary rock strata or layering in other rock types. Clastic dikes form rapidly by fluidized injection (mobilization of pressurized pore fluids) or passively by water, wind, and gravity (sediment swept into open cracks).
- *Damage zone*: The region encompassing a mappable network of subsidiary brittle deformation structures surrounding the fault core. These structures may include small faults, veins, fractures, cleavage, and folds (Caine et al., 1996).
- *Ductile deformation*: "Continuous and homogeneously distributed" deformation. It can involve numerous mechanisms ranging from macroscopic cataclastic flow to crystal-plastic processes (Snoke et al., 1998). Ductile deformation occurs when the stresses on a rock cause permanent strain, without the loss of cohesion.
- *Earthquake nucleation*: The precursor stage preceding the dynamic rupture propagation of an earthquake (with negligible inertial effects), which involves quasi-static, aseismic slippage of a fault surface that has a maximum scale termed "nucleation length."
- *Earthquake energy dissipation*: During an earthquake, the elastic strain energy accumulated during the interseismic period is released by rapid fault frictional sliding. The total energy released (E_{tot}) is partitioned into breakdown work (W_b), frictional heat (E_H), and radiated energy (E_R), that is, $E_{tot} = W_b + E_H + E_R$. Note that W_b includes the fracture (surface) energy G, which is the energy required to cause fracture near the tip of a fault during rupture, and the remainder is also transferred to frictional heat. E_H is the energy dissipated by frictional heating during slippage and is often considered to be the largest component (~80–90%) of the total energy budget. Increasing temperature during coseismic slip can trigger various chemical reactions and phase transitions. These processes are mostly endothermic, but the taken-up energy (often referred to as the EC) is usually minor (<1%) compared with frictional heat generated.
- *Fracture*: A general term for any break in a rock mass, whether or not it causes displacement, including cracks, joints and faults.
- *Fault breccia*: A coarse-grained incohesive fault rock, formed by brittle deformation processes, consisting of at least 30% visible fragments (>0.1 mm).
- *Fault core*: A zone (often asymmetric) enclosed by damage zones that results from the highly localized strain and intense shearing that accommodates the majority of the displacement within the fault zone. It generally consists of a number of recurring slip surfaces and fault rocks such as gouges, cataclasites, and breccias.
- *Fault gouge*: An incohesive, clay-rich fine- to ultrafine-grained cataclasite, which may possess a foliation and contains <30% visible fragments. Lithic clasts may be present.
- *Matrix*: Groundmass of fine-grained material, often surrounding larger fragments.
- *Mylonite*: A fault rock which is cohesive and characterized by a well-developed foliation resulting from tectonic grain-size reduction derived from crystal plastic processes. It commonly contains rounded porphyroclasts and lithic fragments of similar composition to minerals in the matrix. Mylonites may be

subdivided according to the relative proportion of fine-grained matrix into protomylonite, mesomylonite and ultramylonite, which feature grain-size reduction in respectively <50%, 50–90%, and >90% of the rock volume.

- *Principal slip zone (PSZ)*: The fault plane along which the most slip is accommodated during a single earthquake event. It is located within the fault core, surrounded by the damage zone. Synonyms: principal slip surface (PSS) and principal slip plane (PSP).
- *Pseudotachylyte*: A cohesive fault rock that occurs as solidified melts produced by frictional heating during seismic slip. It is typically dark in color and is glassy in appearance. Generally, quick, quench cooling of the melt along the main fault plane forms a pseudotachylyte generation vein. Sometimes, some of the melt may intrude minor faults or coseismic fractures into the wall rock; the resulting veins are termed injection veins.
- *Velocity-strengthening/weakening*: The fault strength in the brittle crust is a function of two basic parameters: the effective normal stress and the coefficient of friction. A fault may be strong and slip stably, or weak and fail in large earthquakes. To explain differences between stable sliding (aseismic) and unstable stick-slip (seismogenic) behavior, frictional velocity dependence is considered the most likely mechanism. Materials that exhibit velocity strengthening (frictional resistance increases with sliding velocity) produce only inherently stable frictional slip, whereas those that exhibit velocity-weakening (frictional resistance decreases with sliding velocity) frictional behavior are capable of hosting unstable rupture.

Data Availability Statement

Data of Figure 4d can be found at Yang et al. (2018); data of Figures 6a–6d are available in Özdemir et al. (1993, 2008), Dekkers et al. (1989), and Guyodo et al. (2006); and data in Figures 11b and 11c are from Chou, Song, Aubourg, Song, et al. (2012) and Chou, Song, Aubourg, et al. (2014). The data used to create Figure 5 can be found in the Magnetics Information Consortium (at https://doi.org/10.7288/V4/MAGIC/16879).

Acknowledgments

This work was supported by the National Science Foundation of China (NSFC) grant numbers 41874105, 41472177, and 41204062 to T. Y. Y. M. C. was funded by the Shenzhen Science and Technology Program under grant KQTD20170810111725321, Science and Technology Innovation Committee of Shenzhen Municipality under grant ZDSYS201802081843490, and the Southern University of Science and Technology under grants K19313901 and Y01316111. This work was also supported by the National Science Council of Taiwan (grants NSC 101-2116-M-003-005 and NSC 102-2116-M-003-003 to E. C. Y. and Y. M. C.) and National Science Foundation (Instrumentation and Facilities grant EAR-0521558 and Geophysics grant EAR-0228818 to E. C. F.). M. J. D. acknowledges support from Netherlands Science Foundation (NWO) Deep NL grant 2018.040. We are grateful to Huan Wang and Tsafrir Levi for providing the original copies of Figures 2h and 19, respectively. We thank Toshiaki Mishima for discussions on an earlier version of the manuscript. We also thank Silvia Mittempergher, Bjarne S. G. Almqvist, and two anonymous reviewers for their insightful comments and suggestions that helped to improve the manuscript significantly. The Editor-in-Chief Fabio Florindo is acknowledged for the efficient handling of the manuscript.

References

Aben, F. M., Dekkers, M. J., Bakker, R. R., van Hinsbergen, D. J. J., Zachariasse, W. J., Tate, G., et al. (2014). Untangling inconsistent magnetic polarity records through an integrated rock magnetic analysis: A case study on Neogene sections in East Timor. *Geochemistry, Geophysics, Geosystems*, *15*, 2531–2554. https://doi.org/10.1002/2014GC005294

Aharonov, E., & Scholz, C. H. (2019). The brittle-ductile transition predicted by a physics-based friction law. *Journal of Geophysical Research: Solid Earth*, *124*, 2721–2737. https://doi.org/10.1029/2018JB016878

Almeida, T. P., Muxworthy, A. R., Kovács, A., Williams, W., Brown, P. D., & Dunin-Borkowski, R. E. (2016). Direct visualization of the thermomagnetic behavior of pseudo-single-domain magnetite particles. *Science Advances*, *2*, e1501801. https://doi.org/10.1126/sciadv.1501801

Almqvist, B. S. G., Bender, H., Bergman, A., & Ring, U. (2020). Magnetic properties of pseudotachylytes from western Jämtland, central Swedish Caledonides. *Solid Earth*, *11*(3), 807–828. https://doi.org/10.5194/se-11-807-2020

Almqvist, B. S. G., & Koyi, H. (2018). Bulk strain in orogenic wedges based on insights from magnetic fabrics in sandbox models. *Geology*, *46*(6), 483–486. https://doi.org/10.1130/G39998.1

Aretusini, S., Mittempergher, S., Plümper, O., Spagnuolo, E., Gualtieri, A. F., & Di Toro, G. (2017). Production of nanoparticles during experimental deformation of smectite and implications for seismic slip. *Earth and Planetary Science Letters*, *463*, 221–231. https://doi.org/10.1016/j.epsl.2017.01.048

Aretusini, S., Spagnuolo, E., Dalconi, M. C., Di Toro, G., & Rutter, E. H. (2019). Water availability and deformation processes in smectite-rich gouges during seismic slip. *Journal of Geophysical Research: Solid Earth*, *124*, 10,855–10,876. https://doi.org/10.1029/2019JB018229

Argus, D. F., Gordon, R. G., & DeMets, C. (2011). Geologically current motion of 56 plates relative to the no-net-rotation reference frame. *Geochemistry, Geophysics, Geosystems*, *12*, Q11001. https://doi.org/10.1029/2011GC003751

Banerjee, S. K., Hunt, C. P., & Liu, X. (1993). Separation of local signals from the regional paleomonsoon record of the Chinese Loess Plateau: A rock-magnetic approach. *Geophysical Research Letters*, *20*(9), 843–846. https://doi.org/10.1029/93GL00908

Banerjee, S. K., King, J., & Marvin, J. (1981). A rapid method for magnetic granulometry with applications to environmental studies. *Geophysical Research Letters*, *8*(4), 333–336. https://doi.org/10.1029/GL008i004p00333

Bense, V. F., Gleeson, T., Loveless, S. E., Bour, O., & Scibek, J. (2013). Fault zone hydrogeology. *Earth-Science Reviews*, *127*, 171–192. https://doi.org/10.1016/j.earscirev.2013.09.008

Berman, R. G., Ya Aranovich, L., & Pattison, D. R. M. (1995). Reassessment of the garnet-clinopyroxene Fe-Mg exchange thermometer: II. Thermodynamic analysis. *Contributions to Mineralogy and Petrology*, *119*(1), 30–42. https://doi.org/10.1007/BF00310715

Berndt, T., Muxworthy, A. R., & Fabian, K. (2016). Does size matter? Statistical limits of paleomagnetic field reconstruction from small rock specimens. *Journal of Geophysical Research: Solid Earth*, *121*, 15–26. https://doi.org/10.1002/2015JB012441

Besnus, M. J., & Meyer, A. J. (1964). *Nouvelles données expérimentales sur le magnétisme de la pyrrhotine naturelle* (pp. 507–511). Paper presented at Proceedings of the International Conference on Magnetism, Nottingham, England.

Bezaeva, N. S., Demory, F., Rochette, P., Sadykov, R. A., Gattacceca, J., Gabriel, T., & Quesnel, Y. (2015). The effect of hydrostatic pressure up to 1.61 GPa on the Morin transition of hematite-bearing rocks: Implications for planetary crustal magnetization. *Geophysical Research Letters*, *42*, 10,188–10,196. https://doi.org/10.1002/2015GL066306

Bezaeva, N. S., Gattacceca, J., Rochette, P., Sadykov, R. A., & Trukhin, V. I. (2010). Demagnetization of terrestrial and extraterrestrial rocks under hydrostatic pressure up to 1.2 GPa. *Physics of the Earth and Planetary Interiors*, *179*(1–2), 7–20. https://doi.org/10.1016/j.pepi.2010.01.004

Bhargava, S. K., Garg, A., & Subasinghe, N. D. (2009). In situ high-temperature phase transformation studies on pyrite. *Fuel*, *88*(6), 988–993. https://doi.org/10.1016/j.fuel.2008.12.005

Bilardello, D., & Jackson, M. (2013). What do the Mumpsies do? *IRM Quarterly*, *23*(3), 11–15.

Billi, A. (2005). Grain size distribution and thickness of breccia and gouge zones from thin (<1 m) strike-slip fault cores in limestone. *Journal of Structural Geology*, *27*(10), 1823–1837. https://doi.org/10.1016/j.jsg.2005.05.013

Bizzarri, A. (2009). What does control earthquake ruptures and dynamic faulting? A review of different competing mechanisms. *Pure and Applied Geophysics*, *166*(5–7), 741–776. https://doi.org/10.1007/s00024-009-0494-1

Bloemendal, J., King, J. W., Hall, F. R., & Doh, S. J. (1992). Rock magnetism of Late Neogene and Pleistocene deep-sea sediments: Relationship to sediment source, diagenetic processes and sediment lithology. *Journal of Geophysical Research*, *97*(B4), 4361–4375. https://doi.org/10.1029/91JB03068

Böhnel, H. N., Dekkers, M. J., Delgado-Argote, L. A., & Gratton, M. N. (2009). Comparison between the microwave and multispecimen parallel difference pTRM paleointensity methods. *Geophysical Journal International*, *177*(2), 383–394. https://doi.org/10.1111/j.1365-246X.2008.04036.x

Borradaile, G. J. (1988). Magnetic susceptibility, petrofabric and strain. *Tectonophysics*, *156*(1–2), 1–20. https://doi.org/10.1016/0040-1951(88)90279-X

Borradaile, G. J. (1996). Experimental stress remagnetization of magnetite. *Tectonophysics*, *261*(4), 229–248. https://doi.org/10.1016/0040-1951(95)00156-5

Borradaile, G. J., & Henry, B. (1997). Tectonic applications of magnetic susceptibility and its anisotropy. *Earth-Science Reviews*, *42*(1–2), 49–93. https://doi.org/10.1016/S0012-8252(96)00044-X

Borradaile, G. J., & Jackson, M. (2004). *Anisotropy of magnetic susceptibility (AMS): Magnetic petrofabrics of deformed rocks*, *Special Publications* (Vol. 238, pp. 299–360). London: Geological Society.

Borradaile, G. J., & Jackson, M. (2010). Structural geology, petrofabrics and magnetic fabrics (AMS, AARM, AIRM). *Journal of Structural Geology*, *32*(10), 1519–1551. https://doi.org/10.1016/j.jsg.2009.09.006

Borradaile, G. J., & Lagroix, F. (2000). Thermal enhancement of magnetic fabrics in high grade gneisses. *Geophysical Research Letters*, *27*(16), 2413–2416. https://doi.org/10.1029/2000GL008522

Boullier, A.-M. (2011). Fault-zone geology: lessons from drilling through the Nojima and Chelungpu faults. *Geological Society, London, Special Publications*, *359*(1), 17–37. https://doi.org/10.1144/SP359.2

Boullier, A.-M., Yeh, E.-C., Boutareaud, S., Song, S.-R., & Tsai, C.-H. (2009). Microscale anatomy of the 1999 Chi-Chi earthquake fault zone. *Geochemistry, Geophysics, Geosystems*, *10*, Q03016. https://doi.org/10.1029/2008GC002252

Boulton, C., Yao, L., Faulkner, D. R., Townend, J., Toy, V. G., Sutherland, R., et al. (2017). High-velocity frictional properties of Alpine Fault rocks: Mechanical data, microstructural analysis, and implications for rupture propagation. *Journal of Structural Geology*, *97*, 71–92. https://doi.org/10.1016/j.jsg.2017.02.003

Bradbury, K. K., Davis, C. R., Shervais, J. W., Janecke, S. U., & Evans, J. P. (2015). Composition, alteration, and texture of fault-related rocks from SAFOD core and surface outcrop analogs: Evidence for deformation processes and fluid-rock interactions. *Pure and Applied Geophysics*, *172*(5), 1053–1078. https://doi.org/10.1007/s00024-014-0896-6

Brantut, N., Schubnel, A., Rouzaud, J.-N., Brunet, F., & Shimamoto, T. (2008). High velocity frictional properties of a clay-bearing fault gouge and implications for earthquake mechanics. *Journal of Geophysical Research*, *113*, B10401. https://doi.org/10.1029/2007JB005551

Brodie, K., Fettes, D., & Harte, B. (2007). Structural terms including fault rock terms. In D. Fettes, & J. Desmonds (Eds.), *Metamorphic rocks: A classification and glossary of terms* (pp. 24–31). Cambridge, UK: Cambridge University Press.

Brodsky, E., Ma, K.-F., Mori, J. J., Saffer, D. M., & the participants of the ICDP/SCEC International Workshop (2009). Rapid response fault drilling: Past, present and future. *Scientific Drilling*, *8*, 66–74. https://doi.org/10.2204/iodp.sd.8.11.2009

Brodsky, E. E., Mori, J. J., Anderson, L., Chester, F. M., Conin, M., Dunham, E. M., et al. (2020). The state of stress on the fault before, during, and after a major earthquake. *Annual Reviews in Earth and Planetary Science*, *48*(1), 49–74. https://doi.org/10.1146/annurev-earth-053018-060507

Burmeister, K. C., Harrison, M. J., Marshak, S., Ferré, E., Bannister, R. A., & Kodama, K. P. (2009). Comparison of Fry strain ellipse and AMS ellipsoid trends to tectonic fabric trends in very low-strain sandstone of the Appalachian fold-thrust belt. *Journal of Structural Geology*, *31*(9), 1028–1038. https://doi.org/10.1016/j.jsg.2009.03.010

Cai, Y., Pei, J., Wang, H., Sheng, M., & Si, J. (2019). Paleo-earthquakes revealed by rock magnetic evidence from the Anxian-Guanxian Fault, Sichuan Province, China. *Tectonophysics*, *752*, 68–80. https://doi.org/10.1016/j.tecto.2018.12.027

Caine, J. S., Bruhn, R. L., & Forster, C. B. (2010). Internal structure, fault rocks, and inferences regarding deformation, fluid flow, and mineralization in the seismogenic Stillwater normal fault, Dixie Valley, Nevada. *Journal of Structural Geology*, *32*(11), 1576–1589.

Caine, J. S., Evans, J. P., & Forster, C. B. (1996). Fault zone architecture and permeability structure. *Geology*, *24*(11), 1025–1028. https://doi.org/10.1130/0091-7613(1996)024<1025:FZAAPS>2.3.CO;2

Carpenter, B. M., Kitajima, H., Sutherland, R., Townend, J., Toy, V. G., & Saffer, D. M. (2014). Hydraulic and acoustic properties of the active Alpine Fault, New Zealand: Laboratory measurements on DFDP-1 drill core. *Earth and Planetary Science Letters*, *390*, 45–51. https://doi.org/10.1016/j.epsl.2013.12.023

Carpenter, B. M., Saffer, D. M., & Marone, C. (2015). Frictional properties of the active San Andreas Fault at SAFOD: Implications for fault strength and slip behavior. *Journal of Geophysical Research: Solid Earth*, *120*, 5273–5289. https://doi.org/10.1002/2015JB011963

Casas-Sainz, A. M., Gil-Imaz, A., Simón, J. L., Izquierdo-Llavall, E., Aldega, L., Román- Berdiel, T., et al. (2018). Strain indicators and magnetic fabric in intraplate fault zones: Case study of Daroca thrust, Iberian Chain, Spain. *Tectonophysics*, *730*, 29–47. https://doi.org/10.1016/j.tecto.2018.02.013

Cerchiari, A., Remitti, F., Mittempergher, S., Festa, A., Lugli, F., & Cipriani, A. (2020). Cyclical variations of fluid sources and stress state in a shallow megathrust zone mélange. *Journal of the Geological Society*, *177*(3), 647–659. https://doi.org/10.1144/jgs2019-072

Chang, L., Roberts, A. P., Rowan, C. J., Tang, Y., Pruner, P., Chen, Q., & Horng, C.-S. (2009). Low-temperature magnetic properties of greigite (Fe_3S_4). *Geochemistry, Geophysics, Geosystems*, *10*, Q01Y04. https://doi.org/10.1029/2008GC002276

Chen, J., Niemeijer, A., Yao, L., & Ma, S. (2017). Water vaporization promotes coseismic fluid pressurization and buffers temperature rise. *Geophysical Research Letters*, *44*, 2177–2185. https://doi.org/10.1002/2016GL071932

Chen, J., Yang, X., Ma, S., & Spiers, C. J. (2013). Mass removal and clay mineral dehydration/rehydration in carbonate-rich surface exposures of the 2008 Wenchuan Earthquake fault: Geochemical evidence and implications for fault zone evolution and coseismic slip. *Journal of Geophysical Research: Solid Earth*, *118*, 474–496. https://doi.org/10.1002/jgrb.50089

Chen, J., Yang, X., Ma, S., Yang, T., & Niemeijer, A. (2016). Hydraulic properties of samples retrieved from the Wenchuan earthquake Fault Scientific Drilling Project Hole-1 (WFSD-1) and the surface rupture zone: Implications for coseismic slip weakening and fault healing. *Geochemistry, Geophysics, Geosystems*, *17*, 2717–2744. https://doi.org/10.1002/2016GC006376

Chen, T., Xu, H., Xie, Q., Chen, J., Ji, J., & Lu, H. (2005). Characteristics and genesis of maghemite in Chinese loess and paleosols: Mechanism for magnetic susceptibility enhancement in paleosols. *Earth and Planetary Science Letters*, *240*(3–4), 790–802. https://doi.org/10.1016/j.epsl.2005.09.026

Chester, F. M., Evans, J. P., & Biegel, R. L. (1993). Internal structure and weakening mechanisms of the San Andreas Fault. *Journal of Geophysical Research*, *98*(B1), 771–786. https://doi.org/10.1029/92JB01866

Cho, H., Kim, J.-S., Kim, K.-K., Kang, M.-H., Sohn, Y. K., Lee, Y. S., et al. (2015). Determination of rock cleavages using AMS (anisotropy of magnetic susceptibility): A case study on the Geochang granite stone, Korea [in Korean with English abstract]. *The Journal of the Petrological Society of Korea*, *24*(3), 209–231. https://doi.org/10.7854/JPSK.2015.24.3.209

Cho, H., Son, M., Sohn, Y. K., & Park, M. E. (2017). Magnetic fabric (anisotropy of magnetic susceptibility) constraints on emplacement mechanism of clastic dikes. *Journal of Geophysical Research: Solid Earth*, *122*, 3306–3333. https://doi.org/10.1002/2016JB013583

Choi, J.-H., Edwards, P., Ko, K., & Kim, Y.-S. (2016). Definition and classification of fault damage zones: A review and a new methodological approach. *Earth-Science Reviews*, *152*, 70–87. https://doi.org/10.1016/j.earscirev.2015.11.006

Chou, Y.-M., Song, S.-R., Aubourg, C., Lee, T.-Q., Boullier, A.-M., Song, Y.-F., et al. (2012). An earthquake slip zone is a magnetic recorder. *Geology*, *40*(6), 551–554. https://doi.org/10.1130/G32864.1

Chou, Y.-M., Song, S.-R., Aubourg, C., Lee, T.-Q., Song, Y.-F., & Yeh, E.-C. (2014). Quantitative modeling of the newly formed magnetic minerals in the fault gouge of 1999 Chi-Chi earthquake (M_w 7.6), Taiwan. *Journal of Geophysical Research: Solid Earth*, *119*, 6771–6781. https://doi.org/10.1002/2014JB011098

Chou, Y.-M., Song, S.-R., Aubourg, C., Song, Y.-F., Boullier, A.-M., Lee, T.-Q., et al. (2012). Pyrite alteration and neoformed magnetic minerals in the fault zone of the Chi-Chi earthquake (M_w 7.6, 1999): Evidence for frictional heating and co-seismic fluids. *Geochemistry, Geophysics, Geosystems*, *13*, Q08002. https://doi.org/10.1029/2012GC004120

Chou, Y.-M., Song, S.-R., Lee, T.-Q., Aubourg, C., & Yeh, E.-C. (2014). *Magnetic fabric analysis of Chelungpu fault gouge in Taiwan and its implications* (Abstract T11B-4552). Paper presented at American Geophysical Union Fall Meeting 2014, San Francisco, USA.

Chou, Y.-M., Song, S.-R., Tsao, T.-M., Lin, C.-S., Wang, M.-K., Lee, J.-J., & Chen, F.-J. (2014). Identification and tectonic implications of nano-particle quartz (~50 nm) by synchrotron X-ray diffraction in the Chelungpu fault gouge Taiwan. *Tectonophysics*, *619–620*, 36–43. https://doi.org/10.1016/j.tecto.2013.07.021

Cifelli, F., Mattei, M., Hirt, A. M., & Günther, A. (2004). The origin of tectonic fabrics in "undeformed" clays: The early stages of deformation in extensional sedimentary basins. *Geophysical Research Letters*, *31*, L09604. https://doi.org/10.1029/2004GL019609

Coffey, G. L., Savage, H. M., Polissar, P. J., Rowe, C. D., & Rabinowitz, H. S. (2019). Hot on the trail: Coseismic heating on a localized structure along the Muddy Mountain fault, Nevada. *Journal of Structural Geology*, *120*, 67–79. https://doi.org/10.1016/j.jsg.2018.12.012

Collettini, C., Di Stefano, G., Carpenter, B., Scarlato, P., Tesei, T., Mollo, S., et al. (2014). A novel and versatile apparatus for brittle rock deformation. *International Journal of Rock Mechanics and Mining Sciences*, *66*, 114–123. https://doi.org/10.1016/j.ijrmms.2013.12.005

Collombat, H., Rochette, P., & Vialon, P. (1995). Magnetic fabric as a strain indicator in unconsolidated sediments of the Chile Triple Junction area. In S. D. Lewis, J. H. Behrmann, R. J. Musgrave, S. C. Cande (Eds.), *Chile Triple Junction, Proceedings of the Ocean Drilling Program, Scientific Results* (Vol. 141, pp. 29–49). Ocean Drilling Program: College Station, TX.

Cornell, R. M., & Schwertmann, U. (2003). *The iron oxides: Structure, properties, reactions, occurrences and uses*. Weinheim, Germany: Wiley-VCH.

Cowan, D. S. (1999). Do faults preserve a record of seismic slip? A field geologist's opinion. *Journal of Structural Geology*, *21*(8–9), 995–1001. https://doi.org/10.1016/S0191-8141(99)00046-2

Criado, J. M., Gonzalez, M., & Macias, M. (1988). Influence of grinding on both the stability and thermal decomposition mechanism of siderite. *Thermochimica Acta*, *135*, 219–223. https://doi.org/10.1016/0040-6031(88)87389-1

D'Alessio, M. A., Blythe, A. E., & Bürgmann, R. (2003). No frictional heat along the San Gabriel fault, California: Evidence from fission-track thermochronology. *Geology*, *31*(6), 541–544. https://doi.org/10.1130/0091-7613(2003)031<0541:NFHATS>2.0.CO;2

Davidson, C., Davis, K. J., Bailey, C. M., Tape, C. H., Singleton, J., & Singer, B. (2003). Age, origin, and significance of brittle faulting and pseudotachylyte along the coast shear zone, Prince Rupert, British Columbia. *Geology*, *31*(1), 43–46. https://doi.org/10.1130/0091-7613(2003)031<0043:AOASOB>2.0.CO;2

Day, R., Fuller, M., & Schmidt, V. A. (1977). Hysteresis properties of titanomagnetites: Grain-size and compositional dependence. *Physics of the Earth and Planetary Interiors*, *13*(4), 260–267. https://doi.org/10.1016/0031-9201(77)90108-X

de Wall, H. (2000). The field-dependence of AC susceptibility in titanomagnetites: Implications for the anisotropy of magnetic susceptibility. *Geophysical Research Letters*, *27*(16), 2409–2411. https://doi.org/10.1029/2000GL008515

Dekkers, M. J. (1988). Magnetic properties of natural pyrrhotite, Part 1: Behaviour of initial susceptibility and saturation-magnetization related rock magnetic parameters in a grain-size dependent framework. *Physics of the Earth and Planetary Interiors*, *52*(3–4), 376–393. https://doi.org/10.1016/0031-9201(88)90129-X

Dekkers, M. J. (1990). Magnetic properties of natural goethite. Part III. Magnetic behaviour and properties of minerals originating from goethite dehydration during thermal demagnetization. *Geophysical Journal International*, *103*(1), 233–250. https://doi.org/10.1111/j.1365-246X.1990.tb01765.x

Dekkers, M. J. (1997). Environmental magnetism: An introduction. *Geologie en Mijnbouw*, *76*(1/2), 163–182. https://doi.org/10.1023/A:1003122305503

Dekkers, M. J., Mattéi, J.-L., Fillion, G., & Rochette, P. (1989). Grain-size dependence of the magnetic behavior of pyrrhotite during its low-temperature transition at 34 K. *Geophysical Research Letters*, *16*(8), 855–858. https://doi.org/10.1029/GL016i008p00855

Dekkers, M. J., Passier, H. F., & Schoonen, M. A. A. (2000). Magnetic properties of hydrothermally synthesized greigite (Fe_3S_4)-II. High- and low-temperature characteristics. *Geophysical Journal International*, *141*(3), 809–819. https://doi.org/10.1046/j.1365-246x.2000.00129.x

Derr, J. S. (1973). Earthquake lights: A review of observations and present theories. *Bulletin of the Seismological Society of America*, *63*, 2177–2187.

Di Toro, G., Han, R., Hirose, T., De Paola, N., Nielsen, S., Mizoguchi, K., et al. (2011). Fault lubrication during earthquakes. *Nature*, *471*(7339), 494–498. https://doi.org/10.1038/nature09838

Di Toro, G., Niemeijer, A., Tripoli, A., Nielsen, S., Di Felice, F., Scarlato, P., et al. (2010). From field geology to earthquake simulation: A new state-of-The-art tool to investigate rock friction during the seismic cycle (SHIVA). *Rendiconti Lincei*, *21*(S1), 95–114. https://doi.org/10.1007/s12210-010-0097-x

Di Toro, G., Pennacchioni, G., & Nielsen, S. (2009). Pseudotachylytes and earthquake source mechanics. In E. Fukuyama (Ed.), *Fault-zone properties and earthquake rupture dynamics* (pp. 87–134). Amsterdam: Elsevier.

Dubey, A. K. (2014). Anisotropy of magnetic susceptibility. In *Understanding an orogenic belt* (pp. 17–34). Cham, Switzerland: Springer.

Dunlop, D. J. (2002a). Theory and application of the Day plot (M_{rs}/M_s versus H_{cr}/H_c): 1. Theoretical curves and tests using titanomagnetite data. *Journal of Geophysical Research*, *107*(B3), 2056. https://doi.org/10.1029/2001JB000486

Dunlop, D. J. (2002b). Theory and application of the Day plot (M_{rs}/M_s versus H_{cr}/H_c): 2. Application to data for rocks, sediments, and soils. *Journal of Geophysical Research*, *107*(B3), 2057. https://doi.org/10.1029/2001JB000487

Dunlop, D. J., & Özdemir, Ö. (1997). *Rock magnetism: Fundamentals and frontiers*. Cambridge, UK: Cambridge University Press.

Dyar, M. D., Agresti, D. G., Schaefer, M. W., Grant, C. A., & Sklute, E. C. (2006). Mössbauer spectroscopy of Earth and planetary materials. *Annual Review of Earth and Planetary Sciences*, *34*(1), 83–125. https://doi.org/10.1146/annurev.earth.34.031405.125049

Egli, R. (2004a). Characterization of individual rock magnetic components by analysis of remanence curves: 1. Unmixing natural sediments. *Studia Geophysica et Geodaetica*, *48*(2), 391–446. https://doi.org/10.1023/B:SGEG.0000020839.45304.6d

Egli, R. (2004b). Characterization of individual rock magnetic components by analysis of remanence curves: 2. Fundamental properties of coercivity distributions. *Physics and Chemistry of the Earth*, *29*, 851–867. https://doi.org/10.1016/j.pce.2004.04.001

Egli, R. (2004c). Characterization of individual rock magnetic components by analysis of remanence curves: 3. Bacterial magnetite and natural processes in lakes. *Physics and Chemistry of the Earth*, *29*(13–14), 869–884. https://doi.org/10.1016/j.pce.2004.03.010

Egli, R. (2013). VARIFORC: An optimized protocol for calculating non-regular first-order reversal curve (FORC) diagrams. *Global and Planetary Change*, *110*(2013), 302–320. https://doi.org/10.1016/j.gloplacha.2013.08.003

Elhanati, D., Levi, T., Marco, S., & Weinberger, R. (2020). Zones of inelastic deformation around surface ruptures detected by magnetic fabrics. *Tectonophysics*, *788*, 228502. https://doi.org/10.1016/j.tecto.2020.228502

Enomoto, Y., Asuke, F., Zheng, Z., & Ishigaki, H. (2001). Hardened foliated fault gouge from the Nojima Fault zone at Hirabayashi: Evidence for earthquake lightning accompanying the 1995 Kobe earthquake? *Island Arc*, *10*(3–4), 447–456. https://doi.org/10.1046/j.1440-1738.2001.00343.x

Enomoto, Y., Yamabe, T., & Okumura, N. (2017). Causal mechanisms of seismo-EM phenomena during the 1965–1967 Matsushiro earthquake swarm. *Scientific Reports*, *7*, 44774. https://doi.org/10.1038/srep44774

Enomoto, Y., & Zheng, Z. (1998). Possible evidences of earthquake lightning accompanying the 1995 Kobe earthquake inferred from the Nojima fault gouge. *Geophysical Research Letters*, *25*(14), 2721–2724. https://doi.org/10.1029/98GL02015

Essene, E. J., & Fisher, D. C. (1986). Lightning strike fusion: Extreme reduction and metal-silicate liquid immiscibility. *Science*, *234*(4773), 189–193. https://doi.org/10.1126/science.234.4773.189

Evans, J. P., & Chester, F. M. (1995). Fluid-rock interaction in faults of the San-Andreas system-inferences from San-Gabriel fault rock geochemistry and microstructures. *Journal of Geophysical Research*, *100*(B7), 13,007–13,020. https://doi.org/10.1029/94JB02625

Evans, J. P., Prante, M. R., Janecke, S. U., Ault, A. K., & Newell, D. L. (2014). Hot faults: Iridescent slip surfaces with metallic luster document high-temperature ancient seismicity in the Wasatch fault zone, Utah, USA. *Geology*, *42*(7), 623–626. https://doi.org/10.1130/G35617.1

Evans, M. E., & Heller, F. (2003). *Environmental magnetism: Principles and applications of enviromagnetics*. San Diego, California: Academic.

Faulkner, D. R., Jackson, C. A. L., Lunn, R. J., Schlische, R. W., Shipton, Z. K., Wibberley, C. A. J., & Withjack, M. O. (2010). A review of recent developments concerning the structure, mechanics and fluid flow properties of fault zones. *Journal of Structural Geology*, *32*(11), 1557–1575. https://doi.org/10.1016/j.jsg.2010.06.009

Ferré, E. C., Chou, Y.-M., Kuo, R.-L., Yeh, E.-C., Leibovitz, N. R., Meado, A. L., et al. (2016). Deciphering viscous flow of frictional melts with the mini-AMS method. *Journal of Structural Geology*, *90*, 15–26. https://doi.org/10.1016/j.jsg.2016.07.002

Ferré, E. C., Gébelin, A., Till, J. L., Sassier, C., & Burmeister, K. (2014). Deformation and magnetic fabrics in ductile shear zones: A review. *Tectonophysics*, *629*, 179–188. https://doi.org/10.1016/j.tecto.2014.04.008

Ferré, E. C., Geissman, J. W., Chauvet, A., Vauchez, A., & Zechmeister, M. S. (2015). Focal mechanism of prehistoric earthquakes deduced from pseudotachylyte fabric. *Geology*, *43*(6), 531–534. https://doi.org/10.1130/G36587.1

Ferré, E. C., Geissman, J. W., Demory, F., Gattacceca, J., Zechmeister, M. S., & Hill, M. J. (2014). Coseismic magnetization of fault pseudotachylytes: 1. Thermal demagnetization experiments. *Journal of Geophysical Research: Solid Earth*, *119*, 6113–6135. https://doi.org/10.1002/2014JB011168

Ferré, E. C., Geissman, J. W., & Zechmeister, M. S. (2012). Magnetic properties of fault pseudotachylytes in granites. *Journal of Geophysical Research*, *117*, B01106. https://doi.org/10.1029/2011JB008762

Ferré, E. C., Martín-Hernández, F., Teyssier, C., & Jackson, M. (2004). Paramagnetic and ferromagnetic anisotropy of magnetic susceptibility in migmatites: Measurements in high and low fields and kinematic implications. *Geophysical Journal International*, *157*(3), 1119–1129. https://doi.org/10.1111/j.1365-246X.2004.02294.x

Ferré, E. C., Meado, A. L., Geissman, J. W., Di Toro, G., Spagnuolo, E., Ueda, T., et al. (2017). Earthquakes in the mantle? Insights from rock magnetism of pseudotachylytes. *Journal of Geophysical Research: Solid Earth*, *122*, 8769–8785. https://doi.org/10.1002/2017JB014618

Ferré, E. C., Zechmeister, M. S., Geissman, J. W., MathanaSekaran, N., & Kocak, K. (2005). The origin of high magnetic remanence in fault pseudotachylites: Theoretical considerations and implication for coseismic electrical currents. *Tectonophysics*, *402*(1–4), 125–139. https://doi.org/10.1016/j.tecto.2005.01.008

Fidani, C. (2010). The earthquake lights (EQL) of the 6 April 2009 Aquila earthquake, in Central Italy. *Natural Hazards and Earth System Sciences*, *10*(5), 967–978. https://doi.org/10.5194/nhess-10-967-2010

Flinn, D. (1965). On the symmetry principle and the deformation ellipsoid. *Geological Magazine*, *102*(1), 36–45. https://doi.org/10.1017/S0016756800053851

Fondriest, M., Smith, S. A. F., Candela, T., Nielsen, S. B., Mair, K., & Di Toro, G. (2013). Mirror-like faults and power dissipation during earthquakes. *Geology*, *41*(11), 1175–1178. https://doi.org/10.1130/G34641.1

Fossen, H., & Cavalcante, G. C. G. (2017). Shear zones-A review. *Earth-Science Reviews*, *174*, 434–455. https://doi.org/10.1016/j.earscirev.2017.05.002

Fossen, H., & Rotevatn, A. (2016). Fault linkage and relay structures in extensional settings—A review. *Earth-Science Reviews*, *154*, 14–28. https://doi.org/10.1016/j.earscirev.2015.11.014

Franke, C., Frederichs, T., & Dekkers, M. J. (2007). Efficiency of heavy liquid separation to concentrate magnetic particles. *Geophysical Journal International*, *170*(3), 1053–1066. https://doi.org/10.1111/j.1365-246X.2007.03489.x

Frederichs, T., von Dobeneck, T., Bleil, U., & Dekkers, M. J. (2003). Towards the identification of siderite, rhodochrosite and vivianite in sediments by their low-temperature magnetic properties. *Physics and Chemistry of the Earth*, *28*(16–19), 669–679. https://doi.org/10.1016/S1474-7065(03)00121-9

Freund, F., da Silva, M. A. S., Lau, B. W. S., Takeuchi, A., & Jone, H. H. (2007). Electric currents along earthquake faults and the magnetization of pseudotachylyte veins. *Tectonophysics*, *431*(1–4), 131–141. https://doi.org/10.1016/j.tecto.2006.05.039

Fu, R. R., Weiss, B. P., Lima, E. A., Kehayias, P., Araujo, J. F. D. F., Glenn, D. R., et al. (2017). Evaluating the paleomagnetic potential of single zircon crystals using the Bishop Tuff. *Earth and Planetary Science Letters*, *458*, 1–13. https://doi.org/10.1016/j.epsl.2016.09.038

Fukuchi, T. (2003). Strong ferrimagnetic resonance signal and magnetic susceptibility of the Nojima pseudotachylyte in Japan and their implication for coseismic electromagnetic changes. *Journal of Geophysical Research*, *108*(B6), 2312. https://doi.org/10.1029/2002JB002007

Fukuchi, T., Mizoguchi, K., & Shimamoto, T. (2005). Ferrimagnetic resonance signal produced by frictional heating: A new indicator of paleoseismicity. *Journal of Geophysical Research*, *110*, B12404. https://doi.org/10.1029/2004JB003485

Fukuchi, T., Tanaka, D., Imai, N., Soh, W., & Song, S.-R. (2009). *Thermal analyses of black zones in the Taiwan Chelungpu fault drilling project Hole B cores using ESR and VSM* (Abstract J172-013). Paper presented at Japan Geoscience Union Meeting 2009, Chiba, Japan.

Fukuchi, T., Yurugi, J., & Imai, N. (2007). ESR detection of seismic frictional heating events in the Nojima fault drill core samples, Japan. *Tectonophysics*, *443*(3–4), 127–138. https://doi.org/10.1016/j.tecto.2007.01.020

Fukuzawa, T., Nakamura, N., Oda, H., Uehara, M., & Nagahama, H. (2017). Generation of billow-like wavy folds by fluidization at high temperature in Nojima fault gouge: Microscopic and rock magnetic perspectives. *Earth, Planets and Space*, *69*, 54. https://doi.org/10.1186/s40623-017-0638-y

Fulton, P. M., Brodsky, E. E., Kano, Y., Mori, J., Chester, F., Ishikawa, T., et al. (2013). Low coseismic friction on the Tohoku-Oki fault determined from temperature measurements. *Science*, *342*(6163), 1214–1217. https://doi.org/10.1126/science.1243641

Fusseis, F., Xiao, X., Schrank, C., & De Carlo, F. (2014). A brief guide to synchrotron radiation-based microtomography in (structural) geology and rock mechanics. *Journal of Structural Geology*, *65*, 1–16. https://doi.org/10.1016/j.jsg.2014.02.005

Gattacceca, J., Lamali, A., Rochette, P., Boustie, M., & Berthe, L. (2007). The effects of explosive-driven shocks on the natural remanent magnetization and the magnetic properties of rocks. *Physics of the Earth and Planetary Interiors*, *162*(1–2), 85–98. https://doi.org/10.1016/j.pepi.2007.03.006

Gattacceca, J., & Rochette, P. (2004). Toward a robust normalized magnetic paleointensity method applied to meteorites. *Earth and Planetary Science Letters*, *227*(3–4), 377–393. https://doi.org/10.1016/j.epsl.2004.09.013

Gehring, A. U., & Hofmeister, A. M. (1994). The transformation of lepidocrocite during heating: A magnetic and spectroscopic study. *Clays and Clay Minerals*, *42*, 409–415. https://doi.org/10.1346/CCMN.1994.0420405

Gendler, T. S., Shcherbakov, V. P., Dekkers, M. J., Gapeev, A. K., Gribov, S. K., & McClelland, E. (2005). The lepidocrocite-maghemite-haematite reaction chain—I. Acquisition of chemical remanent magnetization by maghemite, its magnetic properties and thermal stability. *Geophysical Journal International*, *160*(3), 815–832. https://doi.org/10.1111/j.1365-246X.2005.02550.x

Ghiorso, M. S., & Gualda, G. A. R. (2015). Chemical thermodynamics and the study of magmas. In H. Sigurdsson, B. F. Houghton, S. R. McNutt, H. Rymer, & J. Stix (Eds.), *Encyclopedia of volcanoes* (2nd ed., pp. 143–161). San Diego, CA: Academic Press.

Gilder, S. A., & Le Goff, M. (2008). Systematic pressure enhancement of titanomagnetite magnetization. *Geophysical Research Letters*, *35*, L10302. https://doi.org/10.1029/2008GL033325

Gilder, S. A., Le Goff, M., & Chervin, J.-C. (2006). Static stress demagnetization of single and multidomain magnetite with implications for meteorite impacts. *High Pressure Research*, *26*(4), 539–547. https://doi.org/10.1080/08957950601092085

Gilder, S. A., Le Goff, M., Chervin, J.-C., & Peyronneau, J. (2004). Magnetic properties of single and multi-domain magnetite under pressures from 0 to 6 GPa. *Geophysical Research Letters*, *31*, L10612. https://doi.org/10.1029/2004GL019844

Gilder, S. A., Pohl, J., & Eitel, M. (2018). Magnetic signatures of terrestrial meteorite impact craters: A summary. In H. Lühr, J. Wicht, S. A. Gilder, & M. Holschneider (Eds.), *Magnetic fields in the solar system* (pp. 357–382). Cham, Switzerland: Springer.

Glenn, D. R., Fu, R. R., Kehayias, P., Le Sage, D., Lima, E. A., Weiss, B. P., & Walsworth, R. L. (2017). Micrometer-scale magnetic imaging of geological samples using a quantum diamond microscope. *Geochemistry, Geophysics, Geosystems*, *18*, 3254–3267. https://doi.org/10.1002/2017GC006946

Goddard, J. V., & Evans, J. P. (1995). Chemical changes and fluid-rock interaction in faults of crystalline thrust sheets, northwestern Wyoming, U.S.A. *Journal of Structural Geology*, *17*(4), 533–547. https://doi.org/10.1016/0191-8141(94)00068-B

Gong, Z., Van Hinsbergen, D. J. J., Vissers, R. L. M., & Dekkers, M. J. (2009). Early Cretaceous syn-rotational extension in the Organyà basin: New constraints on the palinspastic position of Iberia during its rotation. *Tectonophysics*, *473*(3–4), 312–323. https://doi.org/10.1016/j.tecto.2009.03.003

Graham, J. W. (1966). Significance of magnetic anisotropy in Appalachian sedimentary rocks. In J. S. Steinhart, & T. J. Smith (Eds.), *The Earth beneath the continents*, *Geophysical Monograph Series* (Vol. 10, pp. 627–648). Washington, DC: American Geophysics Union.

Gratier, J.-P., Dysthe, D. K., & Renard, F. (2013). The role of pressure solution creep in the ductility of the Earth's upper crust. *Advances in Geophysics*, *54*, 47–179. https://doi.org/10.1016/B978-0-12-380940-7.00002-0

Gray, M. B., Stamatakos, J. A., Ferrill, D. A., & Evans, M. A. (2005). Fault-zone deformation in welded tuffs at Yucca Mountain, Nevada, USA. *Journal of Structural Geology*, *27*(10), 1873–1891. https://doi.org/10.1016/j.jsg.2005.01.018

Grønlie, A., & Torsvik, T. H. (1989). On the origin and age of hydrothermal thorium enriched breccias in the Møre-Trøndelag Fault Zone, central Norway. *Norwegian Journal of Geology*, *69*, 1–19.

Grosz, S., Matthews, A., Ilani, S., Ayalon, A., & Garfunkel, Z. (2006). Iron mineralization and dolomitization in the Paran Fault zone, Israel: Implications for low-temperature basinal fluid processes near the Dead Sea Transform. *Geofluids*, *6*(2), 137–153. https://doi.org/10.1111/j.1468-8123.2006.00139.x

Grütter, P., Mamin, H. J., & Rugar, D. (1995). Magnetic force microscopy (MFM). In R. Wiesendanger & H. J. Güntherodt (Eds.), *Scanning tunneling microscopy II*, *Surface Sciences* (Vol. 28, pp. 151–207). Berlin, Heidelberg: Springer.

Gualtieri, A. F., & Venturelli, P. (1999). In situ study of the goethite-hematite phase transformation by real time synchrotron powder diffraction. *American Mineralogist*, *84*(5–6), 895–904. https://doi.org/10.2138/am-1999-5-624

Guichet, X., Jouniaux, L., & Catel, N. (2006). Modification of streaming potential by precipitation of calcite in a sand-water system: Laboratory measurements in the pH range from 4 to 12. *Geophysical Journal International*, *166*(1), 445–460. https://doi.org/10.1111/j.1365-246X.2006.02922.x

Guyodo, Y., LaPara, T. M., Anschutz, A. J., Penn, R. L., Banerjee, S. K., Geiss, C. E., & Zanner, W. (2006). Rock magnetic, chemical and bacterial community analysis of a modern soil from Nebraska. *Earth and Planetary Science Letters*, *251*(1–2), 168–178. https://doi.org/10.1016/j.epsl.2006.09.005

Hailwood, E. A., Maddock, R. H., Fung, T., & Rutter, E. H. (1992). Paleomagnetic analysis of fault gouge and dating fault movement, Anglesey, North Wales. *Journal of the Geological Society*, *149*(2), 273–284. https://doi.org/10.1144/gsjgs.149.2.0273

Han, R., Shimamoto, T., Ando, J., & Ree, J. H. (2007). Seismic slip record in carbonate-bearing fault zones: An insight from high-velocity friction experiments on siderite gouge. *Geology*, *35*(12), 1131–1134. https://doi.org/10.1130/G24106A.1

Harrison, R. J., & Feinberg, J. M. (2008). FORCinel: An improved algorithm for calculating first-order reversal curve distributions using locally weighted regression smoothing. *Geochemistry, Geophysics, Geosystems*, *9*, Q05016. https://doi.org/10.1029/2008GC001987

Hashimoto, Y., & Kaji, U. (2012). Rock-fluid interaction along seismogenic faults inferred from clay minerals in Okitsu melange, the Cretaceous Shimanto Belt, SW Japan. In S. D'Amico (Ed.), *Earthquake research and analysis—Seismology, seismotectonic and earthquake geology* (pp. 253–270). Rijeka, Croatia: InTech.

Hattori, I., & Yamamoto, H. (1999). Rock fragmentation and particle size in crushed zones by faulting. *The Journal of Geology*, *107*(2), 209–222. https://doi.org/10.1086/314343

Hausegger, S., Kurz, W., Rabitsch, R., Kiechl, E., & Brosch, F.-J. (2010). Analysis of the internal structure of a carbonate damage zone: Implications for the mechanisms of fault breccia formation and fluid flow. *Journal of Structural Geology*, *32*(9), 1349–1362. https://doi.org/10.1016/j.jsg.2009.04.014

Hayman, N. W., Housen, B. A., Cladouhos, T. T., & Livi, K. (2004). Magnetic and clast fabrics as measurements of grain-scale processes within the Death Valley shallow crustal detachment faults. *Journal of Geophysical Research*, *109*, B05409. https://doi.org/10.1029/2003JB002902

Hayman, N. W., & Lavier, L. L. (2014). The geological record of deep episodic tremor and slip. *Geology*, *42*(3), 195–198. https://doi.org/10.1130/G34990.1

Henderson, I. H. C., Ganerød, G. V., & Braathen, A. (2010). The relationship between particle characteristics and frictional strength in basal fault breccias: Implications for fault-rock evolution and rockslide susceptibility. *Tectonophysics*, *486*(1–4), 132–149. https://doi.org/10.1016/j.tecto.2010.02.002

Heraud, J. A., & Lira, J. A. (2011). Co-seismic luminescence in Lima, 150 km from the epicenter of the Pisco, Peru earthquake of 15 August 2007. *Natural Hazards and Earth System Sciences*, *11*(4), 1025–1036. https://doi.org/10.5194/nhess-11-1025-2011

Heslop, D. (2009). On the statistical analysis of the rock magnetic S-ratio. *Geophysical Journal International*, *178*(1), 159–161. https://doi.org/10.1111/j.1365-246X.2009.04175.x

Heslop, D., & Dillon, M. (2006). Unmixing magnetic remanence curves without a priori knowledge. *Geophysical Journal International*, *170*(2), 556–566. https://doi.org/10.1111/j.1365-246X.2007.03432.x

Hickman, S., Sibson, R., & Bruhn, R. (1995). Introduction to special section: Mechanical involvement of fluids in faulting. *Journal of Geophysical Research*, *100*(B7), 12,831–12,840. https://doi.org/10.1029/95JB01121

Hirono, T., Ikehara, M., Otsuki, K., Mishima, T., Sakaguchi, M., Soh, W., et al. (2006). Evidence of frictional melting within disk-shaped black materials discovered from the Taiwan Chelungpu fault system. *Geophysical Research Letters*, *33*, L19311. https://doi.org/10.1029/2006GL027329

Hirono, T., Ishikawa, T., Masumoto, H., Kameda, J., Yabuta, H., & Mukoyoshi, H. (2014). Re-evaluation of frictional heat recorded in the dark gouge of the shallow part of a megasplay fault at the Nankai Trough. *Tectonophysics*, *626*, 157–169. https://doi.org/10.1016/j.tecto.2014.04.020

Hirono, T., Lin, W., Yeh, E. C., Soh, W., Hashimoto, Y., Sone, H., et al. (2006). High magnetic susceptibility of fault gouge within Taiwan Chelungpu fault: Nondestructive continuous measurements of physical and chemical properties in fault rocks recovered from Hole B, TCDP. *Geophysical Research Letters*, *33*, L15303. https://doi.org/10.1029/2006GL026133

Hirono, T., Maekawa, Y., & Yabuta, H. (2015). Investigation of the records of earthquake slip in carbonaceous materials from the Taiwan Chelungpu fault by means of infrared and Raman spectroscopies. *Geochemistry, Geophysics, Geosystems*, *16*, 1233–1253.

Hirono, T., Ujiie, K., Ishikawa, T., Mishima, T., Hamada, Y., Tanimizu, M., et al. (2009). Estimation of temperature rise in a shallow slip zone of the megasplay fault in the Nankai Trough. *Tectonophysics*, *478*(3–4), 215–220. https://doi.org/10.1016/j.tecto.2009.08.001

Hirono, T., Yeh, E.-C., Lin, W., Sone, H., Mishima, T., Soh, W., et al. (2007). Nondestructive continuous physical property measurements of core samples recovered from Hole B, Taiwan Chelungpu-fault Drilling Project. *Journal of Geophysical Research*, *112*, B07404. https://doi.org/10.1029/2006JB004738

Hirt, A. M. (2007). Magnetic remanence, anisotropy. In D. Gubbins, & E. Herrero-Bervera (Eds.), *Encyclopedia of geomagnetism and paleomagnetism* (pp. 535–540). New York: Springer.

Hirt, A. M., Banin, A., & Gehring, A. U. (1993). Thermal generation of ferromagnetic minerals from iron-enriched smectites. *Geophysical Journal International*, *115*(3), 1161–1168. https://doi.org/10.1111/j.1365-246X.1993.tb01518.x

Hounslow, M. W. (1990). Grain fabric measured using magnetic susceptibility anisotropy in deformed sediments of the Barbados accretionary prism: Leg 110. In J. C. Moore et al. (Eds.), *Proceedings of the Ocean Drilling Program*, *Scientific Results* (Vol. 110, pp. 257–275). Ocean Drilling Program: College Station, TX.

Housen, B. A., Banerjee, S. K., & Moskowitz, B. M. (1996). Low-temperature magnetic properties of siderite and magnetite in marine sediments. *Geophysical Research Letters*, *23*(20), 2843–2846. https://doi.org/10.1029/96GL01197

Housen, B. A., & Kanamatsu, T. (2003). Magnetic fabrics from the Costa Rica margin: Sediment deformation during the initial dewatering and underplating process. *Earth and Planetary Science Letters*, *206*(1–2), 215–228. https://doi.org/10.1016/S0012-821X(02)01076-2

Housen, B. A., Tobin, H. J., Labaume, P., Leitch, E. C., Maltman, A. J., & ODP Leg 156 Shipboard Science Party (1996). Strain decoupling across the decollement of the Barbados accretionary prism. *Geology*, *24*(2), 127–130. https://doi.org/10.1130/0091-7613(1996)024<0127:SDATDO>2.3.CO;2

Hrouda, F. (1982). Magnetic anisotropy of rocks and its application in geology and geophysics. *Geophysical Surveys*, *5*(1), 37–82. https://doi.org/10.1007/BF01450244

Hrouda, F. (2011). Anisotropy of magnetic susceptibility in variable low-fields: A review. In E. Petrovský, D. Ivers, T. Harinarayana, E. Herrero-Bervera (Eds.), *The Earth's Magnetic Interior* (pp. 281–292). Dordrecht, Netherlands: Springer.

Hrouda, F., Chadima, M., Ježek, J., & Pokorný, J. (2016). Anisotropy of out-of-phase magnetic susceptibility of rocks as a tool for direct determination of magnetic subfabrics of some minerals: An introductory study. *Geophysical Journal International*, *208*(1), 385–402. https://doi.org/10.1093/gji/ggw399

Hrouda, F., Chlupáčová, M., & Mrázová, Š. (2006). Low-field variation of magnetic susceptibility as a tool for magnetic mineralogy of rocks. *Physics of the Earth and Planetary Interiors*, *154*(3–4), 323–336. https://doi.org/10.1016/j.pepi.2005.09.013

Hrouda, F., & Jelínek, V. (1990). Resolution of ferrimagnetic and paramagnetic anisotropies in rocks, using combined low-field and high-field measurements. *Geophysical Journal International*, *103*(1), 75–84. https://doi.org/10.1111/j.1365-246X.1990.tb01753.x

Hrouda, F., & Ježek, J. (2014). Frequency-dependent AMS of rocks: A tool for the investigation of the fabric of ultrafine magnetic particles. *Tectonophysics*, *629*, 27–38. https://doi.org/10.1016/j.tecto.2014.01.040

Hrouda, F., Müller, P., & Hanák, J. (2003). Repeated progressive heating in susceptibility vs. temperature investigation: A new palaeotemperature indicator? *Physics and Chemistry of the Earth*, *28*(16–19), 653–657.

Hu, H.-P., Chen, Q., Yin, Z., Zhang, P., Zou, J., & Che, H. (2002). Study on the kinetics of the thermal decomposition of mechanically activated pyrite. *Thermochimica Acta*, *389*(1–2), 79–83. https://doi.org/10.1016/S0040-6031(01)00850-4

Hu, P. X., Zhao, X., Roberts, A. P., Heslop, D., & Viscarra Rossel, R. A. (2018). Magnetic domain state diagnosis in soils, loess, and marine sediments from multiple first-order reversal curve-type diagrams. *Journal of Geophysical Research: Solid Earth*, *123*, 998–1017. https://doi.org/10.1002/2017JB015195

Huang, W., Dupont-Nivet, G., Lippert, P. C., Van Hinsbergen, D. J. J., Dekkers, M. J., Guo, Z., et al. (2015). Can a primary remanence be retrieved from partially remagnetized Eocence volcanic rocks in the Nanmulin Basin (southern Tibet) to date the India-Asia collision? *Journal of Geophysical Research: Solid Earth*, *120*, 42–66. https://doi.org/10.1002/2014JB011599

Humbert, F., Robion, P., Louis, L., Bartier, D., Ledésert, B., & Song, S.-R. (2012). Magnetic inference of in situ open microcracks in sandstone samples from the Taiwan Chelungpu Fault Drilling Project (TCDP). *Journal of Asian Earth Sciences*, *45*, 179–189. https://doi.org/10.1016/j.jseaes.2011.10.009

Hunt, C. P., Moskowitz, B. M., & Banerjee, S. K. (1995). Magnetic properties of rocks and minerals. In T. J. Ahrens (Ed.), *Rock physics and phase relations: A handbook of physical constants* (pp. 189–204). Washington, DC: American Geophysical Union.

Isaacs, A. J., Evans, J. P., Song, S.-R., & Kolesar, P. T. (2007). Structural, mineralogical, and geochemical characterization of the Chelungpu thrust fault, Taiwan. *Terrestrial, Atmospheric and Oceanic Sciences*, *18*(2), 183–221. https://doi.org/10.3319/TAO.2007.18.2.183(TCDP)

Ishikawa, T., Tanimizu, M., Nagaishi, K., Matsuoka, J., Tadai, O., Sakaguchi, M., et al. (2008). Coseismic fluid-rock interactions at high temperatures in the Chelungpu fault. *Nature Geoscience*, *1*(10), 679–683. https://doi.org/10.1038/ngeo308

Issachar, R., Levi, T., Lyakhovsky, V., Marco, S., & Weinberger, R. (2016). Improving the method of low-temperature anisotropy of magnetic susceptibility (LT-AMS) measurements in air. *Geochemistry, Geophysics, Geosystems*, *17*, 2940–2950. https://doi.org/10.1002/2016GC006339

Issachar, R., Levi, T., Marco, S., & Weinberger, R. (2018). Separation of diamagnetic and paramagnetic fabrics reveals strain directions in carbonate rocks. *Journal of Geophysical Research: Solid Earth*, *123*, 2035–2048. https://doi.org/10.1002/2017JB014823

Jackson, M. (1991). Anisotropy of magnetic remanence: A brief review of mineralogical sources, physical origins, and geological applications, and comparison with susceptibility anisotropy. *Pure and Applied Geophysics*, *136*(1), 1–28. https://doi.org/10.1007/BF00878885

Jackson, M., Borradaile, G., Hudleston, P., & Banerjee, S. (1993). Experimental deformation of synthetic magnetite-bearing calcite sandstones: Effects on remanence, bulk magnetic properties, and magnetic anisotropy. *Journal of Geophysical Research*, *98*(B1), 383–401. https://doi.org/10.1029/92JB01028

Jackson, M. J., Banerjee, S. K., Marvin, J. A., Lu, R., & Gruber, W. (1991). Detrital remanence, inclination errors, and anhysteretic remanence anisotropy: Quantitative model and experimental results. *Geophysical Journal International*, *104*(1), 95–103.

Jackson, M., Moskowitz, B., Rosenbaum, J., & Kissel, C. (1998). Field-dependence of AC susceptibility in titanomagnetites. *Earth and Planetary Science Letters*, *157*(3–4), 129–139. https://doi.org/10.1016/S0012-821X(98)00032-6

Jackson, M., & Solheid, P. (2010). On the quantitative analysis and evaluation of magnetic hysteresis data. *Geochemistry, Geophysics, Geosystems*, *11*, Q04Z15. https://doi.org/10.1029/2009GC002932

Jayangondaperumal, R., Dubey, A. K., Senthil Kumar, B., Wesnousky, S. G., & Sangode, S. J. (2010). Magnetic fabrics indicating Late Quaternary seismicity in the Himalayan foothills. *International Journal of Earth Sciences*, *99*(S1), 265–278. https://doi.org/10.1007/s00531-009-0494-5

Jelínek, V. (1981). Characterization of the magnetic fabric of rocks. *Tectonophysics*, *79*(3–4), T63–T67. https://doi.org/10.1016/0040-1951(81)90110-4

Jiang, Z., Rochette, P., Liu, Q., Gattacceca, J., Yu, Y., Barrón, V., & Torrent, J. (2013). Pressure demagnetization of synthetic Al substituted hematite and its implications for planetary studies. *Physics of the Earth and Planetary Interiors*, *224*, 1–10. https://doi.org/10.1016/j.pepi.2013.09.005

Jordanova, N., Jordanova, D., Kostadinova-Avramova, M., Lesigyarski, D., Nikolov, V., Katsarov, G., & Bacvarov, K. (2018). A mineral magnetic approach to determine paleo-firing temperatures in the Neolithic settlement site of Mursalevo-Deveboaz (SW Bulgaria). *Journal of Geophysical Research: Solid Earth*, *123*, 2522–2538. https://doi.org/10.1002/2017JB015190

Just, J., Dekkers, M. J., Von Dobeneck, T., Van Hoesel, A., & Bickert, T. (2012). Signatures and significance of aeolian, fluvial, bacterial and diagenetic magnetic mineral fractions in late quaternary marine sediments off Gambia, NW Africa. *Geochemistry, Geophysics, Geosystems*, *13*, Q0AO02. https://doi.org/10.1029/2012GC004146

Just, J., & Kontny, A. (2012). Thermally induced alterations of minerals during measurements of the temperature dependence of magnetic susceptibility: A case study from the hydrothermally altered Soultz-sous-Forêts granite, France. *International Journal of Earth Sciences*, *101*(3), 819–839. https://doi.org/10.1007/s00531-011-0668-9

Just, J., Kontny, A., de Wall, H., Hirt, A. M., & Martín-Hernández, F. (2004). *Development of magnetic fabrics during hydrothermal alteration in the Soultz-sous-Forets granite from the EPS-1 borehole, Upper Rhine Graben*, *Special Publications* (Vol. 238, pp. 509–526). London: Geological Society. https://doi.org/10.1144/GSL.SP.2004.238.01.26

Kamogawa, M., Ofuruton, H., & Ohtsuki, Y.-H. (2005). Earthquake light: 1995 Kobe earthquake in Japan. *Atmospheric Research*, *76*(1–4), 438–444. https://doi.org/10.1016/j.atmosres.2004.11.018

Kanamori, H., & Heaton, T. H. (2000). *Microscopic and macroscopic physics of earthquakes*, *Geophysical Monograph* (Vol. 120, pp. 147–163). Washington, DC: American Geophysical Union.

Kano, Y., Mori, J., Fujio, R., Ito, H., Yanagidani, T., Nakao, S., & Ma, K.-F. (2006). Heat signature on the Chelungpu fault associated with the 1999 Chi-Chi, Taiwan earthquake. *Geophysical Research Letters*, *33*, L14306. https://doi.org/10.1029/2006GL026733

Kapička, A. (1988). Anisotropy of magnetic susceptibility in a weak magnetic field induced by stress. *Physics of the Earth and Planetary Interiors*, *51*(4), 349–354. https://doi.org/10.1016/0031-9201(88)90075-1

Kapička, A. (1992). Magnetic susceptibility under hydrostatic pressure of synthetic magnetite samples. *Physics of the Earth and Planetary Interiors*, *70*(3–4), 248–252. https://doi.org/10.1016/0031-9201(92)90191-W

Kapička, A., Hrouda, F., Petrovský, E., & Poláčekc, J. (2006). Effect of plastic deformation in laboratory conditions on magnetic anisotropy of sedimentary rocks. *High Pressure Research*, *26*(4), 549–553. https://doi.org/10.1080/08957950601092390

Kars, M., Aubourg, C., & Pozzi, J.-P. (2011). Low temperature magnetic behaviour near 35 K in unmetamorphosed claystones. *Geophysical Journal International*, *186*(3), 1029–1035. https://doi.org/10.1111/j.1365-246X.2011.05121.x

Kawamoto, E., & Shimamoto, T. (1997). Mechanical behavior of halite and calcite shear zones from brittle to fully-plastic deformation and a revised fault model. In Y. Zheng, G. A. Davis, A. Yin (Eds.), *Structural geology and geomechanics: Proceedings of the 30th International Geological Congress* (Vol. 14, pp. 89–105). Utrecht, Netherlands: VSP International Science Publishers.

Kean, W., Day, R., Fuller, M., & Schmidt, V. (1976). The effect of uniaxial compression on the initial susceptibility of rocks as a function of grain size and composition of their constituent titanomagnetites. *Journal of Geophysical Research*, *81*(5), 861–872. https://doi.org/10.1029/JB081i005p00861

Kelso, P. R., Tikoff, B., Jackson, M., & Sun, W. (2002). A new method for the separation of paramagnetic and ferromagnetic susceptibility anisotropy using low field and high field methods. *Geophysical Journal International*, *151*(2), 345–359. https://doi.org/10.1046/j.1365-246X.2002.01732.x

Kerrich, R., Allison, I., Barnett, R. L., Moss, S., & Starkey, J. (1980). Microstructural and chemical transformations accompanying deformation of granite in a shear zone at Miéville, Switzerland; with implications for stress corrosion cracking and superplastic flow. *Contributions to Mineralogy and Petrology*, *73*(3), 221–242. https://doi.org/10.1007/BF00381442

King, J., Banerjee, S. K., & Marvin, J. (1982). A comparison of different magnetic methods for determining the relative grain size of magnetite in natural materials: Some results from lake sediments. *Earth and Planetary Science Letters*, *59*(2), 404–419. https://doi.org/10.1016/0012-821X(82)90142-X

Kirschvink, J. L. (1980). The least-squares line and plane and the analysis of palaeomagnetic data. *Geophysical Journal of the Royal Astronomical Society*, *62*(3), 699–718. https://doi.org/10.1111/j.1365-246X.1980.tb02601.x

Kodama, K. P., & Dekkers, M. J. (2004). Magnetic anisotropy as an aid to identifying CRM and DRM in red sedimentary rocks. *Studia Geophysica et Geodaetica*, *48*(4), 747–766. https://doi.org/10.1023/B:SGEG.0000045481.47203.33

Kontny, A., De Wall, H., Sharp, T. G., & Posfai, M. (2000). Mineralogy and magnetic behavior of pyrrhotite from a 260°C section at the KTB drilling site, Germany. *American Mineralogist*, *85*(10), 1416–1427. https://doi.org/10.2138/am-2000-1010

Kopp, R. E., & Humayun, M. (2003). Kinetic model of carbonate dissolution in Martian meteorite ALH84001. *Geochimica et Cosmochimica Acta*, *67*(17), 3247–3256. https://doi.org/10.1016/S0016-7037(02)01114-6

Koziol, A. M. (2004). Experimental determination of siderite stability and application to Martian Meteorite ALH84001. *American Mineralogist*, *89*(2–3), 294–300. https://doi.org/10.2138/am-2004-2-306

Kruiver, P. P., Dekkers, M. J., & Heslop, D. (2001). Quantification of magnetic coercivity components by the analysis of acquisition curves of isothermal remanent magnetisation. *Earth and Planetary Science Letters*, *189*(3–4), 269–276. https://doi.org/10.1016/S0012-821X(01)00367-3

Kuo, C. L., Huba, J. D., Joyce, G., & Lee, L. C. (2011). Ionosphere plasma bubbles and density variations induced by pre--earthquake rock currents and associated surface charges. *Journal of Geophysical Research*, *116*, A10317. https://doi.org/10.1029/2011JA016628

Kuo, L.-W., Li, H., Smith, S. A. F., Di Toro, G., Suppe, J., Song, S.-R., et al. (2014). Gouge graphitization and dynamic fault weakening during the 2008 *Mw* 7.9 Wenchuan earthquake. *Geology*, *42*(1), 47–50. https://doi.org/10.1130/G34862.1

Kuo, L.-W., Song, S.-R., Huang, L., Yeh, E.-C., & Chen, H.-F. (2011). Temperature estimates of coseismic heating in clay-rich fault gouges, the Chelungpu fault zones, Taiwan. *Tectonophysics*, *502*(3–4), 315–327. https://doi.org/10.1016/j.tecto.2011.02.001

Lakshmi, B. V., Gawali, P. B., Deenadayalan, K., & Ramesh, D. S. (2017). Rock magnetic and anisotropy of magnetic susceptibility (AMS) of earthquake affected soft sediments: Examples from Shillong and Latur (Deccan Trap), India. *Geophysical Research Abstracts*, *19*, EGU2017-11760.

Lanci, L., & Kent, D. V. (2003). Introduction of thermal activation in forward modeling of hysteresis loops for single-domain magnetic particles and implications for the interpretation of the Day diagram. *Journal of Geophysical Research*, *108*(B3), 2142. https://doi.org/10.1029/2001JB000944

Lascu, I., Harrison, R. J., Li, Y. T., Muraszko, J. R., Channell, J. E. T., Piotrowski, A. M., & Hodell, D. A. (2015). Magnetic unmixing of first-order reversal curve diagrams using principal component analysis. *Geochemistry, Geophysics, Geosystems*, *16*, 2900–2915. https://doi.org/10.1002/2015GC005909

Lavina, B., Dera, P., & Downs, R. T. (2014). Modern X-ray diffraction methods in mineralogy and geosciences. *Reviews in Mineralogy and Geochemistry*, *78*(1), 1–31. https://doi.org/10.2138/rmg.2014.78.1

Leibovitz, N. R. (2016). *Magnetic paleointensities in fault pseudotachylytes and implications for earthquake lightnings* (Master's thesis). Carbondale, USA: Southern Illinois University. Retrieved from ProQuest.

Levi, T., Weinberger, R., Aïfa, T., Eyal, Y., & Marco, S. (2006a). Earthquake-induced clastic dikes detected by anisotropy of magnetic susceptibility. *Geology*, *34*(2), 69–72. https://doi.org/10.1130/G22001.1

Levi, T., Weinberger, R., Aïfa, T., Eyal, Y., & Marco, S. (2006b). Injection mechanism of clay-rich sediments into dikes during earthquakes. *Geochemistry, Geophysics, Geosystems*, *7*, Q12009. https://doi.org/10.1029/2006GC001410

Levi, T., Weinberger, R., Alsop, G. I., & Marco, S. (2018). Characterizing seismites with anisotropy of magnetic susceptibility. *Geology*, *46*(9), 827–830. https://doi.org/10.1130/G45120.1

Levi, T., Weinberger, R., & Marco, S. (2014). Magnetic fabrics induced by dynamic faulting reveal damage zone sizes in soft rocks, Dead Sea basin. *Geophysical Journal International*, *199*(2), 1214–1229. https://doi.org/10.1093/gji/ggu300

Li, H., Xue, L., Brodsky, E. E., Mori, J. J., Fulton, P. M., Wang, H., et al. (2015). Long-term temperature records following the *Mw* 7.9 Wenchuan (China) earthquake consistent with low friction. *Geology*, *43*(2), 163–166. https://doi.org/10.1130/G35515.1

Li, W.-H., Lee, C.-H., Ma, M.-H., Huang, P. J., & Wu, S. Y. (2019). Fault Dynamics of the 1999 Chi-Chi earthquake: Clues from nanometric geochemical analysis of fault gouges. *Scientific Reports*, *9*, 5683. https://doi.org/10.1038/s41598-019-42028-w

Lima, E. A., Bruno, A. C., Carvalho, H. R., & Weiss, B. P. (2014). Scanning magnetic tunnel junction microscope for high-resolution imaging of remanent magnetization fields. *Measurement Science and Technology*, *25*(10), 105401. https://doi.org/10.1088/0957-0233/25/10/105401

Lin, A. (2008). *Fossil earthquakes: The formation and preservation of pseudotachylytes*. Berlin: Springer.

Lin, A., Maruyama, T., Aaron, S., Michibayashi, K., Camacho, A., & Kano, K. (2005). Propagation of seismic slip from brittle to ductile crust: Evidence from pseudotachylyte of the Woodroffe thrust, central Australia. *Tectonophysics*, *402*(1–4), 21–35. https://doi.org/10.1016/j.tecto.2004.10.016

Lin, W., Conin, M., Moore, J. C., Chester, F. M., Nakamura, Y., Mori, J. J., et al. (2013). Stress state in the largest displacement area of the 2011 Tohokuoki Earthquake. *Science*, *339*(6120), 687–690. https://doi.org/10.1126/science.1229379

Liu, D., Li, H., Lee, T.-Q., Chou, Y.-M., Song, S.-R., Sun, Z., et al. (2014). Primary rock magnetism for the Wenchuan earthquake fault zone at Jiulong outcrop, Sichuan Province, China. *Tectonophysics*, *619–620*, 58–69. https://doi.org/10.1016/j.tecto.2013.08.028

Liu, D., Li, H., Lee, T.-Q., Sun, Z., Liu, J., Han, L., & Chevalier, M.-L. (2016). Magnetic mineral characterization close to the Yingxiu-Beichuan fault surface rupture zone of the Wenchuan earthquake (*Mw* 7.9, 2008) and its implication for earthquake slip processes. *Journal of Asian Earth Sciences*, *115*, 468–479. https://doi.org/10.1016/j.jseaes.2015.10.019

Liu, J. Y., Chen, Y. I., Huang, C. H., Ho, Y. Y., & Chen, C. H. (2015). A statistical study of lightning activities and $M \geq 5.0$ earthquakes in Taiwan during 1993–2004. *Surveys in Geophysics*, *36*(6), 851–859. https://doi.org/10.1007/s10712-015-9342-2

Liu, Q. S., Deng, C. L., Yu, Y., Torrent, J., Jackson, M. J., Banerjee, S. K., & Zhu, R. X. (2005). Temperature dependence of magnetic susceptibility in an argon environment: Implications for pedogenesis of Chinese loess/palaeosols. *Geophysical Journal International*, *161*(1), 102–112. https://doi.org/10.1111/j.1365-246X.2005.02564.x

Liu, Q. S., Roberts, A. P., Larrasoaña, J. C., Banerjee, S. K., Guyodo, Y., Tauxe, L., & Oldfield, F. (2012). Environmental magnetism: Principles and applications. *Reviews of Geophysics*, *50*, RG4002. https://doi.org/10.1029/2012RG000393

Liu, Q. S., Yu, Y. J., Torrent, J., Roberts, A. P., Pan, Y. X., & Zhu, R. X. (2006). Characteristic low-temperature magnetic properties of aluminous goethite [α-(Fe, Al)OOH] explained. *Journal of Geophysical Research*, *111*, B12S34. https://doi.org/10.1029/2006JB004560

Lockner, D. A., Johnston, M. J. S., & Byerlee, J. D. (1983). A mechanism to explain the generation of earthquake lights. *Nature*, *302*(5903), 28–33. https://doi.org/10.1038/302028a0

Losseva, T. V., & Nemchinov, I. V. (2005). Earthquake lights and rupture processes. *Natural Hazards and Earth System Sciences*, *5*(5), 649–656. https://doi.org/10.5194/nhess-5-649-2005

Louis, L., Chen, T.-M. N., David, C., Robion, P., Wong, T.-F., & Song, S.-R. (2008). Anisotropy of magnetic susceptibility and *P*-wave velocity in core samples from the Taiwan Chelungpu-Fault Drilling Project (TCDP). *Journal of Structural Geology*, *30*(8), 948–962. https://doi.org/10.1016/j.jsg.2008.03.006

Louzada, K. L., Stewart, S. T., Weiss, B., Gattacceca, J., & Bezaeva, N. S. (2010). Shock and static pressure demagnetization of pyrrhotite and implications for the Martian crust. *Earth and Planetary Science Letters*, *290*(1–2), 90–101. https://doi.org/10.1016/j.epsl.2009.12.006

Louzada, K. L., Stewart, S. T., Weiss, B., Gattacceca, J., Lillis, R. J., & Halekas, J. S. (2011). Impact demagnetization of the Martian crust: Current knowledge and future directions. *Earth and Planetary Science Letters*, *305*(3–4), 257–269. https://doi.org/10.1016/j.epsl.2011.03.013

Lowrie, W. (1990). Identification of ferromagnetic minerals in a rock by coercivity and unblocking temperature properties. *Geophysical Research Letters*, *17*(2), 159–162. https://doi.org/10.1029/GL017i002p00159

Ma, K.-F. (2009). Earthquake dynamics—From macroscopic to microscopic: Examples learnt from the 1999 Chi-Chi earthquake in Taiwan. *Physics*, *38*(7), 462–470.

Ma, S., Shimamoto, T., Yao, L., Togo, T., & Kitajima, H. (2014). A rotary-shear low to high-velocity friction apparatus in Beijing to study rock friction at plate to seismic slip rates. *Earthquake Science*, *27*(5), 469–497. https://doi.org/10.1007/s11589-014-0097-5

Maekawa, Y., Hirono, T., Yabuta, H., Mukoyoshi, H., Kitamura, M., Ikehara, M., et al. (2014). Estimation of slip parameters associated with frictional heating during the 1999 Taiwan Chi-Chi earthquake by vitrinite reflectance geothermometry. *Earth, Planets and Space*, *66*(1), 28. https://doi.org/10.1186/1880-5981-66-28

Maher, B. A., & Thompson, R. (1999). *Quaternary climates, Environments and magnetism*. Cambridge, UK: Cambridge University Press.

Mair, K., & Abe, S. (2008). 3D numerical simulations of fault gouge evolution during shear: Grain size reduction and strain localization. *Earth and Planetary Science Letters*, *274*(1–2), 72–81. https://doi.org/10.1016/j.epsl.2008.07.010

Marcén, M., Román-Berdiel, T., Casas-Sainz, A. M., Soto, R., Oliva-Urcia, B., & Castro, J. (2019). Strain variations in a seismogenic normal fault (Baza Sub-basin, Betic Chain): Insights from magnetic fabrics (AMS). *Tectonophysics*, *765*, 64–82. https://doi.org/10.1016/j.tecto.2019.05.014

Martín-Hernández, F., & Ferré, E. C. (2007). Separation of paramagnetic and ferrimagnetic anisotropies: A review. *Journal of Geophysical Research*, *112*, B03105. https://doi.org/10.1029/2006JB004340

Martín-Hernández, F., & Hirt, A. M. (2001). Separation of ferrimagnetic and paramagnetic anisotropies using a high-field torsion magnetometer. *Tectonphysics*, *337*(3–4), 209–221. https://doi.org/10.1016/S0040-1951(01)00116-0

Martín-Hernández, F., Lüneburg, C. M., Aubourg, C., & Jackson, M. (2004). *Magnetic fabric: Methods and applications—An introduction*, *Special Publications* (Vol. 238, pp. 1–7). London: Geological Society.

Matsuda, T., Omura, K., Ikeda, R., Arai, T., Kobayashi, K., Shimada, K., et al. (2004). Fracture-zone conditions on a recently active fault: Insights from mineralogical and geochemical analyses of the Hirabayashi NIED drill core on the Nojima fault, southwest Japan, which ruptured in the 1995 Kobe earthquake. *Tectonophysics*, *378*(3–4), 143–163. https://doi.org/10.1016/j.tecto.2003.09.005

Maxbauer, D. P., Feinberg, J. M., & Fox, D. L. (2016). MAX UnMix: A web application for unmixing magnetic coercivity distributions. *Computers & Geosciences*, *95*, 140–145. https://doi.org/10.1016/j.cageo.2016.07.009

McKenzie, D. P., & Brune, J. N. (1972). Melting on fault planes during large earthquakes. *Geophysical Journal of the Royal Astronomical Society*, *29*(1), 65–78. https://doi.org/10.1111/j.1365-246X.1972.tb06152.x

McLaren, A. C. (2005). *Transmission electron microscopy of minerals and rocks*. Cambridge, UK: Cambridge University Press.

Menegon, L., Pennacchioni, G., Malaspina, N., Harris, K., & Wood, E. (2017). Earthquakes as precursors of ductile shear zones in the dry and strong lower crust. *Geochemistry, Geophysics, Geosystems*, *18*, 4356–4374. https://doi.org/10.1002/2017GC007189

Miller, S. A. (2013). The role of fluids in tectonic and earthquake processes. *Advances in Geophysics*, *54*, 1–46. https://doi.org/10.1016/B978-0-12-380940-7.00001-9

Mishima, T., Hirono, T., Nakamura, N., Tanikawa, W., Soh, W., & Song, S.-R. (2009). Changes to magnetic minerals caused by frictional heating during the 1999 Taiwan Chi-Chi earthquake. *Earth, Planets and Space*, *61*(6), 797–801. https://doi.org/10.1186/BF03353185

Mishima, T., Hirono, T., Soh, W., & Song, S.-R. (2006). Thermal history estimation of the Taiwan Chelungpu fault using rock-magnetic methods. *Geophysical Research Letters*, *33*, L23311. https://doi.org/10.1029/2006GL028088

Moecher, D. P., & Steltenpohl, M. G. (2009). Direct calculation of rupture depth for an exhumed paleoseismogenic fault from mylonitic pseudotachylyte. *Geology*, *37*(11), 999–1002. https://doi.org/10.1130/G30166A.1

Molina-Garza, R. S., Geissman, J., Wawrzyniec, T., Weber, B., Martínez, M. L., & Aranda-Gómez, J. (2009). An integrated magnetic and geological study of cataclasite-dominated pseudotachylytes in the Chiapas Massif, Mexico: A snapshot of stress orientation following slip. *Geophysical Journal International*, *177*(3), 891–912. https://doi.org/10.1111/j.1365-246X.2009.04046.x

Morgan, J. K. (1999). Numerical simulations of granular shear zones using the distinct element method: 2. Effects of particle size distribution and interparticle friction on mechanical behavior. *Journal of Geophysical Research*, *104*(B2), 2721–2732. https://doi.org/10.1029/1998JB900055

Morgan, J. K., & Boettcher, M. S. (1999). Numerical simulations of granular shear zones using the distinct element method: 1. Shear zone kinematics and the micromechanics of localization. *Journal of Geophysical Research*, *104*(B2), 2703–2719. https://doi.org/10.1029/1998JB900056

Morin, F. J. (1950). Magnetic susceptibility of αFe_2O_3 and αFe_2O_3 with added titanium. *Physical Review*, *78*(6), 819–820. https://doi.org/10.1103/PhysRev.78.819.2

Moskowitz, B. M., Jackson, M., & Kissel, C. (1998). Low temperature magnetic behavior of titanomagnetites. *Earth and Planetary Science Letters*, *157*(3-4), 141–149. https://doi.org/10.1016/S0012-821X(98)00033-8

Muir-Wood, R. (1994). *Earthquakes, strain-cycling and the mobilization of fluids*, *Special Publications* (Vol. 78, pp. 85–98). London: Geological Society.

Mukhopadhyay, P. K. (1992). Maturation of organic matter as revealed by microscopicmethods: Applications and limitations of vitrinite reflectance, and continuous spectral and pulsed laser fluorescence spectroscopy. In K. H. Wolf & G. V. Chilingarian (Eds.), *Diagenesis, III: Developments in sedimentology* (Vol. 47, pp. 435–510). Amsterdam: Elsevier.

Mullender, T. A. T., van Velzen, A. J., & Dekkers, M. J. (1993). Continuous drift correction and separate identification of ferrimagnetic and paramagnetic contribution in thermomagnetic runs. *Geophysical Journal International*, *114*(3), 663–672. https://doi.org/10.1111/j.1365-246X.1993.tb06995.x

Murad, E., & Bowen, L. H. (1987). Magnetic ordering in Al-rich goethites: Influence of crystallinity. *American Mineralogist*, *72*, 194–200.

Nagata, T. (1961). *Rock magnetism*. Tokyo: Maruzen.

Nagata, T. (1966). Main characteristics of piezo-magnetization and their qualitative interpretation. *Journal of Geomagnetism and Geoelectricity*, *18*(1), 81–97. https://doi.org/10.5636/jgg.18.81

Nagata, T., & Carleton, B. J. (1969). Notes on piezo-remanent magnetization of igneous rocks II. *Journal of Geomagnetism and Geoelectricity*, *21*(1), 427–445. https://doi.org/10.5636/jgg.21.427

Nakamura, N., Hirose, T., & Borradaile, G. J. (2002). Laboratory verification of submicron magnetite production in pseudotachylytes: Relevance for paleointensity studies. *Earth and Planetary Science Letters*, *201*(1), 13–18. https://doi.org/10.1016/S0012-821X(02)00704-5

Nakamura, N., & Nagahama, H. (2001). Changes in magnetic and fractal properties of fractured granites near the Nojima fault, Japan. *Island Arc*, *10*(3–4), 486–494. https://doi.org/10.1046/j.1440-1738.2001.00347.x

Nielsen, S. (2017). From slow to fast faulting: Recent challenges in earthquake fault mechanics. *Philosophical Transactions of the Royal Society A - Mathematical Physical and Engineering Sciences*, *375*, 20160016. https://doi.org/10.1098/rsta.2016.0016

Niemeijer, A. R., Di Toro, G., Griffith, W. A., Bistacchi, A., Smith, S. A. F., & Nielsen, S. (2012). Inferring earthquake physics and chemistry using an integrated field and laboratory approach. *Journal of Structural Geology*, *39*, 2–36. https://doi.org/10.1016/j.jsg.2012.02.018

Niemeijer, A. R., & Vissers, R. L. M. (2014). Earthquake rupture propagation inferred from the spatial distribution of fault rock frictional properties. *Earth and Planetary Science Letters*, *396*, 154–164. https://doi.org/10.1016/j.epsl.2014.04.010

Niwa, M., Mizuochi, Y., & Tanase, A. (2015). Changes in chemical composition caused by water–rock interactions across a strike-slip fault zone: Case study of the Atera Fault, Central Japan. *Geofluids*, *15*(3), 387–409. https://doi.org/10.1111/gfl.12096

Nixon, C. W., Bull, J. M., & Sanderson, D. J. (2014). Localized vs distributed deformation associated with the linkage history of an active normal fault, Whakatane Graben, New Zealand. *Journal of Structural Geology*, *69*, 266–280. https://doi.org/10.1016/j.jsg.2014.06.005

Noguchi, A., Oda, H., Yamamoto, Y., Usui, A., Sato, M., & Kawai, J. (2017). Scanning SQUID microscopy of a ferromanganese crust from the northwestern Pacific: Submillimeter scale magnetostratigraphy as a new tool for age determination and mapping of environmental magnetic parameters. *Geophysical Research Letters*, *44*, 5360–5367. https://doi.org/10.1002/2017GL073201

O'Hara, K. D. (2001). A pseudotachylyte geothermometer. *Journal of Structural Geology*, *23*(9), 1345–1357. https://doi.org/10.1016/S0191-8141(01)00008-6

O'Hara, K. D., & Huggins, F. E. (2005). A Mössbauer study of pseudotachylytes: Redox conditions during seismogenic faulting. *Contributions to Mineralogy and Petrology*, *148*(5), 602–614. https://doi.org/10.1007/s00410-004-0622-y

Ohmoto, H. (2003). Nonredox transformations of magnetite-hematite in hydrothermal systems. *Economic Geology*, *98*(1), 157–161. https://doi.org/10.2113/gsecongeo.98.1.157

Oohashi, K., Hirose, T., & Shimamoto, T. (2011). Shear-induced graphitization of carbonaceous materials during seismic fault motion: Experiments and possible implications fault mechanics. *Journal of Structural Geology*, *33*(6), 1122–1134. https://doi.org/10.1016/j.jsg.2011.01.007

Oriolo, S., Wemmer, K., Oyhantçabal, P., Fossen, H., Schulz, B., & Siegesmund, S. (2018). Geochronology of shear zones—A review. *Earth-Science Reviews*, *185*, 665–683. https://doi.org/10.1016/j.earscirev.2018.07.007

Otsuki, K., Hirono, T., Omori, M., Sagaguchi, M., Tanigawa, W., Lin, W., et al. (2009). Analyses of pseudotachylyte from Hole-B of Taiwan Chelungpu Fault Drilling Project (TCDP); Their implications for seismic slip behaviors during the 1999 Chi-Chi earthquake. *Tectonophysics*, *469*(1–4), 13–24. https://doi.org/10.1016/j.tecto.2009.01.008

Owens, W. H. (1993). Magnetic fabric studies of samples from Hole 808C, Nankai Trough. In I. A. Hill, A. Taira, J. V. Firth (Eds.), *Proceedings of the Ocean Drilling Program*, *Scientific Results* (Vol. 131, pp. 301–310). Ocean Drilling Program: College Station, TX.

Özdemir, Ö., & Banerjee, S. K. (1984). High temperature stability of maghemite (γ-Fe_2O_3). *Geophysical Research Letters*, *11*(3), 161–164. https://doi.org/10.1029/GL011i003p00161

Özdemir, Ö., & Dunlop, D. J. (1997). Effect of crystal defects and internal stress on the domain structure and magnetic properties of magnetite. *Journal of Geophysical Research*, *102*(B9), 20,211–20,224. https://doi.org/10.1029/97JB01779

Özdemir, Ö., & Dunlop, D. J. (2000). Intermediate magnetite formation during dehydration of goethite. *Earth and Planetary Science Letters*, *177*(1–2), 59–67. https://doi.org/10.1016/S0012-821X(00)00032-7

Özdemir, Ö., Dunlop, D. J., & Berquó, T. S. (2008). Morin transition in hematite: Size dependence and thermal hysteresis. *Geochemistry, Geophysics, Geosystems*, *9*, Q10Z01. https://doi.org/10.1029/2008GC002110

Özdemir, Ö., Dunlop, D. J., & Moskowitz, B. M. (1993). The effect of oxidation on the Verwey transition in magnetite. *Geophysical Research Letters*, *20*(16), 1671–1674. https://doi.org/10.1029/93GL01483

Palmer, C. S., Ohly, S. R., Smith, R. W., Neupane, G., McLing, T., & Mattson, E. (2015). Mineral selection for multicomponent equilibrium geothermometry. *Transactions-Geothermal Resources Council*, *38*, 453–459.

Pan, Y., & Nilges, M. J. (2014). Electron paramagnetic resonance spectroscopy: Basic principles, experimental techniques and applications to Earth and planetary sciences. *Reviews in Mineralogy and Geochemistry*, *78*(1), 655–690. https://doi.org/10.2138/rmg.2014.78.16

Pan, Y. X., Zhu, R. X., Banerjee, S. K., Gill, J., & Williams, Q. (2000). Rock magnetic properties related to thermal treatment of siderite: Behavior and interpretation. *Journal of Geophysical Research*, *105*(B1), 783–794. https://doi.org/10.1029/1999JB900358

Parés, J. M. (2015). Sixty years of anisotropy of magnetic susceptibility in deformed sedimentary rocks. *Frontiers in Earth Science*, *3*, 1–13. https://doi.org/10.3389/feart.2015.00004

Parés, J. M., & van der Pluijm, B. A. (2014). Low-temperature AMS and the quantification of subfabrics in deformed rocks. *Tectonophysics*, *629*, 55–62. https://doi.org/10.1016/j.tecto.2014.03.005

Pastore, Z., Ter Maat, G., Church, N., McEnroe, S. A., Oda, H., & Fumagalli, P. (2018). Millimeter to micrometer scale mapping of serpentinized dunite by high resolution magnetic microscopy. *Lithos*, *323*, 174–190. https://doi.org/10.1016/j.lithos.2018.09.018

Pechersky, D. M., & Genshaft, Y. S. (2001). Petromagnetism of the continental lithosphere and the origin of regional magnetic anomalies: A review. *Russian Journal of Earth Sciences*, *3*(2), 97–124. https://doi.org/10.2205/2001ES000059

Pei, J. L., Li, H. B., Wang, H., Si, J. L., Sun, Z. M., & Zhou, Z. Z. (2014). Magnetic properties of the Wenchuan Earthquake Fault Scientific Drilling Project Hole-1 (WFSD-1), Sichuan Province, China. *Earth, Planets and Space*, *66*(1), 23. https://doi.org/10.1186/1880-5981-66-23

Pei, J. L., Zhou, Z. Z., Dong, S. G., & Tang, L. (2014). Magnetic evidence revealing frictional heating from fault rocks in granites. *Tectonophysics*, *637*, 207–217. https://doi.org/10.1016/j.tecto.2014.10.008

Pei, Y., Paton, D. A., Knipe, R. J., & Wu, K. (2015). A review of fault sealing behaviour and its evaluation in siliciclastic rocks. *Earth-Science Reviews*, *150*, 121–138. https://doi.org/10.1016/j.earscirev.2015.07.011

Peters, C., & Dekkers, M. J. (2003). Selected room temperature magnetic parameters as a function of mineralogy, concentration and grain size. *Physics and Chemistry of the Earth*, *28*(16–19), 659–667. https://doi.org/10.1016/S1474-7065(03)00120-7

Petri, B., Almqvist, B. S. G., & Pistone, M. (2020). 3D rock fabric analysis using micro-tomography: An introduction to the open-source TomoFab MATLAB code. *Computers & Geosciences*, *138*, 104444. https://doi.org/10.1016/j.cageo.2020.104444

Petrik, I., Nabelek, P. I., Janak, M., & Plasienka, D. (2003). Conditions of formation and crystallization kinetics of highly oxidized pseudotachylytes from the High Tatras (Slovakia). *Journal of Petrology*, *44*(5), 901–927. https://doi.org/10.1093/petrology/44.5.901

Petrovský, E., Alcalá, M. D., Criado, J. M., Grygar, T., Kapička, A., & Šubrt, J. (2000). Magnetic properties of magnetite prepared by ball-milling of hematite with iron. *Journal of Magnetism and Magnetic Materials*, *210*(1–3), 257–273. https://doi.org/10.1016/S0304-8853(99)00624-1

Petrovský, E., Kropáček, V., Dekkers, M. J., de Boer, C. B., Hoffman, V., & Ambatiello, A. (1996). Transformation of hematite to maghemite as observed by changes in magnetic parameters: Effects of mechanical activation? *Geophysical Research Letters*, *23*(12), 1477–1480. https://doi.org/10.1029/96GL01411

Philpotts, A. R. (1964). Origin of pseudotachylytes. *American Journal of Science*, *262*(8), 1008–1035. https://doi.org/10.2475/ajs.262.8.1008

Pittarello, L., Di Toro, G., Bizzarri, A., Pennacchioni, G., Hadizadeh, J., & Cocco, M. (2008). Energy partitioning during seismic slip in pseudotachylyte-bearing faults (Gole Larghe Fault, Adamello, Italy). *Earth and Planetary Science Letters*, *269*(1–2), 131–139. https://doi.org/10.1016/j.epsl.2008.01.052

Pittarello, L., Pennacchioni, G., & Di Toro, G. (2012). Amphibolite-facies pseudotachylytes in Premosello metagabbro and felsic mylonites (Ivrea Zone, Italy). *Tectonophysics*, *580*, 43–57. https://doi.org/10.1016/j.tecto.2012.08.001

Potter, D. K. (2004). *A comparison of anisotropy of magnetic remanence methods—A user's guide for application to palaeomagnetism and magnetic fabric studies*, *Special Publications* (Vol. 238, pp. 21–35). London: Geological Society. https://doi.org/10.1144/GSL.SP.2004.238.01.03

Pozzi, J. P. (1975). Magnetic properties of oceanic basalts—Effects of pressure and consequences for the interpretation of anomalies. *Earth and Planetary Science Letters*, *26*(3), 337–344. https://doi.org/10.1016/0012-821X(75)90009-6

Rabinowitz, H. S., Polissar, P. J., & Savage, H. M. (2017). Reaction kinetics of alkenone and n-alkane thermal alteration at seismic timescales. *Geochemistry, Geophysics, Geosystems*, *18*, 204–219. https://doi.org/10.1002/2016GC006553

Rabinowitz, H. S., Savage, H. M., Polissar, P. J., Rowe, C. D., & Kirkpatrick, J. D. (2020). Earthquake slip surfaces identified by biomarker thermal maturity within the 2011 Tohoku-Oki earthquake fault zone. *Nature Communications*, *11*, 533. https://doi.org/10.1038/s41467-020-14447-1

Reed, S. J. B. (2005). *Electron microprobe analysis and scanning electron microscopy in geology*. Cambridge, UK: Cambridge University Press.

Reverdatto, V. V., Likhanov, I. I., Polyansky, O. P., Sheplev, V. S., & Kolobov, V. Y. (2019). Mineral geothermobarometry. In *The nature and models of metamorphism* (pp. 55–82). Cham, Switzerland: Springer.

Reynolds, R. L., Tuttle, M. L., Rice, C. A., Fishman, N. S., Karachewski, J. A., & Sherman, D. W. (1994). Magnetization and geochemistry of greigite-bearing Cretaceous strata, North Slope Basin, Alaska. *American Journal of Science*, *294*(4), 485–528. https://doi.org/10.2475/ajs.294.4.485

Rice, J. R. (2006). Heating and weakening of faults during earthquake slip. *Journal of Geophysical Research*, *111*, B05311. https://doi.org/10.1029/2005JB004006

Roberts, A. P. (1995). Magnetic properties of sedimentary greigite (Fe_3S_4). *Earth and Planetary Science Letters*, *134*(3–4), 227–236. https://doi.org/10.1016/0012-821X(95)00131-U

Roberts, A. P., Almeida, T. P., Church, N. S., Harrison, R. J., Heslop, D., Li, Y., et al. (2017). Resolving the origin of pseudo-single domain magnetic behavior. *Journal of Geophysical Research: Solid Earth*, *122*, 9534–9558. https://doi.org/10.1002/2017JB014860

Roberts, A. P., Chang, L., Rowan, C. J., Horng, C. S., & Florindo, F. (2011). Magnetic properties of sedimentary greigite (Fe_3S_4): An update. *Reviews of Geophysics*, *49*, RG1002. https://doi.org/10.1029/2010RG000336

Roberts, A. P., Heslop, D., Zhao, X., & Pike, C. R. (2014). Understanding fine magnetic particle systems through use of first-order reversal curve diagrams. *Reviews of Geophysics*, *52*, 557–602. https://doi.org/10.1002/2014RG000462

Roberts, A. P., Liu, Q. S., Rowan, C. J., Chang, L., Carvallo, C., Torrent, J., et al. (2006). Characterization of hematite (α-Fe_2O_3), goethite (α-FeOOH), greigite (Fe_3S_4), and pyrrhotite (Fe_7S_8) using first-order reversal curve diagrams. *Journal of Geophysical Research*, *111*, B12S35. https://doi.org/10.1029/2006JB004715

Roberts, A. P., Pike, C. R., & Verosub, K. L. (2000). First-order reversal curve diagrams: A new tool for characterizing the magnetic properties of natural samples. *Journal of Geophysical Research*, *105*(B12), 28,461–28,475. https://doi.org/10.1029/2000JB900326

Roberts, A. P., Tauxe, L., Heslop, D., Zhao, X., & Jiang, Z. (2018). A critical appraisal of the "Day" diagram. *Journal of Geophysical Research: Solid Earth*, *123*, 2618–2644. https://doi.org/10.1002/2017JB015247

Rochette, P., Bezaeva, N. S., Kosterov, A., Gattacceca, J., Masaitis, V. L., Badyukov, D. D., et al. (2019). Magnetic properties and redox state of impact glasses: A review and new case studies from Siberia. *Geosciences*, *9*, 225. https://doi.org/10.3390/geosciences9050225

Rochette, P., & Fillion, G. (1988). Identification of multicomponent anisotropies in rocks using various field and temperature values in a cryogenic magnetometer. *Physics of the Earth and Planetary Interiors*, *51*(4), 379–386.
Rochette, P., & Fillion, G. (1989). Field and temperature behavior of remanence in synthetic goethite: Paleomagnetic implications. *Geophysical Research Letters*, *16*(8), 851–854. https://doi.org/10.1029/GL016i008p00851
Rochette, P., Fillion, G., & Dekkers, M. J. (2011). Interpretation of low-temperature data part 4: The low-temperature magnetic transition of monoclinic pyrrhotite. *IRM Quarterly*, *21*, 1–11.
Rochette, P., Fillion, G., Mattéi, J.-L., & Dekkers, M. J. (1990). Magnetic transition at 30–34 Kelvin in pyrrhotite: Insight into a widespread occurrence of this mineral in rocks. *Earth and Planetary Science Letters*, *98*(3–4), 319–328. https://doi.org/10.1016/0012-821X(90)90034-U
Rochette, P., Gattacceca, J., Devouard, B., Moustard, F., Bezaeva, N. S., Cournède, C., & Scaillet, B. (2015). Magnetic properties of tektites and other related impact glasses. *Earth and Planetary Science Letters*, *432*, 381–390. https://doi.org/10.1016/j.epsl.2015.10.030
Rochette, P., Jackson, M., & Aubourg, C. (1992). Rock magnetism and the interpretation of anisotropy of magnetic susceptibility. *Reviews of Geophysics*, *30*(3), 209–226. https://doi.org/10.1029/92RG00733
Román-Berdiel, T., Casas-Sainz, A. M., Oliva-Urcia, B., Calvín, P., & Villalaín, J. J. (2019). On the influence of magnetic mineralogy in the tectonic interpretation of anisotropy of magnetic susceptibility in cataclastic fault zones. *Geophysical Journal International*, *216*(2), 1043–1061. https://doi.org/10.1093/gji/ggy481
Rowe, C. D., Fagereng, Å., Miller, J. A., & Mapani, B. (2012). Signature of coseismic decarbonation in dolomitic fault rocks of the Naukluft Thrust, Namibia. *Earth and Planetary Science Letters*, *333–334*, 200–210. https://doi.org/10.1016/j.epsl.2012.04.030
Rowe, C. D., & Griffith, W. A. (2015). Do faults preserve a record of seismic slip: A second opinion. *Journal of Structural Geology*, *78*, 1–26. https://doi.org/10.1016/j.jsg.2015.06.006
Rowe, C. D., Kirkpatrick, J. D., & Brodsky, E. E. (2012). Fault rock injections record paleo-earthquakes. *Earth and Planetary Science Letters*, *335–336*, 154–166. https://doi.org/10.1016/j.epsl.2012.04.015
Rowe, C. D., Lamothe, K., Rempe, M., Andrews, M., Mitchell, T. M., Di Toro, G., et al. (2019). Earthquake lubrication and healing explained by amorphous nanosilica. *Nature Communications*, *10*, 320. https://doi.org/10.1038/s41467-018-08238-y
Sakaguchi, A., Chester, F., Curewitz, D., Fabbri, O., Goldsby, D., Kimura, G., et al. (2011). Seismic slip propagation to the updip end of plate boundary subduction interface faults: Vitrinite reflectance geothermometry on Integrated Ocean Drilling Program NanTro SEIZE cores. *Geology*, *39*(4), 395–398. https://doi.org/10.1130/G31642.1
Sammis, C. G., & Ben-Zion, Y. (2008). Mechanics of grain-size reduction in fault zones. *Journal of Geophysical Research*, *113*, B02306. https://doi.org/10.1029/2006JB004892
Sasai, Y. (2001). Tectonomagnetic modeling based on the piezomagnetism: A review. *Annals of Geophysics*, *44*(2), 361–368.
Sato, M., Makio, M., Hayashi, T., & Ohno, M. (2015). Abrupt intensification of North Atlantic deep water formation at the Nordic Seas during the late Pliocene climate transition. *Geophysical Research Letters*, *42*, 4949–4955. https://doi.org/10.1002/2015GL063307
Savage, H. M., Polissar, P. J., Sheppard, R., Rowe, C. D., & Brodsky, E. E. (2014). Biomarkers heat up during earthquakes: New evidence of seismic slip in the rock record. *Geology*, *42*(2), 99–102. https://doi.org/10.1130/G34901.1
Savage, H. M., Rabinowitz, H. S., Spagnuolo, E., Aretusini, S., Polissar, P. J., & Di Toro, G. (2018). Biomarker thermal maturity experiments at earthquake slip rates. *Earth and Planetary Science Letters*, *502*, 253–261.
Schabes, M. E., & Bertram, H. N. (1988). Magnetization processes in ferromagnetic cubes. *Journal of Applied Physics*, *64*(3), 1347–1357. https://doi.org/10.1063/1.341858
Schmid, S. M., & Handy, M. R. (1991). Towards a genetic classification of fault rocks: Geological usage and tectonophysical implications. In D. W. Müller, J. A. McKenzie, & H. Weissert (Eds.), *Controversies in modern geology: Evolution of geological theories in sedimentology, Earth history and tectonics* (pp. 339–361). London: Academic.
Schmidt, V., Hirt, A. M., Rosselli, P., & Martín-Hernández, F. (2007). Separation of diamagnetic and paramagnetic anisotropy by high-field, low-temperature torque measurements. *Geophysical Journal International*, *168*(1), 40–47. https://doi.org/10.1111/j.1365-246X.2006.03202.x
Scholz, C. H. (2019). *The mechanisms of earthquake faulting* (3rd ed.). New York: Cambridge University Press. https://doi.org/10.1017/9781316681473
Schwarz, E. J., & Vaughan, D. J. (1972). Magnetic phase relations of pyrrhotite. *Journal of Geomagnetics and Geoelectrics*, *24*(4), 441–458. https://doi.org/10.5636/jgg.24.441
Scuderi, M., & Collettini, C. (2016). The role of fluid pressure in induced vs. triggered seismicity: Insights from rock deformation experiments on carbonates. *Scientific Reports*, *6*, 24852. https://doi.org/10.1038/srep24852
Sibson, R. H. (1977). Fault rocks and fault mechanisms. *Journal of the Geological Society*, *133*(3), 191–213. https://doi.org/10.1144/gsjgs.133.3.0191
Sibson, R. H. (1986). Earthquakes and rock deformation in crustal fault zones. *Annual Review of Earth and Planetary Sciences*, *14*(1), 149–175. https://doi.org/10.1146/annurev.ea.14.050186.001053
Sibson, R. H. (1989). Earthquake faulting as a structural process. *Journal of Structural Geology*, *11*(1–2), 1–14. https://doi.org/10.1016/0191-8141(89)90032-1
Sibson, R. H. (1992). Implication of fault-valve behaviour for rupture nucleation and recurrence. *Tectonophysics*, *211*(1–4), 283–293. https://doi.org/10.1016/0040-1951(92)90065-E
Sibson, R. H. (2003). Thickness of the seismic slip zone. *Bulletin of the Seismological Society of America*, *93*(3), 1169–1178. https://doi.org/10.1785/0120020061
Sibson, R. H., & Toy, V. G. (2006). The habitat of fault-generated pseudotachylyte: Presence vs. absence of friction-melt. In R. Abercrombie, A. McGarr, H. Kanamori, G. Di Toro (Eds.), *Earthquakes: Radiated energy and the physics of faulting*, *Geophysical Monograph Series* (Vol. 170, pp. 153–166). Washington, DC: American Geophysical Union.
Siman-Tov, S., Aharonov, E., Sagy, A., & Emmanuel, S. (2013). Nanograins form carbonate fault mirrors. *Geology*, *41*(6), 703–706. https://doi.org/10.1130/G34087.1
Snoke, A. W., Tullis, J., & Todd, V. R. (1998). *Fault-related rocks: A photographic atlas*. Princeton, NJ: Princeton University Press.
Solum, J. G., & van der Pluijm, B. (2009). Quantification of fabrics in clay gouge from the Carboneras fault, Spain and implications for fault behavior. *Tectonophysics*, *475*(3–4), 554–562. https://doi.org/10.1016/j.tecto.2009.07.006
Spassov, S., & Hus, J. (2006). Estimating baking temperatures in a Roman pottery kiln by rock magnetic properties: Implications of thermochemical alteration on archaeointensity determinations. *Geophysical Journal International*, *167*(2), 592–604. https://doi.org/10.1111/j.1365-246X.2006.03114.x

Spray, J. G. (2010). Frictional melting processes in planetary materials: From hypervelocity impact to earthquakes. *Annual Review of Earth and Planetary Sciences*, *38*(1), 221–254. https://doi.org/10.1146/annurev.earth.031208.100045

Stacey, F. D., & Banerjee, D. K. (1974). *Physical principles of rock magnetism*. Amsterdam: Elsevier.

Stephenson, A., Sadikun, S., & Potter, D. K. (1986). A theoretical and experimental comparison of the anisotropies of magnetic susceptibility and remanence in rocks and minerals. *Geophysical Journal International*, *84*(1), 185–200. https://doi.org/10.1111/j.1365-246X.1986.tb04351.x

St-Laurent, F., Derr, J. S., & Freund, F. T. (2006). Earthquake lights and the stress-activation of positive hole charge carriers in rocks. *Physics and Chemistry of the Earth*, *31*(4–9), 305–312. https://doi.org/10.1016/j.pce.2006.02.003

Storti, F., Balsamo, F., & Salvini, F. (2007). Particle shape evolution in natural carbonate granular wear material. *Terra Nova*, *19*(5), 344–352. https://doi.org/10.1111/j.1365-3121.2007.00758.x

Sutherland, R., Toy, V. G., Townend, J., Cox, S. C., Eccles, J. D., Faulkner, D. R., et al. (2012). Drilling reveals fluid control on architecture and rupture of the Alpine fault, New Zealand. *Geology*, *40*(12), 1143–1146. https://doi.org/10.1130/G33614.1

Suttie, N., Shaw, J., & Hill, M. J. (2010). Direct demonstration of microwave demagnetization of a whole rock sample with minimal heating. *Earth and Planetary Science Letters*, *292*(3–4), 357–362. https://doi.org/10.1016/j.epsl.2010.02.002

Swan, A. R. H., & Sandilands, M. (1995). *Introduction to geological data analysis*. Oxford, UK: Blackwell Science.

Swanson, M. T. (1992). Fault structure, wear mechanisms and rupture processes in pseudotachylyte generation. *Tectonophysics*, *204*(3–4), 223–242. https://doi.org/10.1016/0040-1951(92)90309-T

Tanaka, H., Chen, W. M., Wang, C. Y., Ma, K. F., Urata, N., Mori, J., & Ando, M. (2006). Frictional heat from faulting of the 1999 Chi-Chi, Taiwan earthquake. *Geophysical Research Letters*, *33*, L16316. https://doi.org/10.1029/2006GL026673

Tanaka, H., Fujimoto, K., Ohtani, T., & Ito, H. (2001). Structural and chemical characterization of shear zones in the freshly activated Nojima fault, Awaji Island, southwest Japan. *Journal of Geophysical Research*, *106*(B5), 8789–8810. https://doi.org/10.1029/2000JB900444

Tanikawa, W., Ishikawa, T., Honda, G., Hirono, T., & Tadai, O. (2015). Trace element anomaly in fault rock induced by coseismic hydrothermal reactions reproduced in laboratory friction experiments. *Geophysical Research Letters*, *42*, 3210–3217. https://doi.org/10.1002/2015GL063195

Tanikawa, W., Mishima, T., Hirono, T., Lin, W., Shimamoto, T., Soh, W., & Song, S.-R. (2007). High magnetic susceptibility produced in high-velocity frictional tests on core samples from the Chelungpu fault in Taiwan. *Geophysical Research Letters*, *34*, L15304. https://doi.org/10.1029/2007GL030783

Tanikawa, W., Mishima, T., Hirono, T., Soh, W., & Song, S.-R. (2008). High magnetic susceptibility produced by thermal decomposition of core samples from the Chelungpu fault in Taiwan. *Earth and Planetary Science Letters*, *272*(1–2), 372–381. https://doi.org/10.1016/j.epsl.2008.05.002

Tarduno, J. A., Cottrell, R. D., Davis, W. J., Nimmo, F., & Bono, R. K. (2015). A Hadean to Paleoarchean geodynamo recorded by single zircon crystals. *Science*, *349*(6247), 521–524. https://doi.org/10.1126/science.aaa9114

Tarling, D. H., & Hrouda, F. (1993). *The magnetic anisotropy of rocks*. London, UK: Chapman & Hall.

Tauxe, L. (2010). *Essentials of paleomagnetism*. Berkeley: University of California Press.

Tauxe, L., Bertram, H. N., & Seberino, C. (2002). Physical interpretation of hysteresis loops: Micromagnetic modeling of fine particle magnetite. *Geochemistry, Geophysics, Geosystems*, *3*(10), 1055. https://doi.org/10.1029/2001GC000241

Terakawa, T., Zoporowski, A., Galvan, B., & Miller, S. A. (2010). High-pressure fluid at hypocentral depths in the L'Aquila region inferred from earthquake focal mechanisms. *Geology*, *38*(11), 995–998. https://doi.org/10.1130/G31457.1

Thériault, R., St-Laurent, F., Freund, F. T., & Derr, J. S. (2014). Prevalence of earthquake lights associated with rift environments. *Seismological Research Letters*, *85*(1), 159–178. https://doi.org/10.1785/0220130059

Thompson, R., & Oldfield, F. (1986). *Environmental magnetism*. London, UK: Allen and Unwin.

Till, J. L., & Moskowitz, B. M. (2014). Deformation microstructures and magnetite texture development in synthetic shear zones. *Tectonophysics*, *629*, 211–223. https://doi.org/10.1016/j.tecto.2014.04.026

Torii, M., Fukuma, K., Horng, C.-S., & Lee, T.-Q. (1996). Magnetic discrimination of pyrrhotite- and greigite-bearing sediment samples. *Geophysical Research Letters*, *23*(14), 1813–1816. https://doi.org/10.1029/96GL01626

Torrent, J., & Barrón, V. (2008). Diffuse reflectance spectroscopy. In L. R. Dress, & A. L. Ulery (Eds.), *Methods of soil analysis, Part 5. Mineralogical methods*, *SSSA Book Serial* (Vol. 5, pp. 367–387). Wisconsin: Soil Science Society of America.

Torsvik, T. H., Sturt, B. A., Swensson, E., Andersen, T. B., & Dewey, J. F. (1992). Palaeomagnetic dating of fault rocks: Evidence for Permian and Mesozoic movements and brittle deformation along the extensional Dalsfjord Fault, western Norway. *Geophysical Journal International*, *109*(3), 565–580. https://doi.org/10.1111/j.1365-246X.1992.tb00118.x

Toulmin, P., & Barton, P. B. (1964). A thermodynamic study of pyrite and pyrrhotite. *Geochimica et Cosmochimica Acta*, *28*(5), 641–671. https://doi.org/10.1016/0016-7037(64)90083-3

Townend, J., & Zoback, M. D. (2000). How faulting keeps the crust strong. *Geology*, *28*(5), 399–402. https://doi.org/10.1130/0091-7613(2000)28<399:HFKTCS>2.0.CO;2

Twiss, R. J., & Moores, E. M. (1992). *Structural geology*. New York: W. H. Freeman.

Ujiie, K., Hisamitsu, T., & Taira, A. (2003). Deformation and fluid pressure variation during initiation and evolution of the plate boundary décollement zone in the Nankai accretionary prism. *Journal of Geophysical Research*, *108*(B8), 2398. https://doi.org/10.1029/2002JB002314

Ujiie, K., & Kimura, G. (2014). Earthquake faulting in subduction zones: Insights from fault rocks in accretionary prisms. *Progress in Earth and Planetary Science*, *1*(1), 7–30. https://doi.org/10.1186/2197-4284-1-7

Ujiie, K., Tanaka, H., Saito, T., Tsutsumi, A., Mori, J. J., Kameda, J., et al. (2013). Low coseismic shear stress on the Tohoku-oki megathrust determined from laboratory experiments. *Science*, *342*(6163), 1211–1214. https://doi.org/10.1126/science.1243485

Van de Moortèle, B., Reynard, B., Rochette, P., Jackson, M., Beck, P., Gillet, P., et al. (2007). Shock-induced metallic iron nanoparticles in olivine-rich Martian meteorites. *Earth and Planetary Science Letters*, *262*(1–2), 37–49. https://doi.org/10.1016/j.epsl.2007.07.002

Verberne, B. A., Plümper, O., & Spiers, C. J. (2019). Nanocrystalline principal slip zones and their role in controlling crustal fault rheology. *Minerals*, *9*, 328. https://doi.org/10.3390/min9060328

Vermilye, J. M., & Scholz, C. H. (1998). The process zone: A microstructural view of fault growth. *Journal of Geophysical Research*, *103*(B6), 12,223–12,237. https://doi.org/10.1029/98JB00957

Verosub, K. L., & Roberts, A. P. (1995). Environmental magnetism: Past, present, and future. *Journal of Geophysical Research*, *100*(B2), 2175–2192. https://doi.org/10.1029/94JB02713

Verrier, V., & Rochette, P. (2002). Estimating peak currents at ground lightning impacts using remanent magnetization. *Geophysical Research Letters*, *29*(18), 1867. https://doi.org/10.1029/2002GL015207

Verwey, E. J. (1939). Electronic conduction of magnetite (Fe_3O_4) and its transition point at low temperature. *Nature*, *144*(3642), 327–328. https://doi.org/10.1038/144327b0

Viti, C. (2011). Exploring fault rocks at the nanoscale. *Journal of Structural Geology*, *33*(12), 1715–1727. https://doi.org/10.1016/j.jsg.2011.10.005

Volk, M. W. R., & Feinberg, J. M. (2019). Domain state and temperature dependence of pressure remanent magnetization in synthetic magnetite: Implications for crustal remagnetization. *Geochemistry, Geophysics, Geosystems*, *20*, 2473–2483. https://doi.org/10.1029/2019GC008238

Volk, M. W. R., & Gilder, S. A. (2016). Effect of static pressure on absolute paleointensity recording with implications for meteorites. *Journal of Geophysical Research: Solid Earth*, *121*, 5596–5610. https://doi.org/10.1002/2016JB013059

Walden, J., Oldfield, F., & Smith, J. (1999). *Environmental magnetism: A practical guide*, *Technical Guide* (Vol. 6). London: Quaternary Research Association.

Wang, H., Li, H., Si, J., Sun, Z., & Huang, Y. (2014). Internal structure of the Wenchuan earthquake fault zone, revealed by surface outcrop and WFSD-1 drilling core investigation. *Tectonophysics*, *619–620*, 101–114. https://doi.org/10.1016/j.tecto.2013.08.029

Weiss, B., Lima, E., Fong, L., & Baudenbacher, F. (2007). Paleomagnetic analysis using SQUID microscopy. *Journal of Geophysical Research*, *112*, B9105. https://doi.org/10.1029/2007JB004940

Weltje, G. J. (1997). End-member modeling of compositional data: Numerical-statistical algorithms for solving the explicit mixing problem. *Mathematical Geology*, *29*(4), 503–549. https://doi.org/10.1007/BF02775085

White, J. C. (1996). Transient discontinuities revisited: Pseudotachylyte, plastic instability and the influence of low pore fluid pressure on deformation processes in the mid-crust. *Journal of Structural Geology*, *18*(12), 1471–1486. https://doi.org/10.1016/S0191-8141(96)00059-4

Wibberley, C. A. J., Yielding, G., & Di Toro, G. (2008). *Recent advances in the understanding of fault zone internal structure: A review*, *Special Publications* (Vol. 299, pp. 5–33). London: Geological Society.

Williams, J. N., Toy, V. G., Smith, S. A. F., & Boulton, C. (2017). Fracturing, fluid-rock interaction and mineralisation during the seismic cycle along the Alpine Fault. *Journal of Structural Geology*, *103*, 151–166. https://doi.org/10.1016/j.jsg.2017.09.011

Wilson, B., Dewers, T., Reches, Z., & Brune, J. (2005). Particle size and energetics of gouge from earthquake rupture zones. *Nature*, *434*(7034), 749–752. https://doi.org/10.1038/nature03433

Wise, D. U., Dunn, D. E., Engelder, J. T., Geiser, P. A., Hatcher, R. D., Kish, S. A., et al. (1984). Fault-related rocks: Suggestions for terminology. *Geology*, *12*(7), 391–394. https://doi.org/10.1130/0091-7613(1984)12<391:FRSFT>2.0.CO;2

Woodcock, N. H., & Mort, K. (2008). Classification of fault breccias and related fault rocks. *Geological Magazine*, *145*(3), 435–440. https://doi.org/10.1017/S0016756808004883

Worm, H.-U., Clark, D., & Dekkers, M. J. (1993). Magnetic susceptibility of pyrrhotite: Grain size, field and frequency dependence. *Geophysical Journal International*, *114*(1), 127–137. https://doi.org/10.1111/j.1365-246X.1993.tb01472.x

Yamaguchi, A., Cox, S. F., Kimura, G., & Okamoto, S. (2011). Dynamic changes in fluid redox state associated with episodic fault rupture along a megasplay fault in a subduction zone. *Earth and Planetary Science Letters*, *302*(3–4), 369–377. https://doi.org/10.1016/j.epsl.2010.12.029

Yamazaki, K. (2013). Improved models of the piezomagnetic field for the 2011 *Mw* 9.0 Tohoku-oki earthquake. *Earth and Planetary Science Letters*, *363*, 9–15. https://doi.org/10.1016/j.epsl.2012.12.019

Yang, T., Chen, J.-Y., Wang, H.-Q., & Jin, H.-Q. (2012a). Rock magnetic properties of fault rocks from the rupture of the 2008 Wenchuan Earthquake, China and their implications: Preliminary results from the Zhaojiagou outcrop, Beichuan County (Sichuan). *Tectonophysics*, *530-531*, 331–341. https://doi.org/10.1016/j.tecto.2012.01.019

Yang, T., Chen, J.-Y., Wang, H.-Q., & Jin, H.-Q. (2012b). Magnetic properties of fault rocks from the Yingxiu-Beichuan fault: Constraints on temperature rise within the shallow slip zone during the 2008 Wenchuan Earthquake and their implications. *Journal of Asian Earth Sciences*, *50*, 52–60. https://doi.org/10.1016/j.jseaes.2012.01.013

Yang, T., Chen, J.-Y., Xu, H.-R., & Dekkers, M. J. (2019). High-velocity friction experiments indicate magnetic enhancement and softening of fault gouges during seismic slip. *Journal of Geophysical Research: Solid Earth*, *124*, 26–43. https://doi.org/10.1029/2018JB016341

Yang, T., Chen, J.-Y., Yang, X.-S., Wang, H.-Q., & Jin, H.-Q. (2013). Differences in magnetic properties of fragments and matrix of breccias from the rupture of the 2008 Wenchuan earthquake, China: Relationship to faulting. *Tectonophysics*, *601*, 112–124. https://doi.org/10.1016/j.tecto.2013.05.002

Yang, T., Dekkers, M. J., & Chen, J.-Y. (2018). Thermal alteration of pyrite to pyrrhotite during earthquakes: New evidence of seismic slip in the rock record. *Journal of Geophysical Research: Solid Earth*, *123*, 1116–1131. https://doi.org/10.1002/2017JB014973

Yang, T., Dekkers, M. J., & Zhang, B. (2016). Seismic heating signatures in the Japan Trench subduction plate-boundary fault zone: Evidence from a preliminary rock magnetic 'geothermometer'. *Geophysical Journal International*, *205*(1), 319–331. https://doi.org/10.1093/gji/ggw013

Yang, T., Mishima, T., Ujiie, K., Chester, F. M., Mori, J. J., Eguchi, N., Toczko, S., & Expedition 343 Scientists (2013). Strain decoupling across the décollement in the region of large slip during the 2011 Tohoku-Oki earthquake from anisotropy of magnetic susceptibility. *Earth and Planetary Science Letters*, *381*, 31–38. https://doi.org/10.1016/j.epsl.2013.08.045

Yang, T., Yang, X.-S., Duan, Q.-B., Chen, J.-Y., & Dekkers, M. J. (2016). Rock magnetic expression of fluid infiltration in the Yingxiu-Beichuan fault (Longmen Shan thrust belt, China). *Geochemistry, Geophysics, Geosystems*, *17*, 1065–1085. https://doi.org/10.1002/2015GC006095

Yao, L., Ma, S., Niemeijer, A. R., Shimamoto, T., & Platt, J. D. (2016). Is frictional heating needed to cause dramatic weakening of nanoparticle gouge during seismic slip? Insights from friction experiments with variable thermal evolutions. *Geophysical Research Letters*, *43*, 6852–6860. https://doi.org/10.1002/2016GL069053

Yeh, E., Lee, T., Lin, Y., Chou, Y., & Lu, C. (2007). *Analysis of magnetic and grain fabrics across fault gouge in the Chelungpu Fault of Taiwan* (Abstract T43B-1331). Paper presented at American Geophysical Union Fall Meeting 2007, San Francisco, USA.

Zdujić, M., Jovalekić, Č., Karanović, L., Mitrić, M., Poleti, D., & Skala, D. (1998). Mechanochemical treatment of α-Fe_2O_3 powder in air atmosphere. *Materials Science and Engineering A*, *245*(1), 109–117. https://doi.org/10.1016/S0921-5093(97)00715-6

Zhang, L., Li, H.-B., Sun, Z.-M., Chou, Y.-M., Cao, Y., & Wang, H. (2018). Metallic iron formed by melting: A new mechanism for magnetic highs in pseudotachylyte. *Geology*, *46*(9), 779–782. https://doi.org/10.1130/G40153.1

Zhang, L., Sun, Z.-M., Li, H.-B., Zhao, L.-S., Song, S.-R., Chou, Y.-M., et al. (2017). Rock record and magnetic response to large earthquakes within Wenchuan Earthquake Fault Scientific Drilling cores. *Geochemistry, Geophysics, Geosystems*, *18*, 1889–1906. https://doi.org/10.1002/2017GC006822

Zhao, X., Heslop, D., & Roberts, A. P. (2015). A protocol for variable resolution first-order reversal curve measurements. *Geochemistry, Geophysics, Geosystems*, *16*, 1364–1377. https://doi.org/10.1002/2014GC005680

Zhao, X., Roberts, A. P., Heslop, D., Paterson, G. A., Li, Y.-L., & Li, J.-H. (2017). Magnetic domain state diagnosis using hysteresis reversal curves. *Journal of Geophysical Research: Solid Earth*, *122*, 4767–4789. https://doi.org/10.1002/2016JB013683

Zhu, K.-Y., Li, M.-Y., Shentu, L.-F., Shen, Z.-Y., & Yu, Y.-H. (2017). Evaluation of a small-diameter sampling method in magnetic susceptibility, AMS and X-ray CT studies and its applications to mafic microgranular enclaves (MMEs) in granite. *Journal of Volcanology and Geothermal Research*, *341*, 208–227. https://doi.org/10.1016/j.jvolgeores.2017.06.002

Zijderveld, J. D. A. (1967). A.C. demagnetization of rocks: Analysis of results. In D. W. Collinson, K. M. Creer, S. K. Runcorn (Eds.), *Methods in paleomagnetism* (pp. 254–286). New York: Elsevier.

Zoback, M. D., Barton, C. A., Brudy, M., Castillo, D. A., Finkbeiner, T., Grollimund, B. R., et al. (2003). Determination of stress orientation and magnitude in deep wells. *International Journal of Rock Mechanics and Mining Sciences*, *40*(7–8), 1049–1076. https://doi.org/10.1016/j.ijrmms.2003.07.001

Zoback, M. D., Hickman, S., & Ellsworth, W. (2007). The role of fault zone drilling. In H. Kanamori & G. Schubert (Eds.), *Earthquake seismology, treatise on geophysics* (Vol. 4, pp. 649–674). Amsterdam: Elsevier.